DISSERTATION

Ballistic Electron Emission Microscopy/Spectroscopy on Metal-Organic-Semiconductor Heterostuctures

ausgeführt zum Zwecke der Erlangung des

akademischen Grades eines

Doktors der technischen Wissenschaften

unter der Leitung von

Ao. Univ. Prof. Mag. rer. nat. Dr. rer. nat. Jürgen Smoliner

Institut für Festkörperelektronik

eingereicht an der Fakultät für

Elektrotechnik und Informationstechnologie

der Technischen Universität Wien

von

Dipl. Ing.

Soner Özcan

Matrikelnummer: 0025039

Hütteldorferstrasse 130C/4/10

1140 Wien

Wien, März, 2008

Unterschrift

Kurzfassung

Im Zuge dieser Dissertation wurde *Ballistic Electron Emission Microscopy/Spectroscopy* (BEEM/S) verwendet um organische Halbleiter Heterostrukturen zu charakterisieren. Im Detail wurden Heterostrukturen untersucuht, welche die zwei organischen Halbleiter Titanylphthalocyanine (TiOPc, $C_{32}H_{16}N_8OTi$)) und Hexa-*peri* hexabenzocoronene (HBC, $C_{42}H_{18}$) beinhalten.

Au/TiOPc/GaAs Dioden wurden mittels BEEM/S untersucht. Aufgrund der BEEM Bilder lässt sich der Schluss ziehen, dass unsere mit MBE hergestellten Proben im Vergleich zu aufgedampften organischen Filmen sehr homogen sind. Alle Merkmale in den BEEM Bildern unserer Proben korrelieren ausschließlich mit der körnigen Struktur und den topographischen Merkmalen von der Au-Schicht und nicht mit der organischen Schicht darunter. Bei der Analyse der BEEM Spektren wurde festgestellt, dass das TiOPc die Schwellspannung der BEEM Spektren im Vergleich zu Au/GaAs-Dioden erhöht. Die Barrierenhöhe, die in der Au-TiOPc-GaAs Heterostruktur gemessen wurde beträgt $V_b \approx 1.2$ eV. Darüber hinaus sieht man in der ersten Ableitung des BEEM Stromes zusätzliche Schwellen der Energie über dem *lowest unouccupied molecular orbital* (LUMO) levels. In der ersten Ableitung der BEEM Spektren konnten Signaturen des L- and X-Tals von GaAs indentifiziert werden. An herkömmlichen Au-GaAs Dioden sind die Einflüsse der höheren Täler ebenfalls in der ersten Ableitung des BEEM Spektrums als erhöhte Anstiege sichtbar, da die höheren Täler weitere Transportkanäle in die Kollektor Elektrode eröffnen. Die Positionen der höheren Täler in GaAs können nun dazu benutzt werden um die Energieskala zu kalibrieren. Damit kann das Γ-Tal von GaAs indentifiziert werden, welches für die Au/TiOPc/GaAs Heterostruktur 1.1 eV ergibt. Dieser Wert von 1.1 eV liegt aber deutlich unter der gemessenen Schottky Barriere von 1.2 eV und aus diesem Grund sind wir sicher, die Schottky Barriere am Au-TiOPc Übergang gemessen zu haben. Temperaturabhängige Massungen zeigen einen Anstieg der Schottky Barriere von 1.2 eV bei Raumtemperatur

bis hin zu 1.5 eV bei T=10 K.

Die energieabhängigen Elektrontransmissionseigenschaften von TiOPc wurden ebenfalls untersucht. Es wurde herausgefunden, dass die Transmission und auch die mittlere freie Weglänge in Abhängigkeit der Energie steigen, aber ein unterschiedliches Verhalten als Funktion der Temperatur zeigen. Während die mittlere freie Weglänge mit steigender Temperatur sinkt, steigt die Transmission mit steigender Temperatur. Wir glauben, dass die mittlere freie Weglänge durch Phononstreuprozesse dominiert wird, während die Tranmission dominiert wird durch Streuprozesse, die durch Störstellen verursacht werden. In der Annahme, dass ionisierte Unreinheiten Steuprozesse an den Übergängen verursachen und Phononstreuprozesse im Bulk dominieren, können unsere Ergebnisse sehr gut erklärt werden.

Zur Analyse der Daten wurde eine Modellrechnung des BEEM Stromes durch die Au/TiOPc/GaAs Heterostruktur implementiert. Es wurde herausgefunden, dass der ballistische Strom durch die Au/TiOPc/GaAs Heterostruktur für höhere Energien mit der Heterostrukturerweiterung des Bell-Kaiser Models nicht sehr gut beschrieben werden kann. Bei niederen Energien (Bsp. einige meV bis ung. 200 meV über der Schottky Barriere) beschreibt das Model den BEEM Strom durch die Au/TiOPc/GaAs Heterostruktur hingegen sehr gut. Der Grund für die Abweichungen des Models bei höheren Energien sind folgende: Erstens, der Einfluss der höheren GaAs L und X- Täler wurde in den Rechnungen vernachlässigt und zweitens, das Modellieren der TiOPc-Schicht mit einer einfachen rechteckigen Potentialbarriere ist nicht exakt genug. Zusätzlich wurde eine Näherung für die Abschwächlänge von TiOPc als Funktion der Energie vorgestellt.

Die Schottky Barriere der Au/HBC/GaAs Heterostruktur wurde ebenfalls mit BEEM untersucht. Zwischen $T = 300$ K und $T = 10$ K, steigt die Schottky Barriere am Au/HBC Übergang von 1.3 eV bei $T = 300$ K zu 1.56 eV bei $T = 10$ K. Gleichzeitig, wird das *Fermi level pinning* am HBC/GaAs Übergang systematisch tiefer, beginnend bei einer Position von 1.2 eV über dem Leitungsband von GaAs bei $T = 300$ K bis hinzu 1.4 eV bei $T = 10$ K, dieser Wert ist schon sehr nahe am Valenzband von GaAs. Diese hohe Barriere am HBC-GaAs Übergang macht das organische Material HBC zu einer vielversprechenden Grenzflächenschicht um die *open circuit voltage* von GaAs Schottky Solarzellen zu erhöhen.

Im Zuge dieser Dissertation wurden folgende Arbeiten publiziert:

1. S. Özcan, T. Roch, G. Strasser, J. Smoliner, R. Franke and T. Fritz,
   J. Phys: Conf. Ser., 61, 1371, (2007).

2. S. Özcan, J. Smoliner, M. Andrews, G. Strasser, T. Dienel, R. Franke and T. Fritz,
   Appl. Phys. Lett., 90, 092107, selected for the "Virtual Journal of Nanoscale Science and Technology", March 12 (2007).

3. S. Özcan, J. Smoliner, M. Andrews, G. Strasser, T. Dienel and T. Fritz,
   phys. stat. sol. (c), 5, No. 1, $386 - 389$, 2008.

4. S. Özcan, J. Smoliner, M. Andrews, G. Strasser, T. Dienel, R. Franke and T. Fritz,
   Semicond. Sci. Technol., *xxx*, *xxx*, 2008, accepted in print.

5. S. Özcan, J. Smoliner, T. Dienel and T. Fritz,
   Appl. Phys. Lett., *xxx*, *xxx*, 2008, submitted.

Abstract

In the framework of this thesis Ballistic Electron Emission Microscopy/Spectroscopy (BEEM/S) was used to investigate semiconductor heterostructures. Especially heterostructures including organic semiconductors like titanylphthalocyanine (TiOPc, $C_{32}H_{16}N_8OTi$)) and hexa-*peri* hexabenzocoronene (HBC, $C_{42}H_{18}$).

Au/TiOPc/GaAs diodes were investigated by BEEM/S. From the BEEM images it can be concluded that our MBE grown samples are very homogeneous in comparison to organic films manufactured by evaporation. All features visible in the BEEM images of our samples correlate exclusively with the granular structure and the topographic features of the Au-film and cannot be correlated to the organic film underneath. Analyzing the BEEM spectra we find that the TiOPc increases the BEEM threshold voltage compared to reference Au/GaAs diodes. The barrier height measured on the Au-TiOPc-GaAs heterostructure is $V_b \approx 1.2$ eV, whereas the barrier on the Au/GaAs diode is 0.9 eV. In addition, the derivative of the BEEM spectra shows multiple features in the energy regime above the lowest unoccupied molecular orbital (LUMO) level. Using the first derivative of the BEEM spectra signatures of the L- and X-valleys of GaAs can be seen. On conventional Au-GaAs diodes, the influence of higher valleys is normally seen as an increased slope in the first derivative of the spectrum, as the higher valleys open additional transport channels into the collector electrode. The positions of the higher valleys in GaAs can now be used to calibrate the energy scale. Hence we are sure that the measured Schottky barrier height really is the barrier height at the Au/TiOPc interface. Temperature studies show an increase of the SBH from 1.2 eV at room temperature to 1.5 eV at 10 K.

The energy dependent electron transmission properties of TiOPc were investigated too. It was found, that the transmission and the mean free path both increase with energy, but exhibit a different behavior as a function of temperature. While the decreasing mean free path with increasing temperature suggests, that the mean free path is dominated by phonon

scattering processes, the TiOPc transmission increases with increasing temperature, which suggests that the transmission is dominated by impurity scattering processes. Assuming dominant ionized impurity scattering at the interfaces, and dominant phonon scattering in the bulk, however, our findings can be consistently explained.

To analyze the data, a model calculation for the BEEM current through the Au/TiOPc/GaAs heterostructure was implemented. It was found that at higher energies, the ballistic current through Au/TiOPc/GaAs heterostructure can not be described precisely with the heterostructure extension of the Bell-Kaiser model for mainly two reasons: First, the influence of the GaAs L and X valleys was not included into the calculations, and second, modelling the TiOPc with a simple rectangular potential barrier is not accurately enough. Additionally, an approach for the determination of the attenuation length of TiOPc as a function of energy has been successfully introduced.

Finally, the Schottky barrier heights of Au/HBC/GaAs heterostructures were investigated by BEEM. Between $T = 300$ K and $T = 10$ K, the Schottky barrier height at the Au/HBC interface increases from 1.3 eV at $T = 300$ K to 1.56 eV at $T = 10$ K. Simultaneously, the Fermi level pinning at the HBC/GaAs interface becomes systematically deeper, starting with a position of 1.2 eV above the GaAs conduction band at $T = 300$ K and ending at 1.4 eV at $T = 10$ K, which is close to the valence band of GaAs. The high barrier at the HBC-GaAs interface makes this material a promising interfacial layer for increasing the open circuit voltage of GaAs Schottky barrier solar cells.

Whitin this thesis the following publications have been made:

1. S. Özcan, T. Roch, G. Strasser, J. Smoliner, R. Franke and T. Fritz,
   J. Phys: Conf. Ser., 61, 1371, (2007).

2. S. Özcan, J. Smoliner, M. Andrews, G. Strasser, T. Dienel, R. Franke and T. Fritz,
   Appl. Phys. Lett., 90, 092107, selected for the "Virtual Journal of Nanoscale Science and Technology", March 12 (2007).

3. S. Özcan, J. Smoliner, M. Andrews, G. Strasser, T. Dienel and T. Fritz,
   phys. stat. sol. (c), 5, No. 1, $386 - 389$, 2008.

4. S. Özcan, J. Smoliner, M. Andrews, G. Strasser, T. Dienel, R. Franke and T. Fritz,
   Semicond. Sci. Technol., *xxx*, *xxx*, 2008, accepted in print.

5. S. Özcan, J. Smoliner, T. Dienel and T. Fritz,
   Appl. Phys. Lett., *xxx*, *xxx*, 2008, submitted.

Acknowledgements

Contents

Chapter 1

Introduction

The current trend of developing small size electronic devices requires high resolution in the characterization and control of metal-semiconductor heterostructures. To improve device characterization and performance, and for a better understanding of the basic physics of metal-semiconductor interfaces, there is an increase demand for nanometer scale probes, all the way down to the atomic level, of the spatial and electronic properties of metal-semiconductor junctions and semiconductor heterostructures.

The invention of the Scanning Tunneling Microscope (STM) [1, 2] by G. Binning, H. Rohrer and coworkers in 1981 was the trigger for the new field of Scanning Probe Microscopy and Spectroscopy (SPM/SPS) which has since then experienced a rapid flourishing. The development and application of local probe techniques, such as STM, Atomic Force Microscopy (AFM), Scanning Near field Optical Microscopy (SNOM), Transmission Electron Microscopy (TEM), and many more, gave rise to the possibility of a thorough investigation of micro- and nanometer sized structures.

Ballistic Electron Emission Microscopy/Spectroscopy (BEEM(S) is a powerfull tool for nondestructive local characterization of semiconductor heterostructures, and was invented by Bell and Kaiser [3, 4] in 1988. In BEEM, the metallic STM tip (emitter) injects electrons across the tunneling gap into the metal (base) layer deposited on a semiconductor. A third terminal on the sample backside is used to collect those electrons, which traverse the interface.

1.1   State of the Art

Orginally the BEEM technique was invented as a unique microscopic and spectroscopic method to probe the Schottky Barriers on a local scale [4], including technologically important semiconductors such as Ga(Al)As [5, 6, 7], Ga(In)P [8, 9, 10], Ga(As)N [11, 12, 13, 14], and Si [15, 16], SiC [17].

BEEM has also been successfully used to study the electronic properties of buried heterojunctions. Further, BEEM was successfully applied to metal-insulater-semiconductor structures to study the transport related oxide properties on a microscopic scale in buried CaF_2/Si [18] and SiO_2 [19]. In SiO_2- based metal-oxide-semiconductor structures, BEEM was used to study the quantum interference effects and trapped charge distribution that is very important of metal-oxide-semiconductor field-effect transistors [20, 21]. Significant progress was accomplished in establishing BEEM as an effective method for measuring semiconductor heterojunction offsets [7, 22, 23], for measuring resonant transport through single-barrier [24], double-barrier [25] and superlattice resonant tunneling heterostructures [26, 27], for investigation of hot carrier transport in low-dimensional nanostructures such as quantum wires [28, 29] and quantum dots [30, 31, 32], as well as for imaging of defects buried below the surface [33, 34, 35].

Another interesting application of BEEM is to investigate metal-organic-semiconductor heterostructures, which is presented in this work. There have been investigations about metal-organic-semiconductor heterostructures, e. g. : BEEM of a buried Ag/polyparaphenylene interface [36, 37], BEEM on Ag/polyparaphenylene/semiconductor and Ag/poly(2-methoxy-5-2-ethyl-hexyloxy-1,4-phenylenevinylene)/semiconductor heterostructures [38], BEEM studies on Au/octanedithiol/GaAs diodes [39], BEEM studies on Au/alkanedithiol/GaAs diodes [40], BEEM investigations of a Au/GaAs diode with a discontinuous monolayer of dicarboxylic acids at the interface [41], and BEEM studies of organic molecules (fullerene C_{60} and 3,4,9,10-perylene-tetracarboxylic acid dianhydride) on uniformly flat surfaces of bismuth grown on silicon [42], and of course the works presented here on Au/TiOPc/GaAs [43, 44, 45, 46, 47] and Au/HBC/GaAs heterostructures [48].

1.2 Overview About the Work Presented in this Thesis

In this work a systematic study of metal-organic-semiconductor heterostructures is presented. The organic semiconductors investigated in this work are: titanylphthalocyanine (TiOPc, $C_{32}H_{16}N_8OTi$)) and hexa-*peri* hexabenzocoronene (HBC, $C_{42}H_{18}$).

After a introduction to BEEM in chapter 2, a short description to the transfer matrix method is given in section 2.5, and in chapter 3 a introduction to organic semiconductors and energy level alignment at metal-organic interfaces is given.

In chapter 4 first experimental results on Au/TiOPc/GaAs diodes incorporating ultra smooth thin films of the archetypal organic semiconductor TiOPc are presented. From our BEEM images we conclude that our molecular beam epitaxial (MBE) grown samples show very homogeneous transmission, compared to organic films manufactured by simple evaporation. The barrier height measured on the Au-TiOPc-GaAs is $V_b \approx 1.2$ eV, which is in good agreement with the data found in reference [49].

In chapter 5 the Schottky barrier heights of the Au/TiOPc/GaAs heterostructure are investigated for various temperatures and show an approximately linear increase from 1.2 eV at room temperature to 1.5 eV at $T = 10$K.

In chapter 6 BEEM/S measurements are used to determine the transmission of ballistic electrons through TiOPc as a function of energy and temperature. A modelling of the BEEM current through the Au/TiOPc/GaAs heterostructure is implemented. It is found that the ballistic current through Au/TiOPc/GaAs heterostructure can not be described precisely with the heterostructure extension of the Bell-Kaiser model at higher energies. This is because of two reasons: First, we did not include the influence of the GaAs L and X valleys into the calculations, and modelling the TiOPc with a simple rectangular potential barrier is not accurately enough.

In chapter 7 we investigate the electron transmission properties of TiOPc. Additionally, an approach for the determination of the energy dependent attenuation length of TiOPc is successfully introduced. Further, we present an experimental investigation of hot electron transport in thin TiOPc films grown on GaAs and an alternative approach to calculate the attenuation length in titanylphthalocyanine.

In chapter 8 Au/HBC/GaAs heterostructures are investigated by ballistic electron emission microscopy. At room temperature, the Schottky barrier height at the Au/HBC inter-

face was measured to be 1.3 eV, while the Fermi level at the HBC-GaAs interface is pinned 1.2 eV below the GaAs conduction band. Decreasing the temperature down to $T = 10$ K, the Au/HBC Schottky barrier height increases up to 1.55 eV and the Fermi level pinning at the HBC-GaAs interface reaches a value of 1.4 eV, close to the valence band of GaAs. These high values make HBC a promising interfacial layer in order to increase the open circuit voltage of GaAs Schottky barrier solar cells

Finally, in chapter 9 a summary of the presented work is given together with an outlook.

Chapter 2

Ballistic Electron Emission Microscopy (BEEM)/ Spectroscopy (BEES)

2.1   Introduction

Understanding the atomic structure of materials, the behavior and reaction of atoms at surfaces, and the nature of electronic properties at the atomic scale have been the goals of fundamental and applied research for many decades. There where only few experimental probes to verify imagination and intuition for physics on the atomic scale, but still on an indirect or incomplete glimpse of the atomic structure at surfaces. The development of Scanning Tunnel Microscopy (STM) [1] has revolutionized the approach to the investigation of many aspects of material properties at the atomic scale. The STM and the technique have provided methods to measure accurately the three dimensional structure and electronic properties of single surface atoms. Extensions of the STM technique, such as atomic force microscopy, have allowed various other properties to be measured on an nanometer scale. As STM methods have been refined, several experiments have demonstrated the ability to manipulate individual atoms accurately. These recent STM demonstrations are not only accomplishments of modern science, but also fulfill the aspirations of those who first imagined the existence of atoms. This technique has proven to be a powerfull and versatile tool for the determination of structural and electronic properties of samples [2], [50], [51]. With the introduction of ballistic electron emission microscopy / spectroscopy

(BEEM/BEES) by Kaiser [4] and Bell [3] the unique spatial resolution of the STM has been combined with the possibility of locally probing the electronic structure of sub-surface interfaces. This chapter will give an introduction to BEEM.

2.2   Basic Principles of BEEM

The term Ballistic Emission Microscopy/Spectroscopy (BEEM/BEES) denominates a technique utilizing a scanning tunnelling microscope (STM) as an emitter for ballistic electrons. The spectroscopic and imaging capabilities of STM have made it a powerful method for measuring and viewing surfaces at the atomic level. An introduction to STM can be found for example in [52, 53, 54]. A typical BEEM/S sample consists of at least two layers forming an interface, which functions as a potential barrier for the electrons. To optimize the measurement of the ballistic current the conducting top (base) electrode has to be in contact with an n-type semiconductor. Fig. 2.1 shows a typical sample of BEEM/S. Here the natural band bending accelerates the ballistic electrons in the semiconductor away from the metal-semiconductor interface thus preventing them from leaking back into the base. The BEEM spectrum is recorded by keeping the STM tip at a fixed position while the tunnel voltage is varied within a predefined interval and the ballistic current depending on the tunnel voltage, $I_c(V_t)$ is measured at this position by maintaining constant current mode.

Figure 2.2 displays the conduction band profile of a simple Schottky diode sample together with the ballistic current.

The potential for electrons in the STM tip exceeds the potential in the base due to the applied tunnel voltage, with the tip under negative voltage compared to the base. Therefore, electrons reaching the base via tunnelling through the vacuum barrier show energies high above the Fermi level in the base metal, i.e. they are defined as so-called ballistic or hot electrons. As long as the energy provided by the tunnel voltage, eV_t, does not exceed the Schottky barrier height, no electrons will be transmitted into the semiconductor, thus the ballistic current is zero. On the other hand, having an energy higher than the Schottky barrier at the metal-semiconductor interface, the injected electrons will enter into the semiconductor thus causing a measurable ballistic current I_c at the collector electrode. The higher the tunnel voltage is, the more electrons will increase the magnitude of I_c.

Recording the corresponding ballistic current while keeping STM tip constant in xy
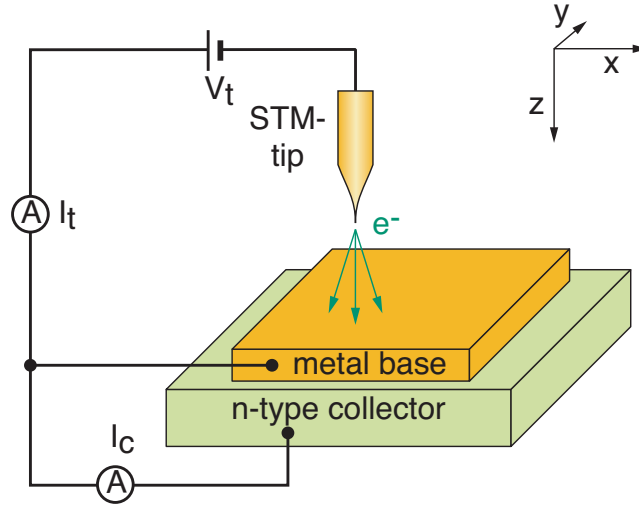
Figure 2.1: Sketch of a BEEM setup with a Schottky diode as a sample (not to scale). The tunnel voltage V_t is applied between the STM tip and the metal surface of the sample, the tunnel current I_t in this circuit is kept constant by the STM feedback loop. A second amperemeter measures the ballistic current I_c between the metal base and the semiconductor collector.
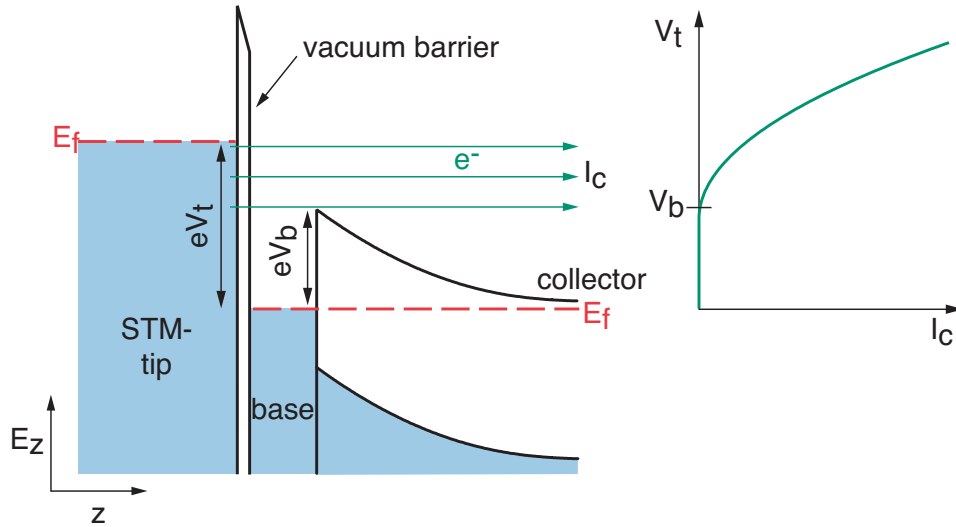
Figure 2.2: Left part: Schematic energy diagram of a BEEM experiment on a Schottky diode. Electrons tunnel from the STM tip into the base. If $eV_t > eV_b$, electrons will be able to surmount the Schottky barrier and enter the semiconductor. — Right part: Ballistic current spectrum $I_c(V_t)$ corresponding to the energy diagram on the left (for varying V_t). Defining zero by the Fermi level of the base, the current sets in at $V_t = V_b$.
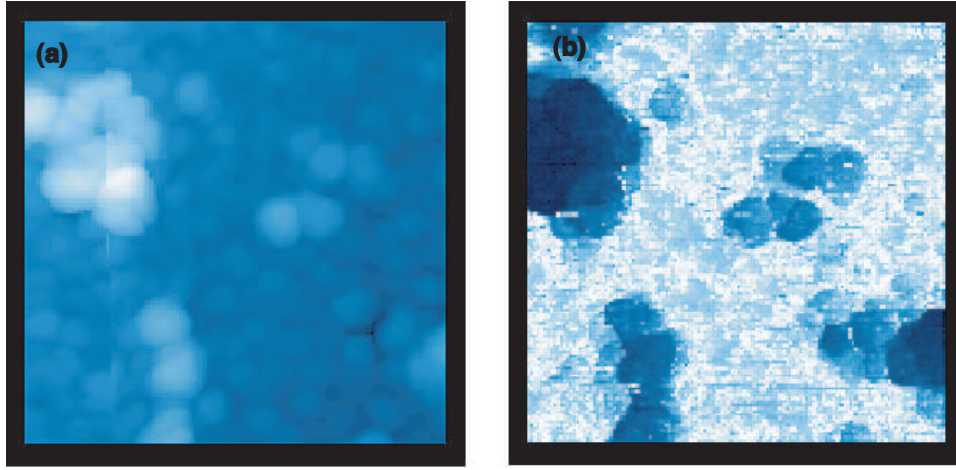
Figure 2.3: (a) STM topographic image of a 70 Å thick gold film evaporated onto a GaAs substrate. Scan size: 100 nm × 100 nm, z-scale: 4 nm, $V_t = 1.8$ V, $I_t = 5$ nA. Bright regions indicate elevations. (b) BEEM image corresponding to (a). z-scale: 100 pA. Bright regions indicate areas of higher transmission.

with respect to the sample surface and varying the tunnel voltage within a chosen interval represents the spectroscopic part of BEEM, often also explicitly referred to as BEES. The plot of $I_c(V_t)$ is usually denoted *BEEM spectrum*.

As mentioned above BEEM image is done by moving the STM tip in constant current mode across the sample surface while keeping the tunnel voltage constant. If the tunnel voltage is chosen correctly, e.g. areas of different barrier height can be directly depicted with this procedure. Because the size of the ballistic current is also influenced by topographic effects, BEEM images are usually taken simultaneously together with the corresponding STM image, to distinguish between topographic effects and changes in the sub-surface properties of the sample. This is a straightforward procedure since the tunnel current and ballistic current are measured independently anyway. Figure 2.3 gives an example of an STM topography and the corresponding BEEM image, taken on an Au/GaAs Schottky diode. The structures are the gold grains of the polycrystalline base layer. The transmission for ballistic electrons is smaller for regions with a thicker gold coverage, therefore producing dark regions in the BEEM image in those areas which show elevations in the STM topography.

2.3 Electron Refraction Effects in BEEM

When the electrons are crossing an interface, their momentum component parallel to this interface does not change. This is often called as *parallel momentum conservation*. This fact that the xy-momentum is conserved during the passage through the interface has profound implications in BEEM.

Typical BEEM samples possess a huge potential step between the base and the collector (caused by the Schottky barrier) as well as strongly different effective masses in the involved areas. As a consequence, electron "refraction" effects are observed, which are described in detail as follows: Note, that for refraction effects, the influence of the potential step is usually even more significant than the mass difference [55].
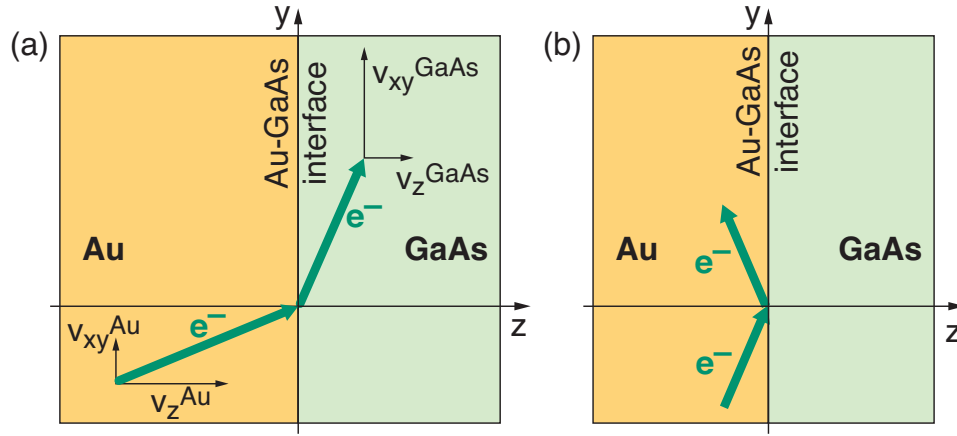
Figure 2.4: (a) Electron refraction: By crossing the interface from Au to GaAs, the electron will gain velocity parallel to the interface and lose velocity perpendicular to it. — (b) Total reflection: If the incident angle with respect to the z-axis is larger than the critical angle, the electron cannot enter the GaAs and is reflected.

As a typical example for electron refraction effects, Figure 2.4 illustrates the situation at the Au-GaAs interface. The effective electron mass in the gold is equal to the free electron mass, m_0, while the effective electron mass in the semiconductor, m^*, is respectable smaller (for GaAs: $m^* = 0.067\ m_0$). To quantify the consequences of this situation, we first write down the energy of the motion parallel to the interface :

$$E_{xy} := E(\mathbf{k}_{xy}) = \frac{\hbar^2 \mathbf{k}_{xy}^2}{2m(z)} = \frac{\hbar^2}{2m(z)}\left(k_x^2 + k_y^2\right) \tag{2.1}$$

By using the relation given in equation 2.1 for the energy associated with the motion in the xy-plane and the momentum conservation law for k_{xy}, the energy component parallel to the interface changes according to:

$$E_{xy}^{GaAs} = E_{xy}^{Au} \frac{m_0}{m^*} \qquad (2.2)$$

The conservation of the total energy E is another limitation, which can be written as:

$$E = \frac{\hbar^2 \mathbf{k}^2}{2m(z)} + E_{pot} = \frac{\hbar^2}{2m(z)} \left(k_x^2 + k_y^2 + k_z^2 \right) + E_{pot} = E_{xy} + E_z + E_{pot} \qquad (2.3)$$

Therefore, the energy associated with the movement vertical to the interface is given by:

$$E_z^{GaAs} = E - E_{xy}^{GaAs} - E_b = E_0 + E_z^{Au} + E_{xy}^{Au} - E_{xy}^{Au} \frac{m_0}{m^*} - E_b$$

$$E_z^{GaAs} = E_z^{Au} - E_{xy}^{Au} \left(\frac{m_0}{m^*} - 1 \right) - eV_{b0} \qquad (2.4)$$

where $eV_{b0} := E_b - E_0$ is the height of the potential step at the interface, with E_0 the conduction band minimum in the metal, and E_b the conduction band minimum in the semiconductor. The first subtrahend in this expression represents the decrease in E_z due to the change of effective mass, while the second one just originates from the potential step.

For the particular case of an Au-GaAs interface, where the effective mass in the GaAs is just 6.7% of the electron mass in the Au layer, E_{xy}^{GaAs} is almost 15 times higher than the energy parallel to the interface in the gold. Electrons crossing the Au-GaAs interface will gain E_{xy} according to equation 2.2 and lose E_z according to equation 2.4. Therefore, they will be refracted away from the z-axis, as depicted in Figure 2.4(a). Only those electrons which have exactly a perpendicular angle of incidence at the interface, i.e. $k_{xy} = 0$, will not undergo any refraction.

A instantaneous consequence of this refraction away from the z-axis is the possibility of total reflection at the Au-GaAs interface. By considering the arrangement of a BEEM experiment, it is obvious, that only electrons with $k_z^{GaAs} \geq 0$ can travel through the semiconductor and finally be collected at the backside of the heterostructure, i.e. contribute to the ballistic current. From this it follows automatically an upper limit for k_{xy} and

therefore a maximum angle of incidence (with respect to the z-axis) for an electron in the base.

Now we want to calculate this critical angle for total reflection, therefore we use equation 2.3 to isolate E_z and take this in turn to find an expression for the momentum component vertical to the interface, k_z:

$$k_z^{Au} = \sqrt{\frac{2m_0}{\hbar^2}(E - E_0) - k_{xy}^2} \tag{2.5}$$

$$k_z^{GaAs} = \sqrt{\frac{2m^*}{\hbar^2}(E - E_b) - k_{xy}^2} \tag{2.6}$$

From $k_z^{GaAs} \geq 0$ and equation 2.6 it follows directly, that:

$$k_{xy}^2 \leq \frac{2m^*}{\hbar^2}(E - E_b) \tag{2.7}$$

The angle of incidence with respect to the z-axis can be described by:

$$\sin(\theta_{Au}) = \frac{k_{xy}}{k} \quad \text{with} \quad k = |\mathbf{k}| = \sqrt{\frac{2m_0(E - E_0)}{\hbar^2}} \tag{2.8}$$

By combining relation (2.7) and equation (2.8) , the critical angle can be determined by:

$$\sin^2(\theta_{crit}) = \frac{m^*}{m_0} \frac{E - E_b}{E - E_0} = \frac{m^*}{m_0} \frac{E' - eV_{b0}}{E'} \tag{2.9}$$

with $E' = E - E_0$, the total electron energy referring to the conduction band minimum in the gold base and eV_{b0}, as defined above, the height of the potential step. In a typical experimental situation, where the material in front of the interface is represented by the base layer of the BEEM sample, it is more convenient, to refer all energies to the Fermi level in the base layer rather than to the conduction band minimum. This can be achieved by the simple substitution of $eV = E' - E_f$ and $eV_b = eV_{b0} - E_f$ leading to a critical angle of:

$$\sin^2(\theta_{crit}) = \frac{m^*}{m_0} \frac{eV - eV_b}{eV + E_f} \tag{2.10}$$

where eV_b now is the usual Schottky barrier height and E_f is the position of the Fermi level with respect to the conduction band minimum in the base layer. $eV + E_f$ is the total

energy of the incident electron, e.g. provided by a tunnel voltage. Electrons are only able to cross the interface, if their angle of incidence, θ, fulfils the requirement:

$$\sin(\theta) \leq \sin(\theta_{crit}) \tag{2.11}$$

Electrons with a larger angle of incidence will be reflected at the interface, as depicted in Figure 2.4(b). In a BEEM experiment, the above condition defines the opening angle of the so-called *acceptance cone* for electrons in the metal film, which selects a fraction of those electrons, which have overcome the tunnel barrier, for further transmission into the semiconductor.

Taking typical values for a BEEM experiment on an Au-GaAs interface, one can see nicely the influence of the effective mass change: Assuming a Schottky barrier height of 1 eV and an injection energy of 1.1 eV, the critical angle without considering the effective mass would be about 18°. But if we consider the change in effective mass too, the critical angle will be just 4.5°.

There is significant effect on the *lateral resolution* of BEEM caused by the small critical angles. Only electrons within the acceptance cone will determine the lateral resolution, because only those will be able to enter the semiconductor and therefore to contribute to the ballistic current. Assuming a point-like electron source at the top of the base layer, the minimal lateral resolution is determined by:

$$\Delta x = 2d \tan(\theta_{crit}) \tag{2.12}$$

where d is the thickness of the base layer. Taking the critical angle calculated above, the lateral resolution will be 16 Å for a 100 Å thick base layer and 11 Å for a 70 Å thick one.

Note, that the determination of the lateral resolution by the acceptance cone further has the consequence, that scattering in the base layer will usually *not* deteriorate the lateral resolution. Scattering in the base will just lead to a general decrease of the ballistic current, because it will remove electrons from the acceptance cone by changing their angle of incidence.

Finally, because it will be needed later, also the restriction on the initial energy component parallel to the interface shall be written down here explicitly. From equation (2.7) and $E_{xy}^{Au} = \frac{\hbar^2 k_{xy}^2}{2m_0}$ immediately follows, that:

$$E_{xy}^{Au} \leq \frac{m^*}{m_0} \left(E - E_b \right) . \tag{2.13}$$

Expressing this in terms of E_z^{Au} rather than in terms of the total energy, by using $E = E_{xy}^{Au} + E_z^{Au} + E_0$, and further replacing again E_b directly by the barrier height, with $E_b = eV_{b0} + E_0$, one receives:

$$E_{xy}^{Au} \leq \frac{m^*}{m_0} \left(E_{xy}^{Au} + E_z^{Au} + E_0 - eV_{b0} - E_0 \right) \tag{2.14}$$

$$E_{xy}^{Au} \leq \frac{m^*}{m_0 - m^*} \left(E_z^{Au} - eV_{b0} \right) \tag{2.15}$$

Or, referring again to the more common Schottky barrier height with respect to the Fermi level in the Au base, by substituting $eV_{b0} = eV_b + E_f$:

$$E_{xy}^{Au} \leq \frac{m^*}{m_0 - m^*} \left(E_z^{Au} - E_f - eV_b \right) . \tag{2.16}$$

2.4   The Bell-Kaiser Model

In 1988, Bell and Kaiser introduced BEEM, they presented a formula for the ballistic current, which is known as the Bell-Kaiser model and is widely utilised in BEEM/BEES [3]. Their first step in developing their model was to use the well-known formalism for tunnelling between planar electrodes as an approximation. For simplicity, the STM tip and the base layer are assumed to be identical metals. Further, heterostructures incorporated into the collector, are not treated by the original Bell-Kaiser Model.

At T=0, electrons tunnelling from the STM tip to the metal base occupy tip states within a half-shell (because of the restriction $k_z > 0$) of the Fermi sphere between $E = E_f$ and $E = E_f - eV_t$. Within this model, the tunnel current can be written as [3, 56]:

$$I_t(V_t) = \frac{2eA}{(2\pi)^3} \int d^3k \ T_{tb}(E_z) \frac{\hbar k_z}{m_0} \left[f(E) - f(E + eV_t) \right] \tag{2.17}$$

For convenience, here as well as in the following, all energies are referring to the STM tip conduction band minimum. The BEEM sample is assumed to be energetically lowered with respect to the tip by a positive tunnel voltage V_t applied to the base layer of the sample. A is the effective tunnel area, f the Fermi function and $T_{tb}(E_z)$ the tunnelling probability. Note, that the expression $\frac{\hbar k_z}{m_0}$ is the velocity component parallel to the z-axis.

Provided that the barrier between tip and base at $V_t = 0$ is a square barrier of height Φ and width s, and will be distorted into a trapezoidal shape by applying a tunnel voltage, the tunnelling probability given by the WKB model can be approximated by [57]:

$$T_{tb}(E_z) = e^{-\alpha s \sqrt{E_f + \Phi - \frac{eV_t}{2} - E_z}} \tag{2.18}$$

with $\alpha = \sqrt{8m_0}/\hbar = 1.024$ eV$^{-\frac{1}{2}}$Å^{-1}.

Substituting the integral over the wave vector by integrals over the energy components associated with k_{xy} and k_z yields:

$$I_t(V_t) = C \int\limits_0^\infty dE_z \, T_{tb}(E_z) \int\limits_0^\infty dE_{xy} \left[f(E) - f(E + eV_t) \right] \tag{2.19}$$

with the constant $C = 4\pi A m_0 e / h^3$.

A analogical expression can be forthwith obtained for the collector current. However, due to the conservation of the total energy and the xy-momentum at the metal-semiconductor interface, additional restrictions apply to those tip states which can contribute to the collector current. The first one originates from the requirement, that the electrons must have enough energy to overcome the Schottky barrier between the base layer and the semiconductor ballistically. Because here, E_z refers to the tip conduction band minimum and the conduction band minimum in the base layer lies at $-eV_t$ with respect to the one in the tip, the minimum E_z which facilitates a ballistic entry of the semiconductor is:

$$E_z^{min} = E_f - eV_t + eV_b \tag{2.20}$$

The second limit has its origin in the refraction at the metal-semiconductor interface and is given by equation 2.16. Again, one has to bear in mind, that the energies now refer to the tip, and therefore:

$$E_{xy}^{max} = \frac{m^*}{m_0 - m^*} \left(E_z - E_f + eV_t - eV_b \right) \tag{2.21}$$

Using these two restrictions as integration limits, one can express the collector current as:

$$I_c(V_t) = RC \int\limits_{E_z^{min}}^{\infty} dE_z \, T_{tb}(E_z) \int\limits_0^{E_{xy}^{max}} dE_{xy} \left[f(E) - f(E + eV_t) \right] \tag{2.22}$$

R is a measure of the attenuation due to scattering in the base layer. The attenuation length for ballistic electrons in metals is in very good approximation energy independent within the energy ranges used in BEEM experiments for the measurement of Schottky barrier heights, and therefore R shall be treated here as a constant.

To get an expression of the ballistic current and to eliminate the prefactor C, Bell and Kaiser [3], suggested to normalise $I_c(s_0, V_t)$ by $I_t(s_0, V_t)$ for each voltage V_t. The expression for I_c then takes the following form, commonly known as the *Bell-Kaiser-Formula*:

$$I_c(V_t) = R \, I_{t0} \, \frac{\int\limits_{E_z^{min}}^{\infty} dE_z \, T_{tb}(E_z) \int\limits_0^{E_{xy}^{max}} dE_{xy} \left[f(E) - f(E + eV_t) \right]}{\int\limits_0^{\infty} dE_z \, T_{tb}(E_z) \int\limits_0^{\infty} dE_{xy} \left[f(E) - f(E + eV_t) \right]} \tag{2.23}$$

where I_{t0} is the constant tunnel current at which the ballistic spectrum is measured. The Bell-Kaiser formula is well suited for fitting ballistic electron spectra on simple Schottky diodes in a tunnel voltage range of up to $\approx$ 200 mV [58, 59, 60, 61, 62, 63, 64, 65, 66, 67, 27, 68, 69, 70, 71, 26, 72, 73, 74, 75, 76, 77, 78, 79, 80, 81, 82, 83, 84, 29, 85] above the onset, i.e. eV_b. Many authors use the Bell-Kaiser model even up to tunnel voltages of $\approx$ 600 mV [86, 87, 88, 89] above the onset. However, for such large ranges usually a noticeable deviation has to be taken into account. At higher tunnel voltages numerous scattering processes occur and energy dependent influences become important.

2.4.1 Heterostructure Extension for the Bell-Kaiser Model

Recently BEEM techniques have been extended to the study of buried semiconductor heterostructures [90, 25]. An extension of the initial theoretical description of the ballistic current was introduced by Smith and Kogan [63]. Their model was developed to describe the BEEM spectra of buried heterostructures such as the double barrier resonant tunneling diode used by Sajoto [25]. Essentially, their model is a modification of the original Bell-Kaiser model, where the properties of the buried heterostructure are described by an additional transmission coefficient T_{hs} introduced into the numerator of the Bell-Kaiser formula.

$$I_c(V_t) = R \, I_{t0} \, \frac{\int\limits_{E_z^{min}}^{\infty} dE_z \, T_{tb}(E_z) \, T_{hs}(E_z) \int\limits_{0}^{E_{xy}^{max}} dE_{xy} \, [f(E) - f(E + eV_t)]}{\int\limits_{0}^{\infty} dE_z \, T_{tb}(E_z) \int\limits_{0}^{\infty} dE_{xy} \, [f(E) - f(E + eV_t)]} \qquad (2.24)$$

Besides T_{hs}, all variables are defined just as in equation 2.23. The integration limits are again given by equations 2.20 and 2.21. Note, that T_{hs} does not only describe the transmission behaviour of the buried heterostructure, but must also include the quantum mechanical reflections in the region between the metal-semiconductor interface and the buried heterostructure. The total coefficient T_{hs} is usually calculated by a transfer matrix method, as described in the following section.

It must be pointed out, that the formula above only accounts for the coupling of the transverse and the longitudinal energy via the upper border of integration limit E_{xy}^{max}. While this is not a problem for simple Schottky barriers, the proper choice of E_{xy}^{max} for samples with buried tunnelling structures is not straightforward.

In our opinion, a much more instructive way to include this coupling, is to calculate the transmission through the BEEM sample, starting at the metal-semiconductor interface, in dependence of both, E_{xy} and E_z:

$$I_c(V_t) = R \, I_{t0} \, \frac{\int\limits_{E_z^{min}}^{\infty} dE_z \, T_{tb}(E_z) \int\limits_{0}^{\infty} dE_{xy} \, T_{hs}(E_z, E_{xy}) \, [f(E) - f(E + eV_t)]}{\int\limits_{0}^{\infty} dE_z \, T_{tb}(E_z) \int\limits_{0}^{\infty} dE_{xy} \, [f(E) - f(E + eV_t)]} \qquad (2.25)$$

In this expression E_{xy}^{max} does no longer have to be declared explicitly, because this limit is now implicitly included via the dependence of T_{hs} on E_{xy}. Note, that the transmission coefficient of the vacuum barrier and the transmission of the heterostructure should not be combined into an overall transmission coefficient since this leads to quantum interferences between the vacuum barrier and the collector barrier when calculating I_C explicitly. In principle, such interferences could exist, but in practice they are not observed in BEEM, because of the scattering processes at the non epitaxial Au-GaAs interface and the electron-electron scattering in the Au-base layer. Details on the calculation of T_{hs} are described in the following section.
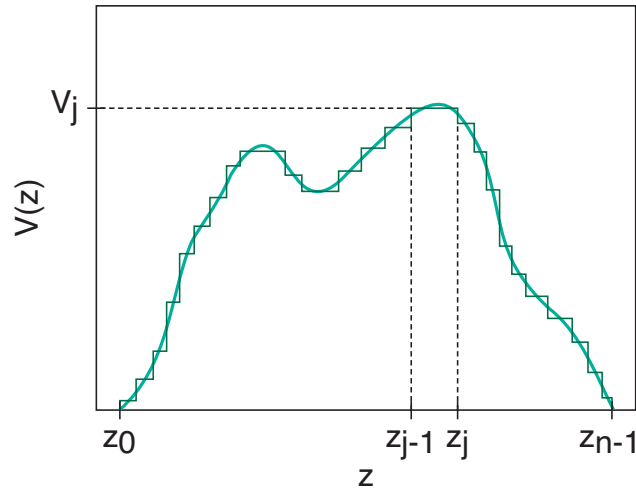
Figure 2.5: Approximation of an arbitrary potential profile by a piecewise constant potential. The j-th section is located between z_{j-1} and z_j. Note, that the width of the single steps does not need to be equal for all subdivisions, but can be adjusted according to requirements.

2.5 The Transfer Matrix Method

The transfer matrix method [91, 92] is used to calculate the quantum mechanical transmission factor of the considered heterostructures, which is essential for the description of BEEM spectra. Because it is based on the approximation of an arbitrary potential by a piecewise constant potential, it is especially well suited to calculate the transmission through such heterostructures which exhibit a band profile consisting on rectangles, e.g. double-barrier resonant tunneling diode and superlattices. The principles of this method as well as the modifications concerning the electron refraction effects mentioned earlier are outlined in the following.

The following description is based on a one-dimensional, arbitrary potential profile $V(z)$. The given potential shape can be subdivided into several sections. For each section the potential and the effective mass is assumed to be constant (see Figure 2.5). Each potential change between two such sections represents an ideal step function. These assumptions allow for the Schrödinger equation to be written and solved for each of these sections without difficulties. In the next step, those partial solutions are connected together by using the continuity of the wave function and its derivative to match the wave functions at each sampling point.

First, a band profile which is subdivided into n sections can be written as:

$$V(z) = \sum_{j=0}^{n-1} V_j \qquad \text{with}: \quad V_j = \begin{cases} const \text{ for } z_{j-1} < z < z_j \\ 0 \text{ elsewhere} \end{cases} \tag{2.26}$$

The analogous description applies to the z-dependent effective mass, where m_j is the (effective) mass in the j-th region.

Using a stationary approach, the one-dimensional Schrödinger equation within the region j (i.e. for a constant potential and a constant effective mass) is:

$$\left[-\frac{\hbar^2}{2m_j} \frac{d^2}{dz^2} + V_j - E_z \right] \psi(z) = 0 \tag{2.27}$$

It must be pointed out, that we first consider electrons with zero parallel momentum and therefore with zero components of kinetic energy due to a motion parallel to the barriers. As in this case the energy depends on k_z only, it is therefore denoted as E_z. Electrons with non-zero k_{xy} and electron refraction effects will be considered later in this section.

The general solution ψ_j in the region $z \in [z_{j-1}, z_j]$ is written as :

$$\psi_j(z) = A_j e^{ik_j z} + B_j e^{-ik_j z} \tag{2.28}$$

with:

$$k_j = \sqrt{\frac{2m_j(E_z - V_j)}{\hbar^2}} \tag{2.29}$$

The boundary conditions at the sampling point $z = z_j$ between the two adjoining sections j and $j+1$ are:

$$\psi_j(z_j) = \psi_{j+1}(z_j) \tag{2.30}$$

$$\frac{1}{m_j} \frac{\partial \psi_j(z)}{\partial z} \bigg|_{z=z_j} = \frac{1}{m_{j+1}} \frac{\partial \psi_{j+1}(z)}{\partial z} \bigg|_{z=z_j} \tag{2.31}$$

For convenience, the following abbreviations are introduced:

$$u_j(z) = A_j e^{ik_j z} \qquad \text{and} \qquad v_j(z) = B_j e^{-ik_j z}$$

Now, the relations between u_j and v_j on the one hand and u_{j+1} and v_{j+1} on the other hand can be calculated from the boundary conditions (equation (2.30), (2.31)), which read as:

$$u_j(z_j) + v_j(z_j) = u_{j+1}(z_j) + v_{j+1}(z_j) \tag{2.32}$$

$$\frac{ik_j}{m_j}u_j(z_j) - \frac{ik_j}{m_j}v_j(z_j) = \frac{ik_{j+1}}{m_{j+1}}u_{j+1}(z_j) - \frac{ik_{j+1}}{m_{j+1}}v_{j+1}(z_j) \tag{2.33}$$

Before we continue to describe the transfer matrix method, we have to discuss the influence of non-zero k_{xy} values on the relation between k_j and k_{j+1}.

If k_{xy} is zero, k_j and k_{j+1} are simply calculated by equation (2.29). For non-zero k_{xy}, the mass induced coupling between the parallel and vertical components of energy has to be taken into account. For better understanding, we first split the total energy E into a vertical component E_z and an energy component parallel to the barriers, E_{xy}. Thus, the total energy is: $E = E_{xy} + E_z$. While k_{xy} is always conserved, E_{xy} is not. Calculating E_{xy} in the regions (j) and (j+1) we get :

$$E_{xy,j} = \frac{\hbar^2 k_{xy}^2}{2m_j} \tag{2.34}$$

$$E_{xy,j+1} = \frac{\hbar^2 k_{xy}^2}{2m_{j+1}} \tag{2.35}$$

As the total energy has to be conserved, this simply means that E_z is no longer the same in the regions (j) and (j+1). The relation between $E_{z,j+1}$ and $E_{z,j}$ is given by:

$$E_{z,j+1} = E_{z,j} + (V_j - V_{j+1}) + (E_{xy,j} - E_{xy,j+1}) \tag{2.36}$$

From equation (2.36), the relation between k_j and k_{j+1} for non-zero k_{xy} can now be calculated as earlier:

$$k_j = \sqrt{\frac{2m_j(E_{z,j} - V_j)}{\hbar^2}} \tag{2.37}$$

$$k_{j+1} = \sqrt{\frac{2m_{j+1}(E_{z,j+1} - V_{j+1})}{\hbar^2}} \tag{2.38}$$

Having the relations between k_j and k_{j+1}, both for zero and non zero parallel momentum, we can now write equation (2.33) in matrix form:

$$\left(\begin{array}{c} u_j(z_j) \\ v_j(zj) \end{array} \right) = \mathbf{M}^{(j)} \left(\begin{array}{c} u_{j+1}(z_j) \\ v_{j+1}(zj) \end{array} \right) \tag{2.39}$$

where

$$\mathbf{M}^{(j)} = \frac{1}{2} \left(\begin{array}{cc} 1 + \frac{k_{j+1}m_j}{k_j m_{j+1}} & 1 - \frac{k_{j+1}m_j}{k_j m_{j+1}} \\ 1 - \frac{k_{j+1}m_j}{k_j m_{j+1}} & 1 + \frac{k_{j+1}m_j}{k_j m_{j+1}} \end{array} \right) \tag{2.40}$$

Note, that the matrix $\mathbf{M}^{(j)}$ does *not* depend on z. This information is solely comprised in the vectors consisting of u and v.

Because the potential and the mass between two sampling points are constant, the wave function in this area can be written as:

$$\left(\begin{array}{c} u_j(z_j) \\ v_j(z_j) \end{array} \right) = \mathbf{N}^{(j+1)} \left(\begin{array}{c} u_j(z_{j+1}) \\ v_j(z_{j+1}) \end{array} \right) \tag{2.41}$$

where

$$\mathbf{N}^{(j+1)} = \left(\begin{array}{cc} e^{-ik_{j+1}\Delta z_{j+1}} & 0 \\ 0 & e^{ik_{j+1}\Delta z_{j+1}} \end{array} \right) \tag{2.42}$$

The matrix $\mathbf{N}^{(j+1)}$ depends only on the distance $\Delta z_{j+1} = z_{j+1} - z_j$ between two sampling points, not on the location of a sampling point itself. The absolute position z is, again, only contained in the vectors consisting of u and v.

For the whole sequence of potential steps one can write:

$$\left(\begin{array}{c} u_0(z_0) \\ v_0(z_0) \end{array} \right) = \mathcal{M} \left(\begin{array}{c} u_n(z_n) \\ v_n(z_n) \end{array} \right) \tag{2.43}$$

where $\mathcal{M}$ is the product matrix of all $\mathbf{M}^{(j)}$ and $\mathbf{N}^{(j+1)}$:

$$\mathcal{M} = \mathbf{M}^{(0)} \cdot \mathbf{N}^{(1)} \cdots \mathbf{M}^{(n-1)} \cdot \mathbf{N}^{(n)} \tag{2.44}$$

equation (2.43) links the waves incoming on the potential $V(z)$ to the outgoing ones by means of a series of (2×2) matrices (equation (2.44)). The matrices $\mathbf{M}^j$ perform the connection of two parts of the global wave function across an interface, while the matrices $\mathbf{N}^{j+1}$ describe the propagation within a region of constant potential and constant (effective) mass.

Finally, to calculate the global transmission through the structure, one should demand, that $v_n = 0$, which means, that on the outgoing side of the structure just a transmitted wave exists. With this, the global transmission can be simply described by:

$$T(E) = \frac{|k_n|m_0}{|k_0|m_n} \frac{|A_n|^2}{|A_0|^2} = \frac{|k_n|m_0}{|k_0|m_n} \frac{1}{|\mathcal{M}_{11}|^2} \tag{2.45}$$

Note, that the transfer ratio of a barrier is defined as the ratio of the impinging and the transmitted electron currents. As the current is a vector, and for non-zero k_{xy} the current is not impinging vertically onto the barrier, the ratio of the absolute values of the k-vectors, $|k| = \sqrt{k_z^2 + k_{xy}^2}$, has to be used in equation (2.45).

Chapter 3

Organic semiconductors

3.1 Introduction

Recently there has been much interest in electronically functional organic materials with respect to various applications. In 1986 the first field effect transistor based on organic semiconductors was presented [93]. Shortly after that very efficient electro-luminescence from an organic thin film device [94], and a few years later the first polymeric light emitting diode [95] followed. Starting from these initial investigations the interest in organic semiconductors increased dramatically. The possibility of achieving highly efficient electroluminescence from thin films prepared by simple production techniques such as spin coating or dip coating opened up potential new fields in display and lighting technology.

Accordingly many applications including organic semiconductors have been reported: Organic thin film transistors [96, 97, 98, 99], organic light emitting diodes [95], photovoltaic cells [100, 101], sensors [102, 103], radio frequency identification tags [104, 105, 106] for integration into low cost, large area electronics [107]. The main advantages of using organic materials lie in the cost and processibility.

In contrast to inorganic materials that consist of covalent or ionic bonds of atoms over the entire expanse of solids, organic materials are based on independent molecules and characterised by weak intermolecular interactions. Therefore, designs of organic materials can be readily performed on the molecular level. In particular, organic π-electron systems have received attention as potential photo- and electro-active materials.
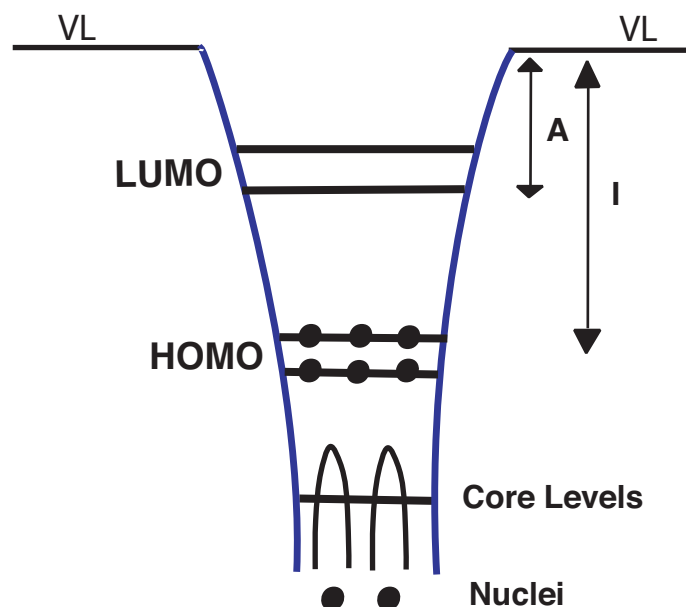
Figure 3.1: Electronic structure of a polyatomic molecule. VL is the vacuum level, A is the electron affinity and I is the ionisation energy.

3.2 The electronic structure of organic semiconductors

We start considering a polyatomic molecule. The atomic orbitals are deeply localised in the potential well. Figure 3.1 gives a pictorial representation of molecular orbitals. The effective potential well of an electron is formed by the atomic nuclei and other electrons. The wells of the nuclei are merged in the upper part to form a broad well. Deep atomic orbitals are still localized in the atomic potential well (core levels), but the upper atomic orbitals interact to form delocalized molecular orbitals. The outermost horizontal part of the potential well is again the vacuum level (VL). The energy separations from the highest occupied molecular orbital (HOMO) or lowest unoccupied molecular orbital (LUMO) to the VL are the ionization energy (I) or the electron affinity (A) of the molecule, respectively.

If we consider weak interactions between the molecules, like the Van der Walls interaction, than the picture that describe the organic solid is the one shown in Figure 3.2. Since the molecules interact only by the weak van der Waals interaction, the top part of the occupied valence states (or valence band) and the lower unoccupied states (conduction band) are usually localized in each molecule, with narrow intermolecular band widths of < 0.1
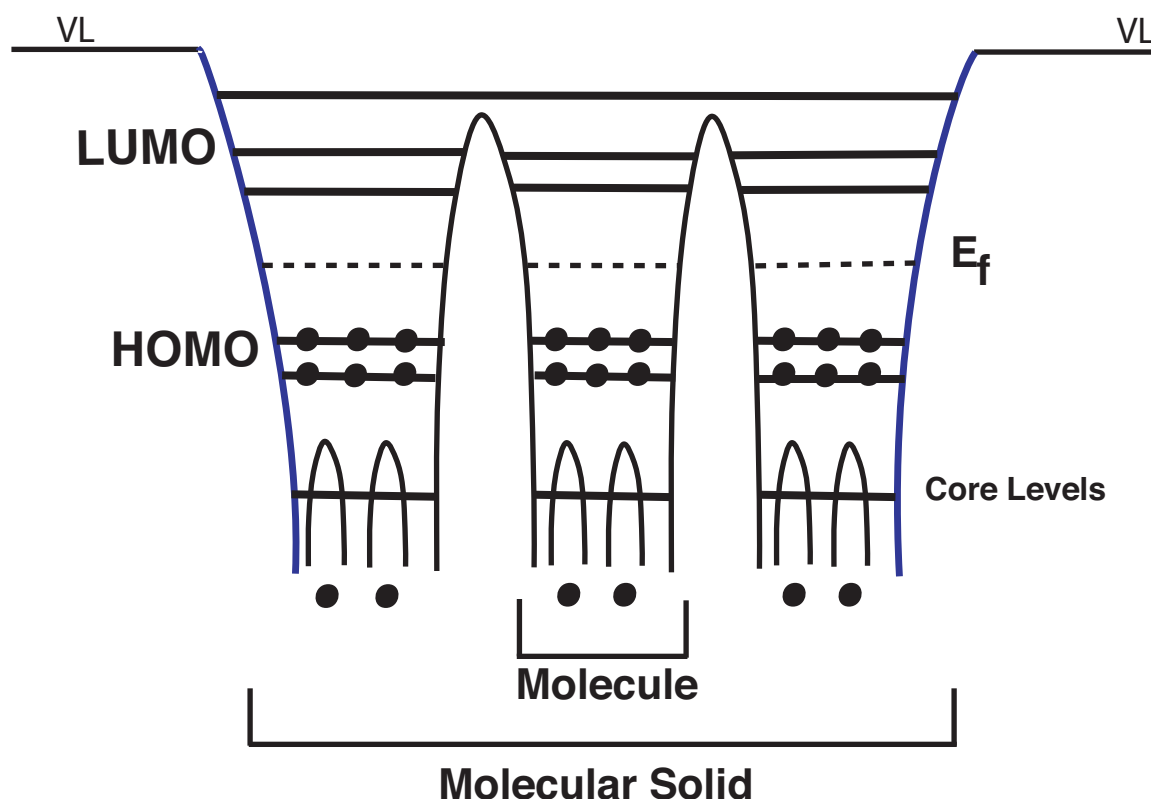
Figure 3.2: Electronic structure of an organic solid. VL is the vacuum level and E_f is the Fermi energy.

eV. Thus the electronic structure of an organic solid largely preserves that of a molecule or a single chain, and the validity of usual band theory (which assumes itinerant electrons) is often limited. The top of the occupied state and the bottom of the unoccupied state are often noted as HOMO and LUMO, reflecting the correspondence with the molecular state.

The situation in Figure 3.2 is often simplified to those in Figure 3.3 and even more simplified 3.4. In Figure 3.3 and 3.4, the Fermi level is also indicated (E_f). Since the electrons fill the energy levels following the Fermi statistics, the concept of Fermi level is always valid. The ionization energy (I) and electron affinity (A) of the solid are defined as the energy separation of the HOMO and the LUMO from the VL. The values of I and A are different from those of an isolated molecule due to a multielectronic effect. The work function Φ of the solid is defined as the energy separation between the Fermi level and the VL. The value of I can be determined by techniques such as ultraviolet photoemission spectroscopy and photoemission yield spectroscopy [108]. The entire valence
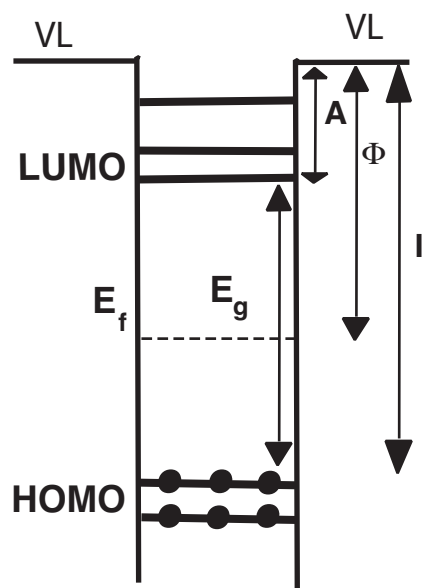
Figure 3.3: Simplification of the electronic structure of an organic solid. VL is the vacuum level, A is the electron affinity and I is the ionisation energy, Φ is the work function E_f is the Fermi energy, and E_g is the HOMO- LUMO bandgap.
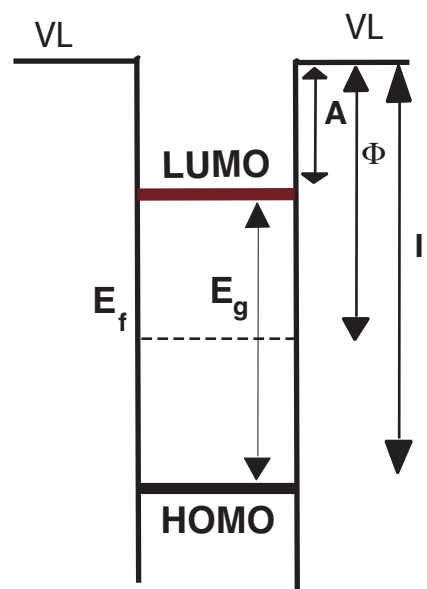

Figure 3.4: A more extended simplification of the electronic structure of an organic solid. VL is the vacuum level, A is the electron affinity and I is the ionisation energy, Φ is the work function E_f is the Fermi energy, and E_g is the HOMO- LUMO bandgap.

electronic structures can also be studied by ultraviolet photoemission spectroscopy and X-ray photoelectron spectroscopy [109].

More precisely, the optical bandgap E_g^{opt} is in general, different from the true bandgap (excitonic effect). It has to be also note that critical selection of various energy parameters is available for representative organic semiconductors.

3.3 Electronic structures at interfaces

An interface between the solids of two materials can be formed either by: a) the contact of two solids, or b) the deposition of one material on the solid surface of the other. The studies of interfaces in these views have been developed rather separately in the fields of electronic devices and surface science, at least for organic molecules. In the following, we attempt to combine the knowledge from these studies. Although we will primarily examine a metal/organic interfaces.

3.4 Energy level alignment at the interfaces

When a metal and an organic solid are far away, their energy levels are aligned sharing VL. When the solids come into contact without rearrangement of the electric charge, the organic layer is now in the potential of the surface dipole of the metal, and its energy levels are raised to have a common VL in an extremely narrow interfacial gap.

In the actual systems, a dipole layer may be formed right at the interface, due to various origins such as charge transfer across the interface, redistribution of electron cloud, interfacial chemical reaction, and other types of rearrangement of electronic charge [110, 111].

With such interfacial dipole formation, there will be an abrupt shift of the potential across the dipole layer.

This leads to the shift in VL in the organic layer at the right-hand side in Figure 3.6 from that of the metal at the left-hand side. Consequently, this factor has often been neglected in the field of organic devices. On the other hand, this possible shift of the VLs is well known in the field of surface science at the adsorption and deposition of molecules on metal surfaces [110, 111]. It is usually called the change in the work function (or surface potential) of the metal, and extensive studies have been carried out for small molecules
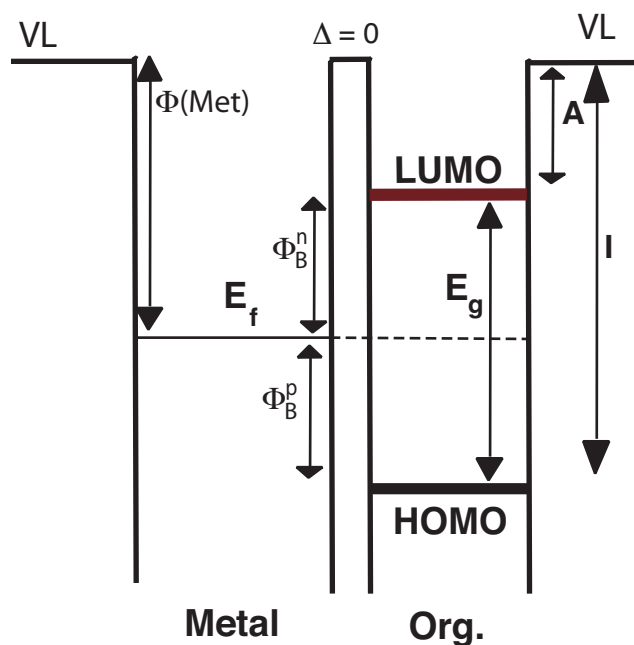
Figure 3.5: Schematic representation of assuming common vacuum levels at the interface. VL is the vacuum level, A is the electron affinity and I is the ionisation energy, Φ is the work function of the metal, E_f is the Fermi energy, E_g is the HOMO- LUMO bandgap, Φ_B^n and Φ_B^p denote the injection barriers for electrons and holes into the organic semiconductor. Δ is the interfacial dipole at the metal-organic interface which is assumed to be zero in that case.

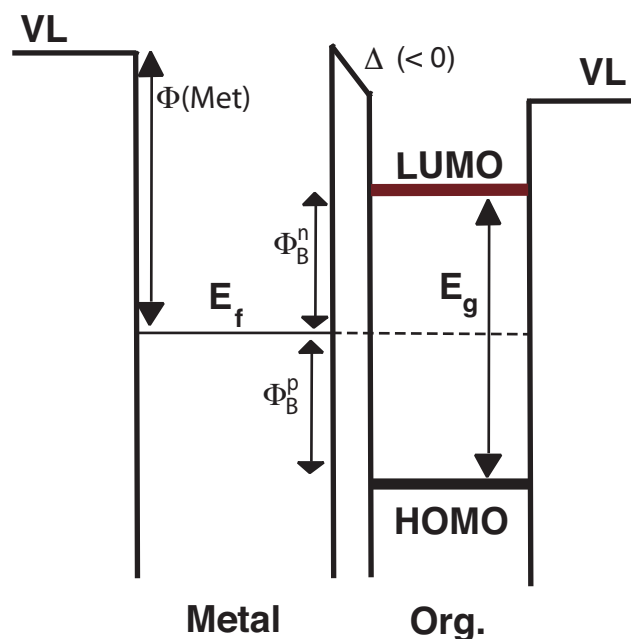Figure 3.6: Interfacial energy diagram with a shift of the vacuum level Δ at the interface due to the dipole layer formation. VL is the vacuum level, A is the electron affinity and I is the ionisation energy, Φ is the work function of the metal, E_f is the Fermi energy, E_g is the HOMO- LUMO bandgap, Φ_B^n and Φ_B^p denote the injection barriers for electrons and holes into the organic semiconductor. Δ is the interfacial dipole at the metal-organic interface.

[111]. Usually, controlled deposition in ultrahigh vacuum is a convenient way to examine the interfacial electronic structure [112]. Unfortunately, most of such studies for organic compounds have been limited in the thickness region of submonolayer to several layers, and not much work has been carried out in interfaces with thicker organic layers, which can be regarded as solids. Also, most studies of the work function change were carried out for small molecules, and electronically functional large molecules have not been extensively examined, although there were some exceptions.

3.5   Electron and hole injection barriers at interfaces

In the case of Figure 3.5 without interfacial dipole layer formation, the VL at the interface is common, and the barrier heights of carrier injection at the interface for hole Φ_B^h and electron Φ_B^h are given by:

$$\Phi_B^h = I - \Phi_m \tag{3.1}$$

$$\Phi_B^n = \Phi_m - A = E_g - \Phi_B^h \tag{3.2}$$

respectively, where Φ_m is the work function of the metal, I is the ionisation energy of the organic semiconductor, A is the electron affinity of the organic semiconductor, and E_g is the bandgap of the organic layer. Equations 3.1 and 3.2 are known as the the Schottky Mott rule [113], and correspond to the case of simple contacts. When this rule applies, we can deduce the barrier height from the values of Φ_m and I determined by techniques like ultraviolet photoemission spectroscopy. The injection barriers for the case with interfacial dipole, see Figure 3.6 are given by:

$$\Phi_B^h = I - \Phi_m - \Delta \tag{3.3}$$

$$\Phi_B^n = \Phi_m - A + \Delta = E_g - \Phi_B^h \tag{3.4}$$

where the case of depositing organic layer on metal has been considered. We see that the injection barrier is modified from the simple expectation of equations 3.1 and 3.2 by Δ. This modification is critically important for applications using carrier injection, such as electroluminescent devices [114, 115].

3.6 Carrier transport in organic semiconductors

For the dark and photoelectric conductivity of organic compounds it is decisive that the electronic carriers produced in primary or secondary processes can migrate through the solid. The essential transport mechanisms in organic semiconductors, tunneling and hopping are discussed in the following.

3.6.1 The tunneling mechanism

This mechanism, which has been first discussed by [116, 117], assumes that an electron, exited for example to the singlet state E_1, can tunnel through the potential barrier between the molecules and thus reach a non occupied term of the neighboring molecule [118, 119, 120]. Since the tunneling probability [121, 122, 123] is

$$W_T = DZ \approx 10^{11} - 10^{14} \, s^{-1} \tag{3.5}$$

(D is a transmission coefficient and Z is the number of impacts against the potential barrier) and the probability for an excited singlet state to return to the ground state is

$$k_R = \frac{1}{\tau_0} \approx 10^8 \, s^{-1} \tag{3.6}$$

from which follows:

$$\frac{W_T}{k_R} \approx 10^3 - 10^6 \,. \tag{3.7}$$

This means that the probability for an excited electron to reach its neighbor molecule is higher by a factor of 10^3 - 10^6 than the probability of a return to the ground state. The transition probability is still higher if a long-living triplet state is involved. The differences between electron and hole mobilities cannot be explained whiting the tunnel mechanism. The observed decrease of mobility with increasing temperature also disagrees with the mechanism of intermolecular tunneling.

Thus the tunnel effect permits only an incomplete description of the carrier transport through the organic solid. Nevertheless we see that, in spite of the potential barriers between the molecules, an excited electron may tunnel over distances of many molecules.

3.6.2 Hopping

In organic solids with broad intermolecular potential barriers ($a > 10$ Å) electrons cannot tunnel from one molecule to the neighboring molecule, but they can reach it by the so called hopping mechanism. The hopping probability is

$$W_H = \nu_j \exp(-\Delta E_j/kT),$$ (3.8)

where ΔE_j is the barrier height and ν_j is a frequency factor which depends on the exchange energy

$$J = J_0 \exp(-\frac{a}{r})$$ (3.9)

to be derived from electron paramagnetic resonance (EPR) or electron spin resonance (ESR) measurements according to

$$\nu_j = \frac{J}{2h}.$$ (3.10)

In the above equations 3.9 and 3.10 r is the effective electron radius, a is the width of the intermolecular barriers and h is Plancks constant. On the basis of Einstein's relation between the mobility μ and the Diffusion D:

$$\mu = \frac{e}{kT}D,$$ (3.11)

one gets with $D = W_H a^2$ and Equations 3.8 and 3.9

$$\mu_j = \frac{a^2 e}{kT}W_H = \frac{a^2 e}{kT}\nu_j \exp(-\Delta E_j/kT),$$ (3.12)

or

$$\mu_j = \mu_{j_0} \exp(-\Delta E_j/kT),$$ (3.13)

where $\nu_{j_0} = \frac{a^2 e}{kT}$. Measurements on inorganic semiconductors, e.g. selenium, NiO, etc. [124, 125] confirm the temperature dependence of mobility to be expected from equation 3.13.

With the assumption of hopping mechanism, equation 3.10 and 3.12 yield for the conductivity ($\sigma = en\mu$):

$$\sigma = A_0 n \frac{a^2 e J}{2hkT} \exp(-\Delta E_j/kT) \,, \tag{3.14}$$

where A_0 is an anisotropy factor. Because of the localization of the electrons, n in equation 3.14 corresponds to the molecule concentration in the case of compounds dissolved in a neutral matrix.

Strictly speaking, the activation energy of conductivity has two components: The energy ΔE_j necessary to overcome the intermolecular potential barriers potential barrier, and a constitution dependent energy ΔE supplied to the individual molecules during thermal or optical excitation of the electrons. With polymers ΔE can tend to zero as the individual conjugation zones grow, while the activation energy of conductivity may be high and carriers mobility may be low because of the potential barriers separating the conjugation zones. With $n = N \exp(-\Delta/2kT)$ and equation 3.13 this fact is described by [126]:

$$\sigma = en\mu = eN \exp(-\frac{\Delta E}{2kT}\nu_{j0} \exp(-\Delta E_j/kT) \,, \tag{3.15}$$

from which follows:

$$\sigma = eN\mu_{j0} \exp\left[-\frac{(\Delta E + 2\Delta E_j)}{2kT}\right] \,, \tag{3.16}$$

With decreasing intermolecular distances tunneling of electrons is facilitated. As a consequence, the hopping mechanism is replaced by a carrier transport according to the band theory [127]. The upper limit of the hopping process therefore agrees approximately with the lower limit of the band model.

3.7 Some of the most studied organic molecular semiconductors

Some of the most widely investigated molecular semiconductors are presented, they belong to the families of the following.

3.7.1 Oligoacenes

Oligoacenes [128, 129] are a class of materials, which has been studied for several decades [130], and currently provides among the best semiconductors in the field of organic electronics. The class of oligoacenes consists of benzen-rings, e.g. naphtalen ($n = 2$), anthracen ($n = 3$), tetracene ($n = 4$) see Figure 3.7, and pentacene ($n = 5$) see Figure 3.8. Special attention has been given to tetracene, pentacene, and derivatives, which have well-defined crystal structures [131].
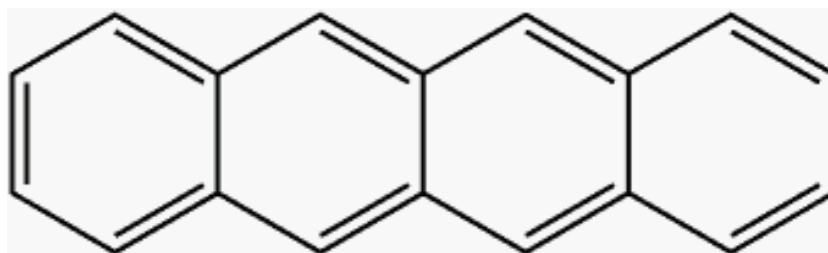

Figure 3.7: Chemical structure of tetracene. Tetracene consists of 4 benzen rings.

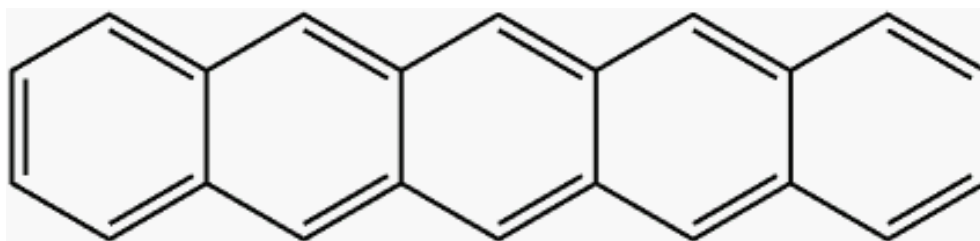Figure 3.8: Chemical structure of pentacene. Pentacene consists of 5 benzen rings.

Pentacene exhibits several crystal polymorph's, which has proven useful to investigate crystal structure transport relationships [132]. Among the derivatives of the oligoacenes, rubrene (a tetracene molecule substituted by four phenyl rings see Figure 3.9 for molecular structure) has been the midpoint of many recent studies [133, 134, 135, 136, 137].
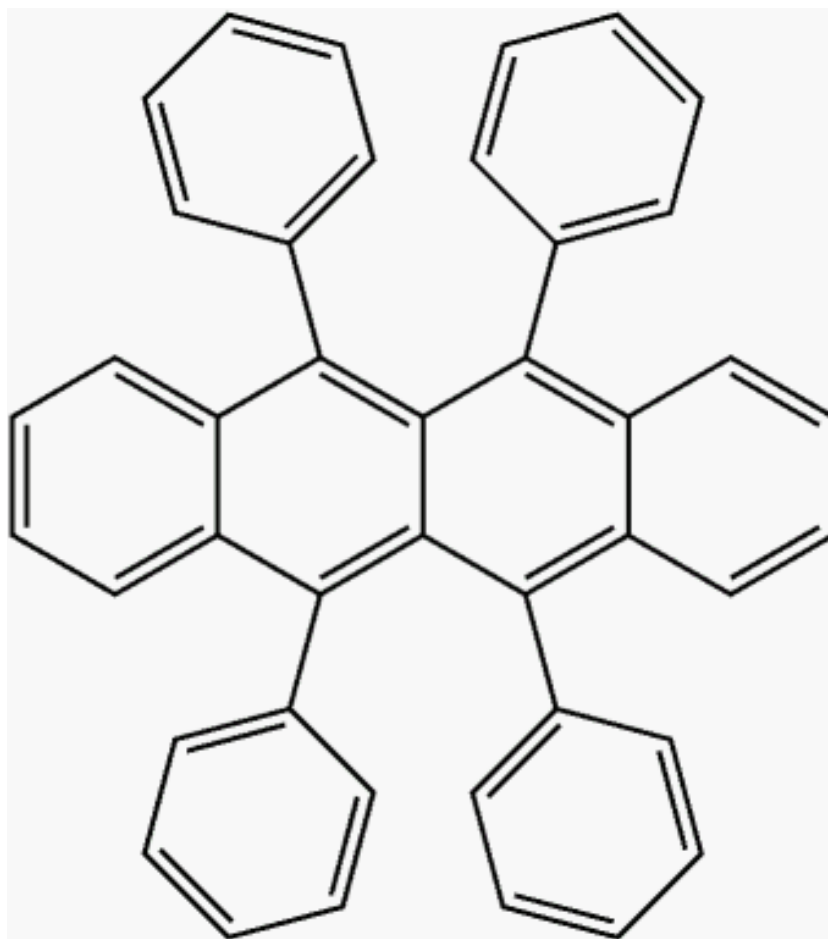
Figure 3.9: Chemical structure of rubrene. Rubrene is a tetracene molecule substituted by four phenyl rings.

3.7.2 Oligothiophenes

The molecular structure of a simple oligothiophene is given in Figure 3.10. The crystal structures for oligothiophenes [138, 139, 140] are available for the $n = 2, 3, 4, 5, 6$ and 8 oligomers and a number of substituted derivatives.

The class of the oligothiophenes is of special interest because ever since the first organic transistor, built with sexithinyl ($n = 6$) as the active semiconducting material, was reported [141]. Usually most oligothiophene and oligoacene compounds are used as p-type materials (that is, as hole transporters), their backbone can derivatized with fluorinated substituents to yield efficient n-type materials (electron transporters) [142, 143, 144, 145].
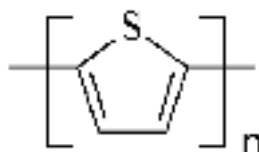
Figure 3.10: Chemical structure of oligothiophenes. Oligothiophenes are available for the $n = 2$, 3, 4, 5, 6 and 8 oligomers and a number of substituted derivatives.

3.7.3 Discotic liquid crystals

Discotic liquid crystals [146] are based on 2 dimensional, disc-like molecules made of a central conjugated core substituted by saturated chains on the periphery. In the discotic phase, these molecules organize in the form of quasi 1 dimensional colums that provide 1 dimensional pathways for electron and/or hole transport (the n- or p-type character can be tuned as a function of the nature substituents). Systems representative for discotic liquid crystals are triphenylene (for molecular structure see Figure 3.11), hexabenzocoronene, perylenediimide, and metal phthalocyanine (for molecular structure see Figure 3.12) cores.

Nevertheless the absence of crystalline order, mobility values in the order of 0.4 cm^2/Vs have been reported in discotic phases of hexabenzocoronene derivatives [147]. Investigations about transport in liquid crystals formed by rodlike molecules have also been reported [148, 149].

3.7.4 Triphenylamines

Triphenylamines compounds such as the prototypical 4,4'-bis(N-m-tolyl-N-phenylamino)biphenyl (TPD, for molecular structures of some TPD's see Figure 3.13) molecule, have a long history as organic photoconductors in the Xerox industry [150]. These compounds have also been extensively used in organic light emitting diodes as hole-transporting materials under the form of vacuum-deposited amorphous films [151].

3.7.5 Perylenes

Perylene exhibits a peculiar crystal packing in which dimers and not single molecules are arranged in an herringbone fashion [152]. The attachment of dianhydride moieties lieds to
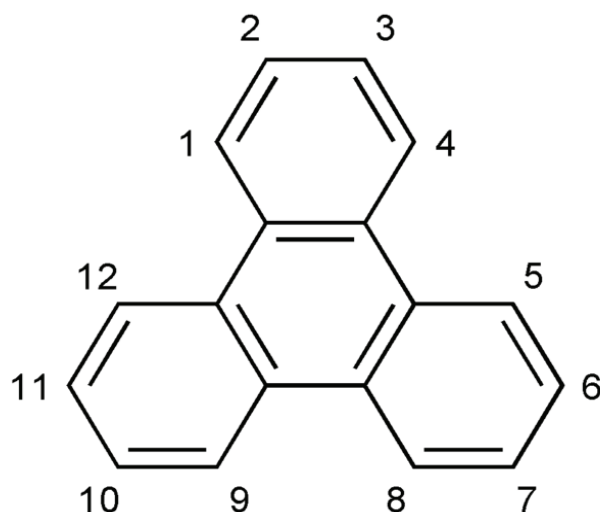
Figure 3.11: Chemical structure of triphenylene.

perylene-3,4,9,10-tetracarboxylic-dianhydride (PTCDA) and 3,4,9,10-perylene-tetracarboxylic-diimide (PTCDI) (molecular structure can be seen in Figure 3.14), both compounds have good n-type properties [153].

3.7.6 Tetrathiafulvalenes

Tetrathiafulvalenes and derivatives belong to the organic semiconductors which have been initially widely investigated as donor entities in highly conducting charge-transfer salts [154, 155]. There has been work extended to their transport properties in thin films and crystals [156, 157, 158].

Figure 3.12: Chemical structure of metal phthalocyanine.

3.7.7   Fullerenes

The interest in fullerene (C_{60} molecular structure see Figure 3.15) and derivatives [159, 160] stems for their extensive use as e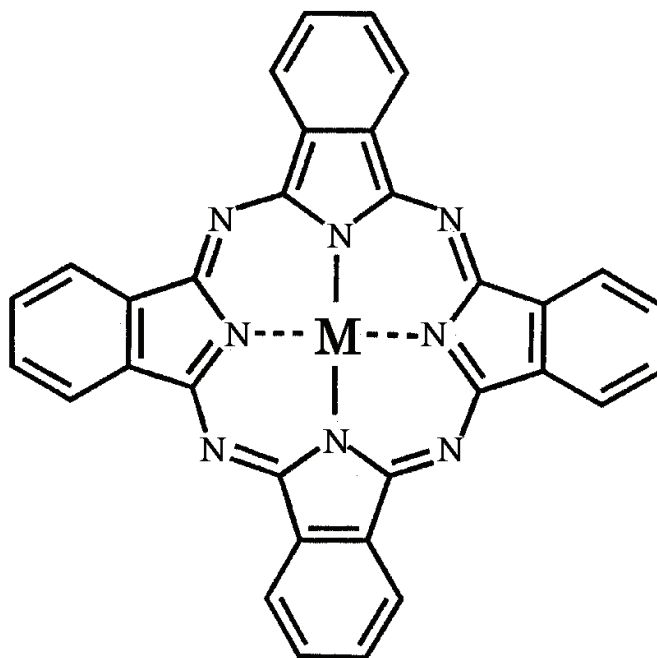lectron acceptors in organic blends for photovoltaics. It also has to be noted that in the case of single-wall carbon nanotubes, ballistic transport has been measured with carrier mobilities on the order of 80 000 cm^2/Vs [161]. Ballistic transport implicates that the carrier mean free path is longer than the nanotube.

Conjugated polymer chains have also been the focus for many scientists. Charge transport in conjugated polymer chains has been investigated intensely. For totally disordered polymer films, charge mobilities are small, namely in the range of 10^{-6} - 10^{-3} cm^2/Vs. Usually the mobilities increase significantly when the polymer chains present self-assembling properties that can be exploited to generate ordered structures [162]. Via introduction of a liquid crystal character high mobilities can also be achieved [163, 164].

Among the above listed organic semiconductors also the most studied organic polymeric semiconductors will be listed in the following.
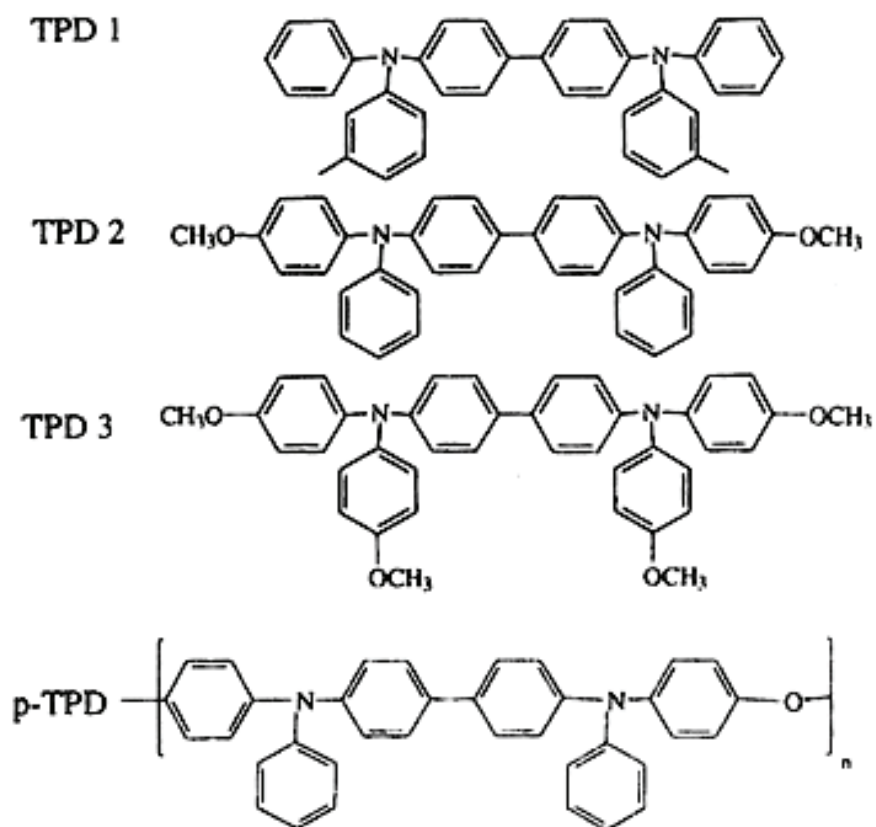
Figure 3.13: Chemical structure of 4,4'-bis(N-m-tolyl-N-phenylamino)biphenyl's (TPD's).

3.7.8 Polyparaphenylene and Polyparaphenylenevinylene

Polyparaphenylene (PPP), polyparaphenylenevinylene (PPV) and their derivatives were initially the focus of many experimental and theoretical studies in view of their high luminescense quantum yield in the solid state, which is feature of major interest for light-emitting applications. [95, 165].

The molecular structures of PPP and PPV can be seen Figures 3.16 and 3.17 respectively.
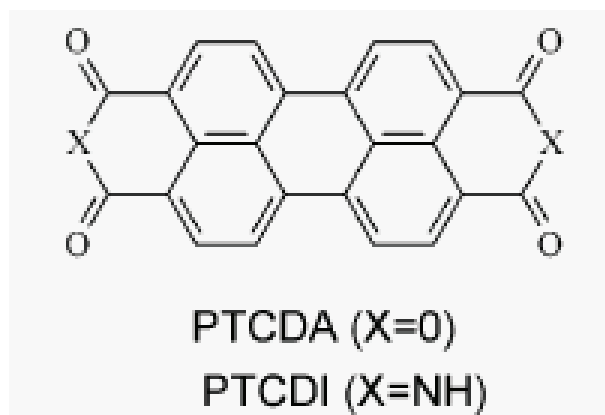
Figure 3.14: Chemical structure of perylene-3,4,9,10-tetracarboxylic-dianhydride (PTCDA) for X=O and 3,4,9,10-perylene-tetracarboxylic-diimide (PTCDI) for X=NH.

3.7.9 Polyfluorene

Polyfluorene (PF) and some of it's alternating copolymers represent a new generation of materials of light emitting polymers with high purity and stability [166]. For

The molecular structures of PF and PF copolymers can be seen Figures 3.18 and 3.19 respectively.

3.7.10 Polythiophene

The regio-regular alkyl-substituted polythiophene (PT) and derivatives display currently among the highest mobilities (around 0.1 cm^2 /Vs) due to their packing in well-organized lamellae [162]. There have been reports on even higher mobilities on the order of 0.6 cm^2 /Vs for PT derivatives incorporating fused thiopehene rings [163].
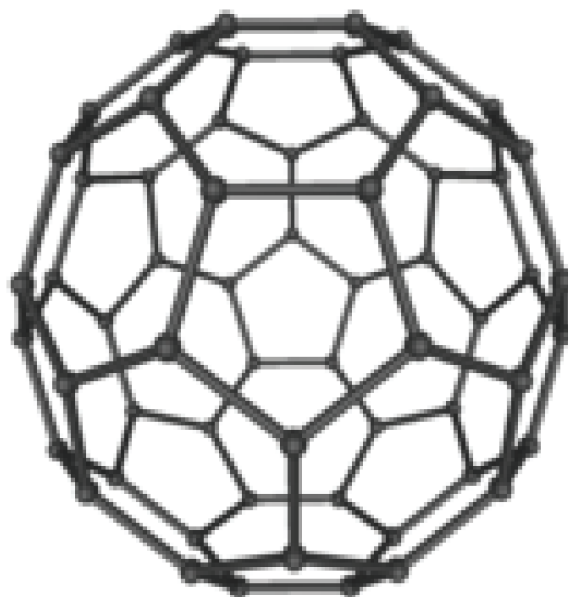
Figure 3.15: Chemical structure of fullerene C_{60}.
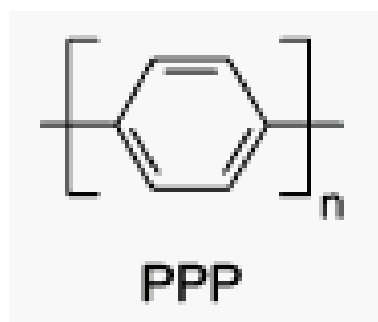
Figure 3.16: Chemical structure of Polyparaphenylene (PPP).

3.7.11 Discussion

Polymers which are π-conjugated are generally exploited as p-type materials. But Polymers with high electron affinity such as the poly(benzobisimidabenzophenanthrolines) [167], can be used as n-type semiconductors. It is important to bear in mind that the characterization found in the literature of an organic semiconductor as p-type or n-type most often not reflect the intrinsic ability of the material to transport holes or electrons; mostly it rather translates the easy way with which holes or electrons can be injected into the material from the electrodes. Theoretical investigations of the past few years found in the literature [168, 169], points to the conclusion that, in many organic semiconductors, the electron and
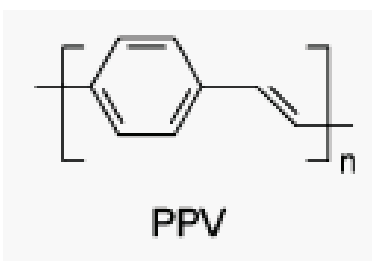
Figure 3.17: Chemical structure of polyparaphenylenevinylene (PPV).
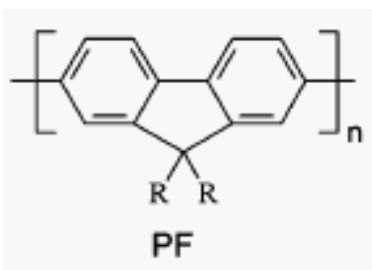
Figure 3.18: Chemical structure of Polyfluorene (PF).

hole mobilities are expected to be comparable. Usually, the observation of a low n-type mobility is generally the consequence of extrinsic effects, such as the presence of specific traps for electrons (due to photo-oxidation of the π-conjugated backbone) or the instability of radical-anions with respect to water, hydroxyl groups, or oxygen [170, 171], which was very nice demonstrated by [172]. It was shown in the literature that SiO_2, commonly used as gate dielectric in organic field-effect transistors (OFETs), presents a large number of hydroxyl groups on its surface, which act as traps for electrons injected into the organic semiconductor channel [172].

Charge transport through organic semiconductors requires that the charges be able to move from molecule to molecule and to be trapped or scattered to be efficient. This is the reason why charge carrier mobilities are influenced by many factors including molecular packing, disorder [136, 173, 96, 174, 175, 176, 177, 178, 179, 180, 181, 182, 183, 184, 185, 186, 187, 188, 189, 190, 191], presence of impurities [192], temperature [193, 194, 133, 137, 182, 183, 195, 196, 197], electric field [198, 133, 199, 200, 201, 202, 203], magnetic field, charge-carrier density [204], molecular size or molecular weight [205, 168, 196, 206, 207], pressure [208, 204, 209], etc. . Now a few impacts of these parameters on charge transport in organic semiconductors will be discussed.
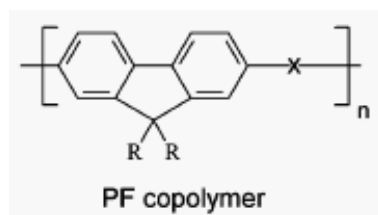
Figure 3.19: Chemical structure of Polyfluorene (PF) copolymers.
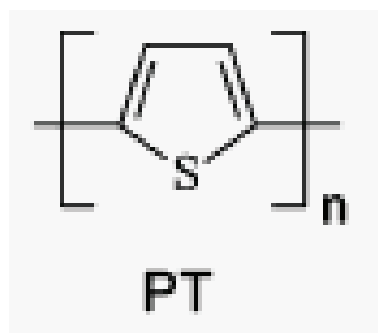
Figure 3.20: Chemical structure of Polythiophene (PT)

Anisotropy of charge transport in single crystals points out that the efficiency is intimately related to the relative positions of the interacting molecules, and hence to crystal packing. In the most circumstances, unsubstituted π-conjugated molecules crystallize into a layered herringbone packing. A packing like this causes 2 dimensional transport within the stacked organic layers [96] while transport between layers is less efficient. Generally the anisotropy is measured by orienting the crystal along the two axes defining a layer. It has been shown in an elegant approach that by laminating an organic crystal onto a transistor stamp one can build an OFET [136]. This approach allows for multiple relamination steps with the same material and has been exploited with a rubrene single crystal to measure the mobility in multiple directions within the herringbone layer. The mobility anisotropy has also been characterized experimentally for a pentacene single crystal contacted by an electrode array [173].

Information about charge-transport parameters in organic semiconductors can be found in Refs. [210, 130, 144, 211, 212, 213, 214, 215, 216, 217, 218, 219, 220, 221, 222, 223, 224, 225, 226, 227, 228]

3.8   The organic semiconductor titanylphthalocyanine

Titanylphthalocyanine ($C_{32}H_{16}N_8OTi$, TiOPc) is a phthalocyanine with the titanoxide (TiO) group protruding from its centre plane (for the molecular structure see Fig. 3.21).
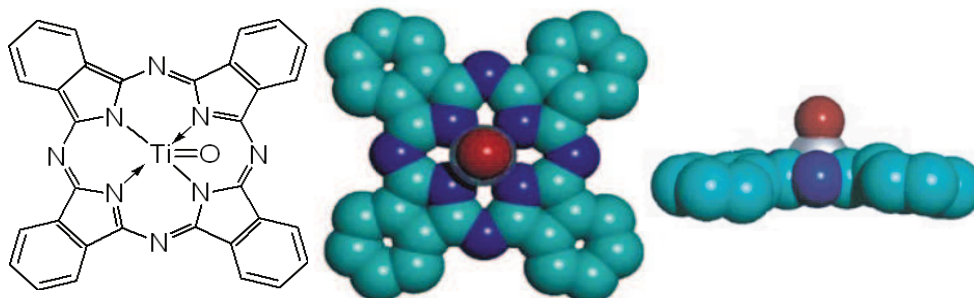
Figure 3.21: Molecular structure and space-filling model of titanylphthalocyanine, top and side view.

In the solid state, so far, five different crystal structures are known [229]. A very interesting property of TiOPc is that its optical absorption depends strongly on its crystal phase. This allows the identification of the different crystal phases, to a certain extent, by optical absorption measurements without the need of X-ray diffraction measurements [230]. Many metallophthalocyanines [231] have strong absorption and good photoconductivity in the near infrared (700 - 900 nm), which facilitates their use as photoconductors in diode laser-based printers [232, 233, 234], in generall metallophthalocyanines [235, 236], copperphthalocyanine [237], vanadylphthalocyanine [238, 239], chloroindiumphthalocyanine [240], indiumphthalocyanine [241], magnesiumhthalocyanine [242], and of course TiOPc have been studied due to deir low cost, nontoxicity, photosensitivity and stability. Especially TiOPc has become of special interest for many scientists all over the world due to its photogenerating properties when exposed to infrared light. This photogenerating activity in the near infrared makes it of use in photoreceptors designed for use in laser printers and digital copiers equipped with light emitting diode-arrays or laser diodes. Additionally TiOPc is of special interest namely for many research areas as: impact of an interface dipole layer on molecular level alignment at an organic-conductor interface [243], analysis of the substrate influence on the ordering of epitaxial molecular layers [244], organic-inorganic heteroepitaxial growth of molecules on crystalline substrates [245], space charge distribution of TiOPc films on metal electrodes [246], electronic sensory behaviour of TiOPc [247],

crystallization on substrates [230, 248], quasi-instrinsic semiconducting state of TiOPc films [249], and atmospheric effect of TiOPc films of doping, band bending and Fermi level alignment [49, 250, 251, 252].

3.9   The organic semiconductor hexa-*peri* hexabenzo-coronene

Hexa-*peri* hexabenzocoronene ($C_{42}H_{18}$, HBC, structural formula shown in Fig. 8.2) is a large flat hydrocarbon with very interesting electric properties [147, 253]. The most important energy characteristics of many-electron π systems, in particular of large polycyclic aromatic hydrocarbons, is the energy gap. Values for the bandgap of HBC can be found in the literature [254, 255]. In [254] there is a transport gap of $E_g^{elec}(HBC) \sim 3.2$ eV, an optical transport gap of $E_g^{opt}(HBC) \sim 2.8$ eV, ionization energy of $I = 5.9$eV and in [255] a value of $E_g^{opt}(HBC) \sim 2.7$ for the optical gap with a exciton binding energy of 0.5eV, including a interfacial dipole layer of $\Delta \sim -0.8$ eV. In this work a electronic transport bandgap of 3 eV is used for HBC.
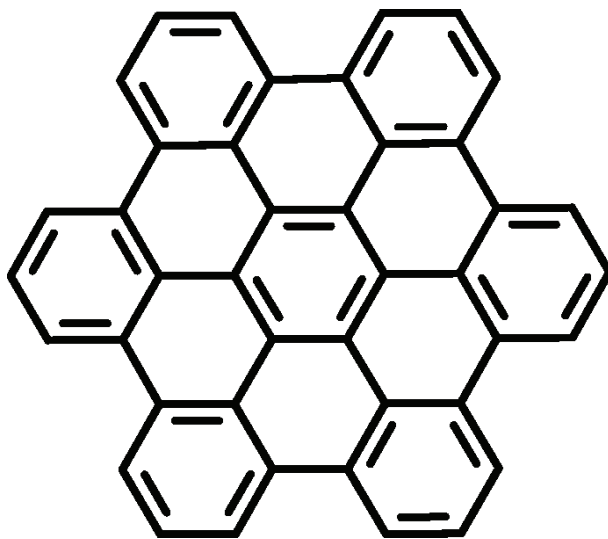
Figure 3.22: Molecular structure formula of hexa-*peri* hexabenzocoronene ($C_{42}H_{18}$, HBC)

HBC is often used as a relatively simple model compound, it can be found in the literature that HBC can be grown in large ordered domains [256, 257, 183]. Since HBC is used as a model compound there is a lot of investigations on the properties of HBC done as: ultraviolet photoelectron spectroscopy [255, 254], self assembly at surfaces [258, 259], electronic properties [253, 260], ordered architectures of HBC at surfaces [261], nanophase segregation and rectification in monolayers of functionalized HBC [262], observation of organic-organic heteroepitaxy [263, 264, 256], and charge transport in HBC [147, 265].

Chapter 4

Ballistic Electron Emission Microscopy/Spectroscopy on Au/Titanylphthalocyanine/GaAs Heterostructures

Au/titanylphthalocyanine/GaAs diodes incorporating ultra smooth thin films of the archetypal organic semiconductor titanylphthalocyanine (TiOPc) were investigated by Ballistic Electron Emission Microscopy/Spectroscopy (BEEM/S). Analyzing the BEEM spectra, we find that the TiOPc increases the BEEM threshold voltage compared to reference Au/GaAs diodes. From BEEM images taken we conclude that our molecular beam epitaxial (MBE) grown samples show very homogeneous transmission, compare to wet chemically manufactured organic films. The barrier height measured on the Au- TiOPc-GaAs is $V_b \approx 1.2 \text{eV}$, which is in good agreement with the data found in reference [49]. The results indicate that TiOPc functions as a p-type semiconductor, which is plausible since the measurements were carried out in air [230].

4.1   Introduction

In recent years, organic semiconductors have attracted much interest due to their variety of interesting optical, electrical and photoelectric properties. Photo- and electro-active organic materials have been the subject of recent attention including organic semiconductors,
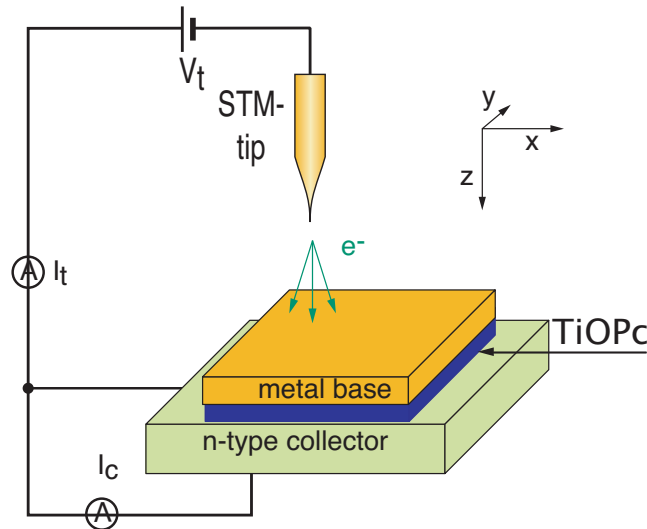
Figure 4.1: Schematical sketch of the BEEM setup with two interfaces: first the metal organic semiconductor interface and second the organic semiconductor n-type semiconductor interface. In this case the organic semiconductor is TiOPc. The tunnel voltage V_t is applied between the STM tip and metal surface of the sample, the tunnel current I_t in this circuit is kept constant by the STM feedback loop. A second amperemeter measures the ballistic current I_c between the metal base and semiconductor collector. The arrows symbolise the electrons emitted from the STM tip.

organic light emitting diodes [266, 267], organic field effect transistors [268, 106], or photovoltaic devices [269, 270]. In addition, organic semiconductors are already widely used in xerography, plate making printings and laser printers. Physicists and chemists have focused on the charge transfer phenomena of organic molecules and polymer organic semiconductors in the field of organic solar cells during the past decade. Besides these applied aspects there are important features motivating basic research, namely the interface properties between semiconductors and organic films e.g. the deformation of the bandstructure at the interfaces.

4.2 Experimental

Ballistic-electron-emission microscopy (BEEM) [4, 3] is a three terminal extension of scanning tunneling microscopy (STM) [1, 2], where electrons tunnel between the STM tip and

a thin Au film evaporated on a semiconductor surface such as Si or GaAs. Figure 4.1 shows a sketch of the experimental setup. Between the Au-base and n-type GaAs a thin film of TiOPc is located.

If the electron energy is high enough to overcome the Schottky barrier height at the metal-semiconductor interface then the electrons can penetrate ballistically into the semiconductor, this causes a current, which is measured with the third electrode on the backside of the sample. By sweeping the applied tip voltage BEEM current spectra can be obtained. By mapping the BEEM current for a constant tip bias while scanning the sample surface, images can be taken with a spatial resolution of about 1 nm. Over the last two decades BEEM became a well-established technique to determine Schottky barrier heights (SBH) and subsurface band offsets. An overview of this technique can be found in detail [271, 272, 70].
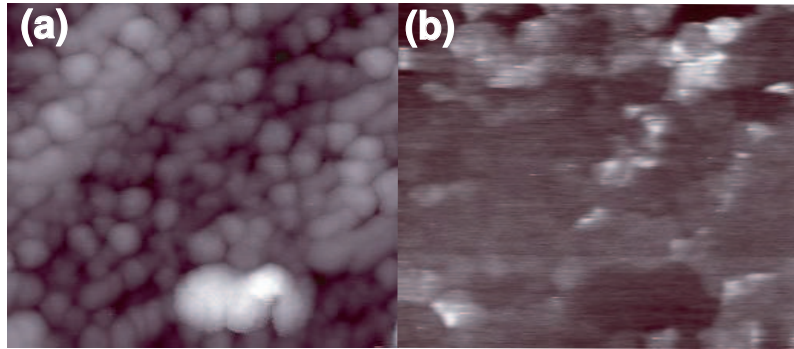
Figure 4.2: (a) STM topographic image of Au/TiOPc/GaAs heterostructure, recorded at $T = 300$K, $I_t = 5$nA, $V_t = 1.4$V. (b) Corresponding BEEM image (recorded simultaneously with the STM image, color scale corresponds to $0 \ldots 1$pA .

To guarantee good internal sample resistance and optimized BEEM signals, molecular beam epitaxial (MBE) grown GaAs samples were used as substrates. In detail, low doped ($N_D \approx 1 \times 10^{16}$ cm^{-3}) GaAs layers ($d = 1\mu$m) were grown on an n^+-wafer. On these substrates, TiOPc-films ($d \approx 6$ monolayers) were grown with organic MBE. Finally, a 7 nm Au layer was evaporated on the samples. From BEEM images taken we conclude that the samples are very homogeneous, in contrast to wet chemically manufactured organic films.

4.3   Results and Discussion

At first the BEEM-images are presented. Then the BEEM spectra and the analysis to extract the Schottky barrier height are presented.
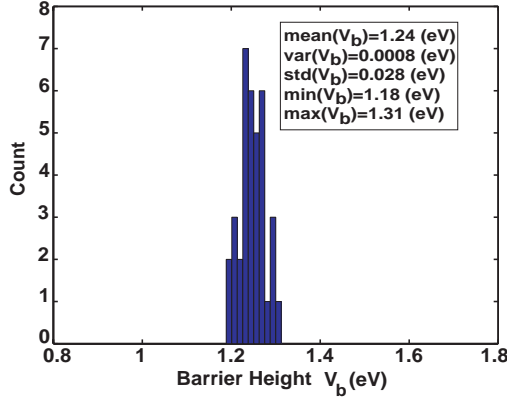
Figure 4.3: Histogram of the measured barrier height of Au/TiOPc/GaAs (sample A).
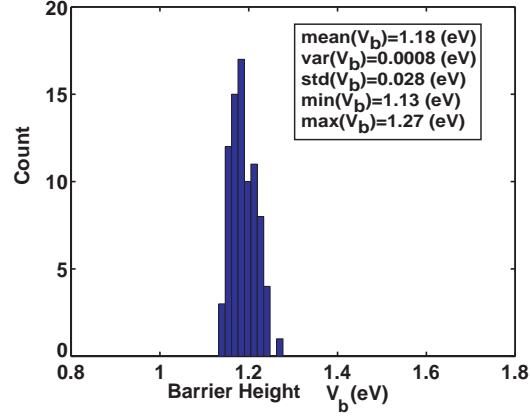
Figure 4.4: Histogram of the measured barrier height of Au/TiOPc/GaAs (sample B).

Figure 5.1a shows the topographic STM image and Figure 5.1b the corresponding BEEM image of our Au/TiOPc/GaAs sample. The BEEM image was obtained simultaneously at a tip bias (V_t) of 1.4V and a tip current (I_t) of 5nA, with a scan area of 200nm ×200nm. The STM constant current image shows the typical or characteristic granular structure of Au. In the corresponding BEEM image,brighter areas indicate an enhanced electron transmission. Features visible in the BEEM image correlate exclusively with the granular structure and the topographic features of the Au-film and can not be correlated to the organic film underneath. Therefore we think, that our MBE grown TiOPc-film is very homogeneous, compare to wet chemically manufactured organic films.

To investigate the transmission behavior of TiOPc, we systematically measured ballistic electron spectra on various positions of our sample. The BEEM current is on different positions of the sample distinct. This can seen very clearly in Figure 4.5. In Figuer 4.5 are three different spectra taken at various positions plotted. One can see very clearly that curve 1 in Figure 4.5 has the the highest amount of BEEM current and the curve 3 in Figure 4.5 has the lowest BEEM current. But they all three have almost the same current onset, which is marked with the arrow in Figure 4.5.
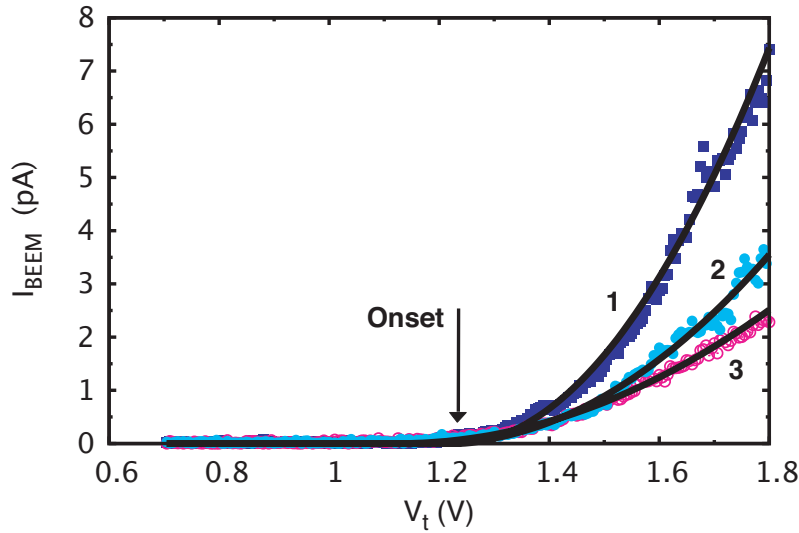
Figure 4.5: Raw BEEM spectra taken at different positions of the sample. Curve 2 shows the highest BEEM current and curve 3 the lowest.

To extract the barrier height, i.e. the onset voltage, from the measured data, we use a quadratic power law fit (see, e.g. [271]).

$$I_{BEEM}(V_t) = \alpha(V_t - V_b)^2 \quad . \tag{4.1}$$

The fit-formula used to analyse the experimental data is shown in equation 4.1. α and V_b are fit-constants, V_b is the fitted onset. The Bell-Kaiser model was not used because already the straightforward power law, despite of its simplicity, fits our data very well and is completely sufficient for our purposes. The barrier height values gained from the power fit are 1.24 eV and 1.18 eV for sample A and B. The histograms of the two samples are in Figure 4.3 and 4.4.

We measured an effective barrier height of Au/TiOPc/GaAs it must be pointed out that at present, we can not decide if the measured barrier height is the barrier of the Au-TiOPc interface or the barrier of the TiOPc-GaAs interface or a combination of both. It is clear that is not the Schottky barrier height of Au/GaAs interface, because the onset we measured is significantly higher than 0.9eV.

The solid line in Figure 4.6 shows averaged BEEM spectra ($I_t = 5$nA, T$= 300$K) and the dashed line is its first derivative taken of over 100 individually BEEM spectra. The spectra are taken over the a voltage-range of 0.8 to 2.3 V.
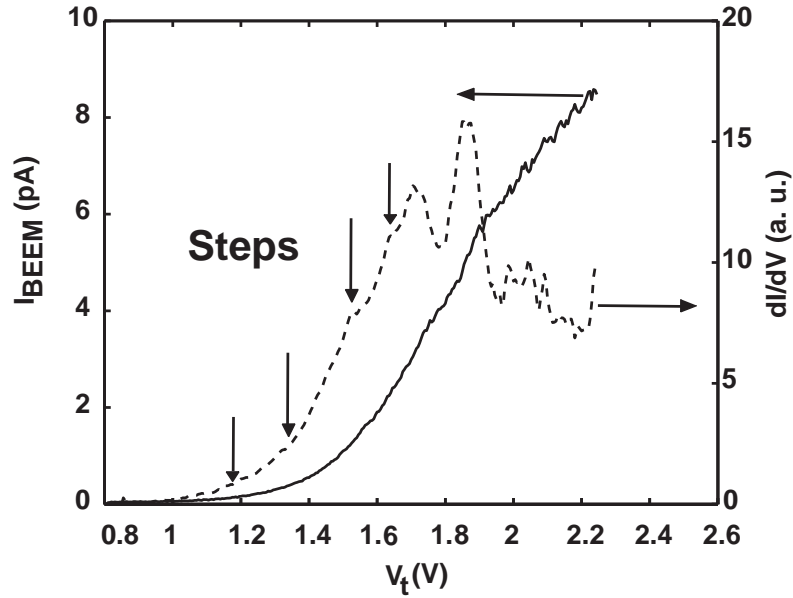
Figure 4.6: Averaged BEEM spectra (solid line) and its first derivative (dashed line) from Au/TiOPc/GaAs. Multiple features are clearly visible in the first derivative.

Above the onset several features are visible, three steps at the points: 1.34, 1.52 and 1.61V. The same behavior of metal-organic interfaces was also found in [37, 36, 38]. Besides these features there are two significant peaks at 1.7 and 1.85V. Above 2.3V the data were not reliable, because of the increased signal to noise ratio.

4.4   Conclusion

Due to the BEEM images, it can be concluded that the samples are very homogeneous, in comparison to wet chemically manufactured organic films. All features visible in the BEEM images of our samples correlate exclusively with the granular structure and the topographic features of the Au-film and cannot be correlated to the organic film underneath. Analyzing the BEEM spectra we find that the TiOPc increases the BEEM threshold voltage compared to reference Au/GaAs diodes, which was also found in [39], where a BEEM study on a Au/Molecule/n-GaAs diode was done. The barrier height measured on the Au-TiOPc-GaAs is $V_b \approx 1.2eV$, which is in good agreement with the data found in references [49]. The results indicate that TiOPc functions as a p-type semiconductor, which is

plausible since the measurements were carried out in air [230]. In addition, the derivative of the BEEM spectra shows multiple features in the energy regime above the LUMO level [230]. Possible origins of these features are currently under investigation.

Chapter 5

Ballistic Electron Transport Through Titanylphthalocyanine Films

In this chapter BEEM investigations of the Au/TiOPc/GaAs heterostructure are presented. The Schottky barrier height of Au on TiOPc was studied as a function of temperature. MBE grown films of TiOPc were incorporated into the base layer of a BEEM sample on GaAs. TiOPc-films (nominal thickness of about 6 and 10 monolayers, corresponds to about 19 Åand 32 Å) were grown using organic MBE. The thicknes of the Au layer is 7 nm.

5.1 Results and Discussion

Figure 5.1 (a) shows the topographic STM image and Figure 5.1 (b) the corresponding BEEM image of our Au/TiOPc/GaAs sample. The BEEM image was obtained simultaneously at a tip bias (V_t) of 1.4 V and a tip current (I_t) of 5 nA, with a scan area of 200 nm $\times$200 nm. The STM constant current image shows the characteristic granular structure of Au. In the corresponding BEEM image, brighter areas indicate an enhanced electron transmission. As one can see, however, the features visible in the BEEM image correlate exclusively with the granular structure and the topographic features of the Au-film and can not be correlated to the organic film underneath.

To investigate the transmission behavior of TiOPc, we systematically measured ballistic electron spectra at various temperatures. To improve the signal to noise ratio, a large number of spectra are taken at different positions of the sample and finally averaged. All curves were normalized to the value of 1 (the BEEM current values are divided by the
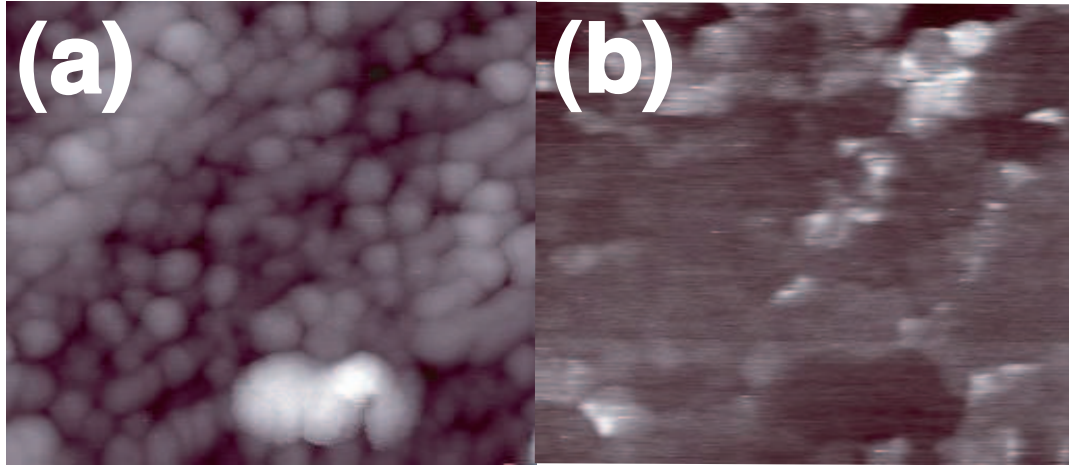
Figure 5.1: (a) STM topographic image of the Au/TiOPc/GaAs heterostructure. The image was recorded at $T = 300K$, $I_t = 5nA$, $V_t = 1.4V$. Scansize is 200nm x 200nm. (b) Corresponding BEEM image recorded simultaneously with the STM image. The color scale corresponds to $0 \ldots 1pA$.

maximum BEEM current value).

In Figure 5.2 (a) such averaged BEEM spectra are displayed for various temperatures. The shown curves are averaged of over 100 individually BEEM spectra. The tunneling current was $I_t = 20$ nA for T= 70, 100, 120, 170, 300 K and $I_t = 5$ nA for T=10, 50 K. for each temperature.

In BEEM measurements, the Schottky barrier height is defined by the onset of the collector current in the BEEM spectra. To extract this barrier height from the measured data, a quadratic power law fit was employed. (see [271]). The Bell-Kaiser model was not used because already the straightforward power law, despite of its simplicity, fits our data very well and turned out to be completely sufficient for our purposes.

$$I_{BEEM}(V_t) = \alpha(V_t - V_b)^2 \quad . \tag{5.1}$$

The fit-formula used to analyse the experimental data is shown in 5.1. α and V_b are fit-constants, V_b is the fitted onset.

Figure 5.2 (a) shows a set of spectra, which were recorded at different temperatures. First thing to be mentioned is: we find that the TiOPc increases BEEM threshold voltage compared to reference Au/GaAs diodes, which is also found in the literature [36, 39]. One

can clearly see that with decreasing temperature, the onset is significantly shifted to higher values. A detailed data analysis shows that the Schottky barrier increases from 1.2 eV at T= 300 K to a value of 1.5 eV at T= 10 K. In Figure 5.2 (b) the Schottky barrier heights are plotted versus temperature and show an approximately linear behavior.

Figure 7.1 shows a sketch of the experimental setup together with the conduction band profile of our sample. The higher valleys for GaAs (X- and L-valley) are also shown.

According to our measurements, the lowest unoccupied molecular orbital (LUMO) of TiOPc is 1.2 eV above the Fermi energy and the highest occupied molecular orbital (HOMO) of TiOPc is 0.6 eV according to the literature [49] below the Fermi energy of the sample.

Concerning the interface between TiOPc and GaAs, our experiments indicate that the LUMO-level of TiOPc is above the Γ-valley of GaAs and we therefore directly measure the Schottky barrier height of Au on TiOPc. Details are outlined below.

As final point in this work, we have to prove our assumption that the measured Schottky barrier height is in fact the barrier height between Au and TiOPc and not the height of the barrier between Au and GaAs. There are two arguments which support our assumption: First, the Schottky barrier height of 1.53 eV at a temperature of T= 10 K would exceed the band gap of GaAs, wich is 1.51 eV. This is extremely unlikely because due to the high surface state density on GaAs, the SBH is in the order of $E_g/2$ for all known metals. Further, a SBH above the energy gap of GaAs would also imply a hole inversion layer at the surface of the n-type GaAs sample, which again is extremely unlikely.

In addition to these arguments, we can find further features by analyzing the shape of the BEEM spectra, especially by plotting the numerically calculated first derivative of the BEEM spectra. As typical example, Figure 5.4 shows the averaged and normalized BEEM spectrum at 300 K (left axis) and its first derivative (right axis). The first derivative of the BEEM spectrum was calculated using the Savitzky Golay smoothing filter method [273].

As one can see, there are two another very distinct onsets in the first derivative of the spectrum and additional further spectral features at higher bias. The tunneling conditions in the current experiment, however, were not good enough for systematic measurements in the high bias regime.

As shown below, however, the two distinct onsets can be identified as signatures of the L- and X-valleys of GaAs. On conventional Au-GaAs diodes, the influence of higher valleys is normally seen as an increased slope in the first derivative of the spectrum, as the
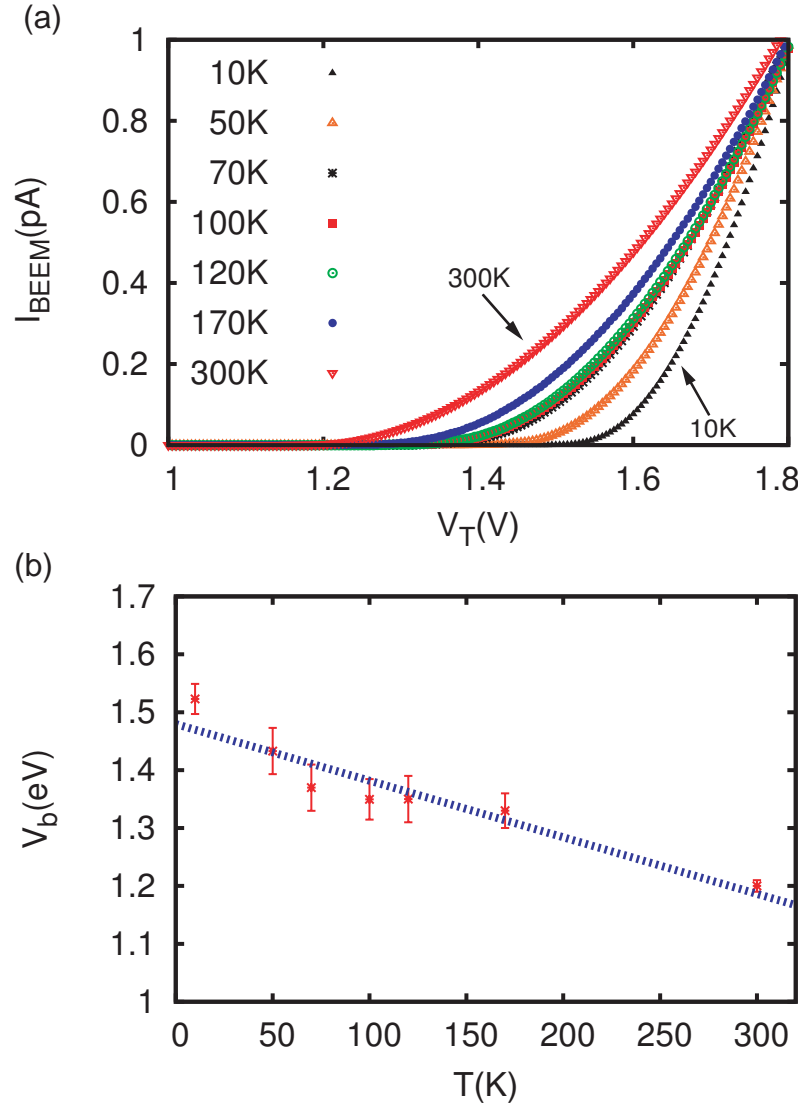
Figure 5.2: (a) averaged BEEM spectra for various different temperatures, between 300K and 10K. For better viewing, all curves were normalized to the value of 1 (the BEEM current values are divided by the maximum BEEM current value). (b) Temperature dependence of the measured SBH with error bars and a linear fit to the data.

Figure 5.3: (a) Schematical view of the experimental setup. (b) The conduction band profile of our sample (Γ-valley at 170K) and the higher X- and L-valleys in valleys for GaAs are also shown. E_f^{sample} is the Fermi energy of the sample, V_{STM} is the tunneling voltage and I_{BEEM} is the ballistic current.

higher valleys open additional transport channels into the collector electrode.

Most probably to an increased scattering in the base of our Au-TiOPc-GaAs samples compared to pure Au-GaAs diodes. Taking these higher onsets in the first derivative (see the marked positions in Figure 5.4) as energetic positions of the *L*- and *X*-valleys in GaAs, respectively, we measure an energy difference of 0.17 eV.

The theoretical value of the energy difference between the *L*- and *X*-valleys of GaAs can be canculated using

$$\Delta E_{\Gamma L}^{GaAs} = 0.296 - 6.45\ 10^{-5}\ \frac{T^2}{T + 204} \quad , \tag{5.2}$$

$$\Delta E_{\Gamma X}^{GaAs} = 0.462 + 8.05\ 10^{-5}\ \frac{T^2}{T + 204} \quad , \tag{5.3}$$

$$\Delta E_{XL}^{GaAs} = \Delta E_{\Gamma X}^{GaAs} - \Delta E_{\Gamma L}^{GaAs} \quad . \tag{5.4}$$

If we compare this experimental value with the calculated energy difference between the *L*- and *X*-valleys of GaAs using the above formulae found in [274] for 300 K, we get a value of 0.16 eV and therefore an excellent agreement with the literature values.

As the positions of the higher valleys in GaAs can now be used to calibrate the energy scale, we start from the *L*-valley and subtract the literature value of the energy difference between the Γ- and *L*-valley (0.295 eV at 300 K [274]) to determine the position of the Γ-valley. As result we obtain a value of 1.1 eV which is clearly smaller than the measured Schottky barrier height of 1.2 eV at 300 K. Hence we are sure that the measured Schottky barrier height really is the barrier height at the Au/TiOPc interface.

5.2   Summary

In summary, MBE grown Au-TiOPc-GaAs diodes were investigated by BEEM. Analyzing the BEEM spectra we find that the TiOPc layer increases the BEEM threshold voltage compared to reference Au/GaAs diodes, and that the measured SBH is the barrier height at the Au-TiOPc interface. Temperature studies show an increase of the SBH from 1.2 eV at room temperature to 1.5 eV at 10 K.
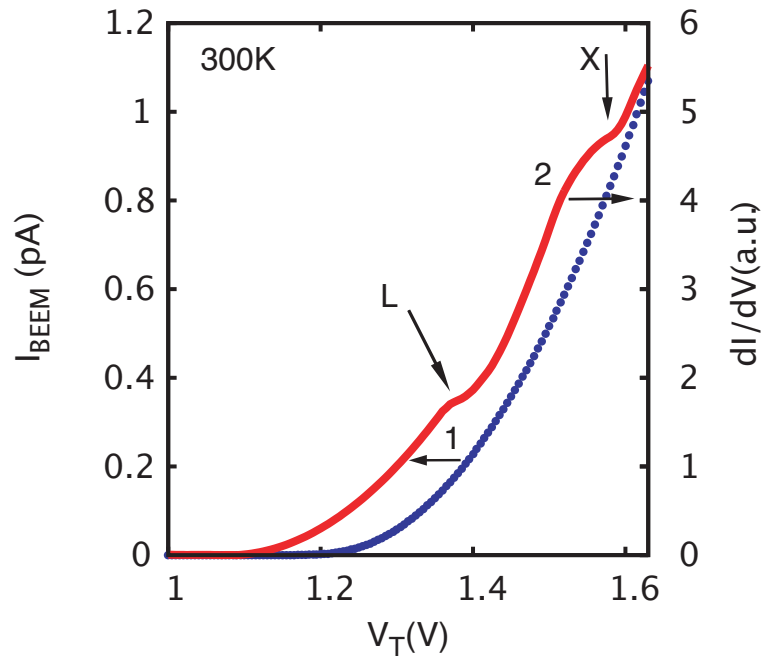
Figure 5.4: Averaged and normalized BEEM spectrum, curve 1 (the BEEM current values are divided by the maximum BEEM current value). The curve 2 is the first derivative, both curves for room temperature.

Chapter 6

Ballistic Electron Mean Free Path of Titanylphthalocyanine films grown on GaAs

In this chapter BEEM measurements were used to determine the transmission of ballistic electrons through TiOPc as a function of energy and temperature. Further the mean free path of the ballistic electrons through TiOPc is presented. The mean free path and the transmission through TiOPc is estimated using only one TiOPc film with a nominal thicknes of about 32 Åwith the help of Au/GaAs reference measurements. The thicknes of Au in Au/GaAs and Au/TiOPc/GaAs was the same, namely 7 nm.

6.1   Results and discussion

The conduction band profile of our experiment is shown in Figure 7.1 . If the bias between the tip and the Au-base layer is large enough, ballistic electrons coming from the STM tip into Au-base overcome the barrier at the Au/TiOPc interface and are collected in the semiconductor at a backside collector contact. The corresponding current I_c as a function of bias V_t called BEEM spectrum.

To investigate the transmission behavior of TiOPc, we systematically measured ballistic electron spectra at various temperatures. The temperature dependence of the Schottky barrier height in Au/TiOPc/GaAs is well described in [43] and in this article the transmission and the mean free path (mfp) is investigated as a function of temperature.
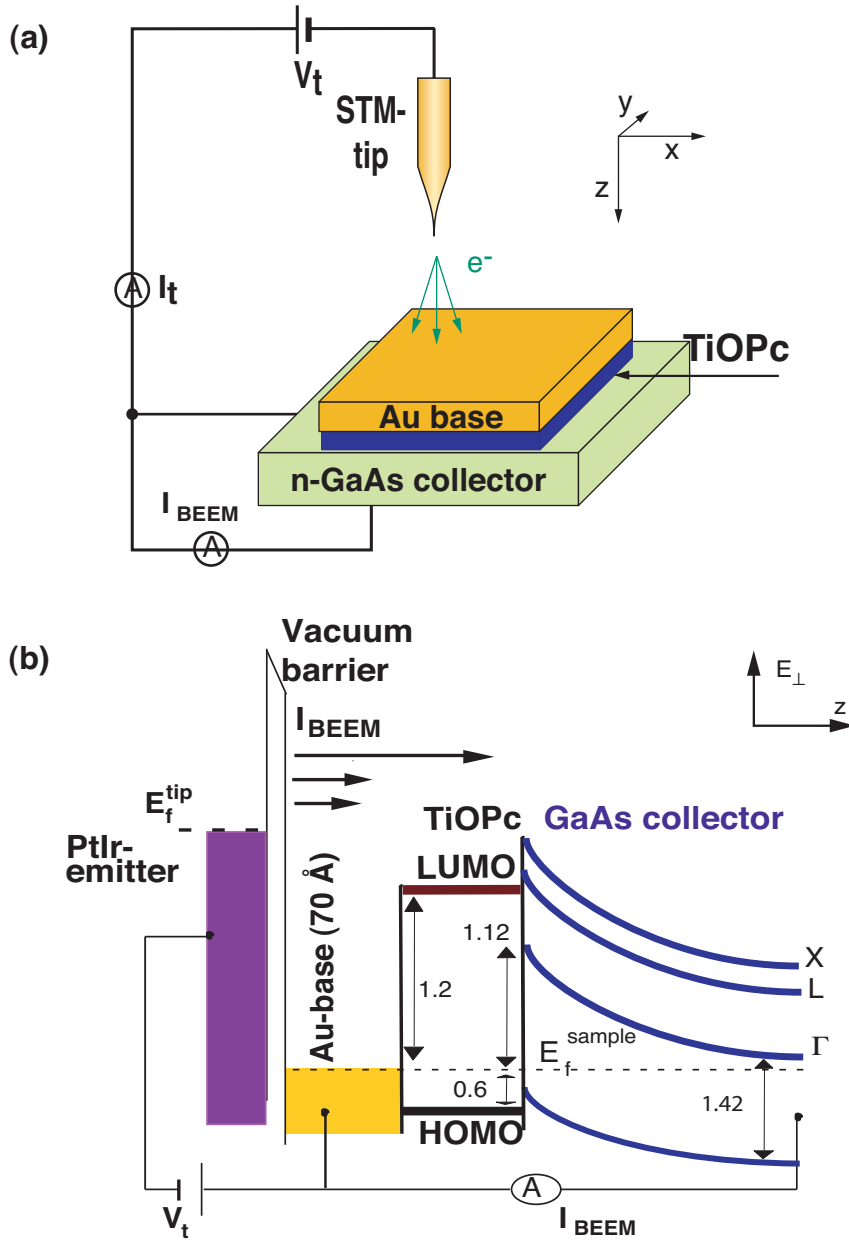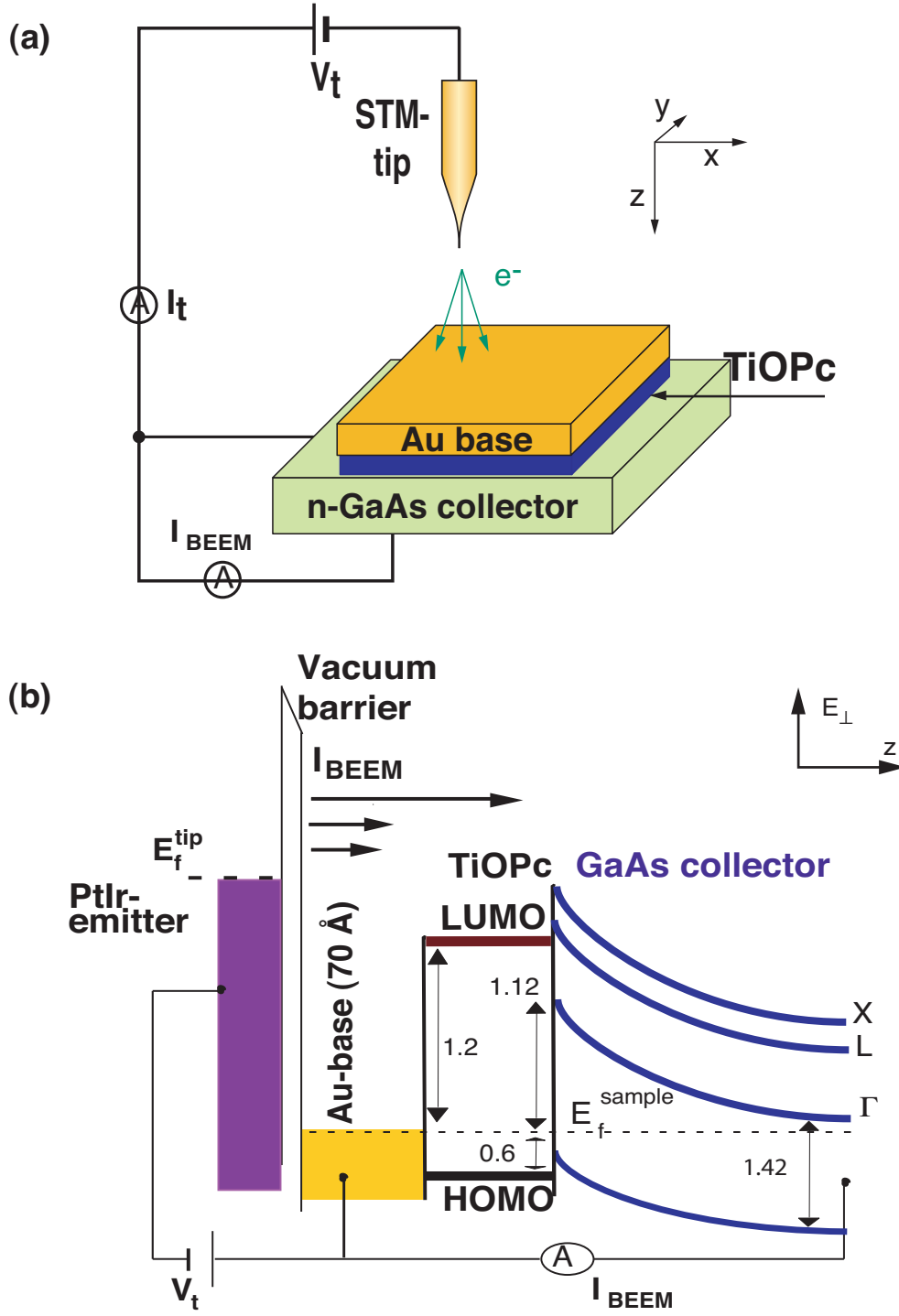
Figure 6.1: (a) Schematical view of the experimental setup. (b) The conduction band profile of our sample (Γ-valley at 300K) and the higher X- and L-valleys in valleys for GaAs are also shown. E_f^{sample} is the Fermi energy of the sample, V_{STM} is the tunneling voltage and I_{BEEM} is the ballistic current.
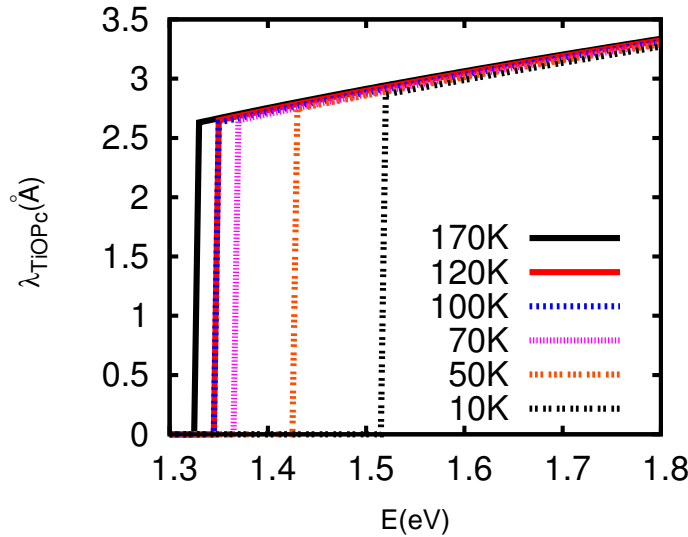
Figure 6.2: The energy dependent attenuation length of TiOPc for various temperatures, from 170K down to 10K. The shifting onset of the curves is due to the increasing Schottky barrier height with decreasing temperature. One can clearly see linear increase of the attenuation length with energy for all temperatures. The temperature dependence of attenuation length, however is rather weak.

Calculating the transmission we assumed that the BEEM current through Au/TiOPc/-GaAs is a energy dependent transmission factor times the BEEM current through Au/-GaAs, $I_{BEEM}^{TiOPc}(E) = T^{TiOPc}(E)I_{BEEM}^{GaAs}(E)$. With the help of reference measurements on Au/GaAs samples the transmission through TiOPc, can be obtained by division of these two spectra according to

$T^{TiOPc}(E) = I_{BEEM}^{TiOPc}(E)/I_{BEEM}^{GaAs}(E)$.

From these data, the attenuation length of the ballistic electrons, λ, can be determined. For this purpose, the ballistic electron current I_{BEEM} is expressed as $I_{BEEM} = I_t T(E)e^{-d/\lambda}$, where I_t is the tunneling current, $T(E)$ the energy dependent transmission through TiOPc obtained like described above and d the film thickness of TiOPc.

In Figure 6.2 is the energy dependent attenuation length of TiOPc shown. Two features are clearly visible: With the increase of the SBH with decreasing temperature [43] also the
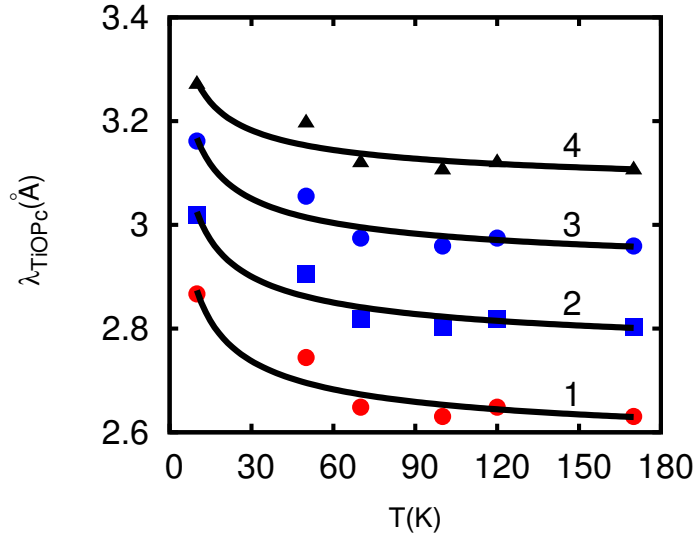
Figure 6.3: The attenuation length of TiOPc in dependence of the temperature taken at certain energies. Curve 1 shows values of the attenuation length taken at the SBH, Curve 2 shows values 100meV above the SBH, Curve 3 shows values 200meV above the SBH and Curve 4 shows values 300meV above the SBH. The solid line is a $aT^{-\frac{1}{2}} + b$ fit to the experimental data.

onset of the attenuation length is shifted to higher energies with decreasing temperatures In addition, one can also see a linear increase of the attenuation length with the energy for all temperatures. The temperature dependence of attenuation length, however, is rather weak.

To investigate the temperature dependence behaviour of the mfp, mfp-values taken at different energies, (at the SBH, 100meV, 200meV and 300meV above the SBH) were plotted as a function of temperature. The results of this procedure can be seen in Figure 6.3. As one can see, the mfp increases with decreasing temperature. Assuming phonon scattering to be responsible for this behavior, the solid lines are fits to the experimental values of the mfp, where the fitted curves follow a $aT^{-\frac{1}{2}} + b$ relation, which is the typical dependence for phonon scattering. Curve 1 is obtained for the mfp at the SBH, Curve 2, 3 and 4 are for 100, 200 and 300 meV above the SBH, respectively. As one can see, the
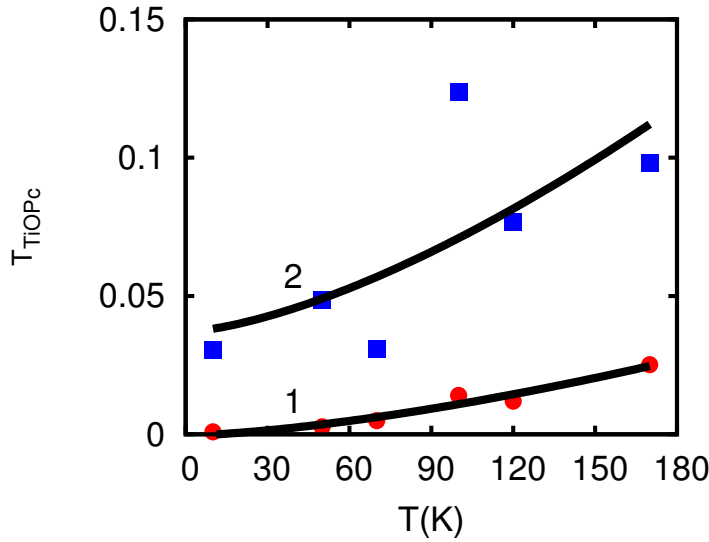
Figure 6.4: The transmission of TiOPc in dependence of the temperature, taken at different energies. Curve 1 shows values of the attenuation length taken at the SBH, Curve 2 shows values 100meV above the SBH,

curves fit the data reasonably well.

In addition to the mfp, we also investigated the energy dependent transmission of TiOPc as a function of temperature. In Figure 6.4, curve 1 shows transmission values taken at the SBH and curve 2 values 100 meV above the SBH, respectively. In contrast to the mfp, the transmission of TiOPc decreases with decreasing temperature, suggesting that for the transmission, ionized impurity scattering processes play a major role in this case.

For the fits to the data, a $aT^{\frac{3}{2}} + b$ power law behavior behavior was assumed. As one can see, this expression is in very good agreement with the data for the transmission values taken at the SBH. For the values taken 100 meV above the SBH the data show increased noise and larger deviations from the $aT^{\frac{3}{2}} + b$ behavior, which are getting larger for the transmission values taken 200 meV and 300 meV above the SBH. This, however, is not surprising in our opinion, since at higher energies a number of other scattering processes (avalange multiplication, Auger scattering etc.) may play an increasing role.

As shown above, the mfp and the transmission of TiOPc exhibit a different behavior as

a function of temperature. While the decreasing mfp with increasing temperature suggests, that the mfp is dominated by phonon scattering processes, the transmission seems to be dominated by impurity scattering and increases with increasing temperature, which seems to be an apparent contradiction.

Assuming a dominant ionized impurity interface scattering, however, either at the Au-TiOPc, TiOPc-GaAs or both interfaces, and in addition, only a moderate impurity scattering in the TiOPc bulk, can help to clarify the situation. In this case, ionized impurity scattering in the TiOPc bulk would only have a weak influence on the mfp and therefore the observed qualitative difference of the temperature behavior is consistently explained. On the other hand, however, this does not explain the surprisingly weak dependence of the mfp on the temperature, which is only in the order of 10 % in the investigated temperature regime. From this we conclude, that other scattering processes, which we cannot identify in the current experiment must also play a role and that the observed behavior is probably a superposition of all of them.

6.2   Summary

In summary, we have investigated the temperature and energy dependent electron transmission properties of TiOPc. It was found, that the transmission and the mfp both increase with energy, but exhibit a different behavior as a function of temperature. While the decreasing mfp with increasing temperature suggests, that the mfp is dominated by phonon scattering processes, the TiOPc transmission increases with increasing temperature, which suggests that the transmission is dominated by impurity scattering processes. Assuming dominant ionized impurity scattering at the interfaces, and dominant phonon scattering in the bulk, however, our findings can be consistently explained.

Chapter 7

Ballistic Electron Attenuation Length in Titanylphthalocyanine Films Grown on GaAs

In this chapter an experimental investigation of hot electron transport in thin TiOPc films grown on GaAs is presented. The transmisson through a Au/TiOPc/GaAs heterostructure is evaluated using the Bell-Kaiser model [3]. In addition, an approach to calculate the attenuation length in TiOPc is presented, whereas the method to calculate the attenuation length in TiOPc presented in this chapter is independent of the Bell-Kaiser model and independent of the method presented in chapter 6. Two Au/TiOPc/GaAs heterostructures, whereas the TiOPc-films had a nominal thickness of 10 and 6 monolayers, which correspond to about 3.2 and 1.9 nm, respectively. With a 7 nm thicknes of Au.

7.1 Results and Discussion

A schematic diagram of our experiment is shown in Figure 7.1. If the bias between the tip and the Au-base layer is large enough, ballistic electrons tunneling from the STM tip into Au-base can overcome the barrier at the Au/TiOPc interface and are collected in the semiconductor at a backside collector contact. The corresponding current I_{BEEM} as a function of bias V_t is called BEEM spectrum.

First measurements on the Au/TiOPc/GaAs heterostructure are published in [44] and the temperature dependence of the Schottky barrier height in Au/TiOPc/GaAs is already

described in [43]. In this article we focus on the transmission behavior of hot electrons through TiOPc and calculate the corresponding electron attenuation length.

In Figure 7.2 (a), a typical set of averaged BEEM spectra is shown. Figure 7.2 (a) shows the data for several TiOPc thicknesses (curve 1: 0nm TiOPc, curve 2: 1.9nm TiOPc, curve 31: 3.2nm TiOPc), embedded between a 7nm Au film and a GaAs bottom contact. From this point on we are using the following nomenclature for the samples: sample A (0 nm TiOPc), sample B (1.9 nm TiOPc) and sample C (3.2 nm TiOPc). One can clearly see the increase of the BEEM current threshold in the presence of TiOPc. With increasing thickness of TiOPc from 1.9 nm to 3.2 nm the onset of the ballistic current does not change, the current, however, is significantly decreased.

To analyze the data in more detail the Bell-Kaiser model [3] was used:

$$I_{BEEM}(V_t) = R\, I_{STM}\, \frac{\int_{E_z^{min}}^{\infty} dE_z\, T_{tb}(E_z) \int_0^{E_{xy}^{max}} dE_{xy}\, [f(E) - f(E + eV_t)]}{\int_0^{\infty} dE_z\, T_{tb}(E_z) \int_0^{\infty} dE_{xy}\, [f(E) - f(E + eV_t)]}\, , \qquad (7.1)$$

where the above formula is known as the Bell-Kaiser formula. I_{STM} is the constant tunnel current at which the ballistic spectrum is measured, R is a measure of attenuation due to scattering in the Au layer, and T_{tb} is the transmission coefficient of the vacuum barrier which is calculated by a transfer matrix method [91, 92]. The SBH V_b appears in the coefficients $E_z^{min} = E_f - eV_t + eV_b$ and $E_{xy}^{max} = E_z - E_f + eV_t - eV_b$. The prefactor R and V_b are fitting parameters. The Bell-Kaiser formula is well suited for fitting ballistic electron spectra on simple Schottky diodes in a voltage range of up to $\approx$ 200meV above the onset. Formula 7.1 describes our sample A very well as one can see in Figure 7.2 (a). The calculated BEEM-current yields a SBH at the Au-GaAs interface of $V_b = 0.89$ eV, which is in very good agreement with the values from the literature [26, 65].

For the samples B and C we use a extension of the above formula which is a modification of the original Bell-Kaiser model and consists of an additional transmission coefficient T_{hs} to describes the properties of the heterostructure [63]:

$$I_{BEEM}(V_t) = R\, I_{STM} \frac{\int_{E_z^{min}}^{\infty} dE_z\, T_{tb}(E_z) \int_0^{\infty} dE_{xy}\, T_{hs}(E_z, E_{xy})\, [f(E) - f(E + eV_t)]}{\int_0^{\infty} dE_z\, T_{tb}(E_z) \int_0^{\infty} dE_{xy}\, [f(E) - f(E + eV_t)]}\, . \qquad (7.2)$$

In this expression E_{xy}^{max} no longer has to be declared explicitly, because the limit is now implicitly included via the dependence of T_{hs} on E_{xy}. To avoid quantum interferences

between the vacuum barrier and the collector barrier, the transmission coefficients T_{tb} and T_{hs} are not combined into an overall transmission coefficient. To calculate T_{hs} we used the transfer matrix method using a potential shown in Figure 7.2 (b). The TiOPc layer is modelled via a rectangular barrier with the height of the measured Schottky barrier and the width of the samples B and C. In Figure 7.2 (a) the calculations for the samples B and C are shown where the extended Bell-Kaiser model equation 7.2 was used. Here, the calculation yields the same SBH for the samples B and C, $V_b = 1.2$ eV, respectively, for the Au-TiOPc interface. As one can see in Figure 7.2 (a) for both samples with TiOPc the extended Bell-Kaiser model does not describe the BEEM-current for higher energies extremely well for two major reasons: first the influence of the GaAs L and X valleys was not included in the calculations, and second the assumption of modelling the TiOPc with a simple rectangular potential barrier is not precise enough.

Now we want evaluate the attenuation length through TiOPc as a function of the energy. Since the Bell-Kaiser model does not describe the BEEM current through the samples B and C sufficiently at high energies we use a different approach. First, we write the BEEM current through the Au/TiOPc/GaAs heterostructure as:

$$I_{BEEM}(d_{TiOPc}) = I_{STM}\, t_{tot} = I_{STM}\, t_{Au}\, t_{TiOPc}(d_{TiOPc}), \tag{7.3}$$

which is the BEEM current through the whole structure. I_{STM} is the constant tunnel current at which the ballistic spectrum is measured, t_{tot} is a measure of attenuation through the whole structure and can be written as a product of the attenuation through the base layer and the attenuation through TiOPc. In the above formula 7.3 the product $I_{STM}t_{Au}$ stays constant, because I_{STM} is constant anyway and t_{Au} can be treated as energy independent, therefore and we can write:

$$\frac{I_{BEEM}(d_{TiOPc})}{t_{TiOPc}(d_{TiOPc})} = I_{STM}\, t_{Au} = const. \tag{7.4}$$

now we put BEEM currents for two different thicknesses of TiOPc in equation 7.4 and get:

$$\frac{I_{BEEM}(d_{TiOPc}^{(1)})}{I_{BEEM}(d_{TiOPc}^{(2)})} = \frac{t_{TiOPc}(d_{TiOPc}^{(2)})}{t_{TiOPc}(d_{TiOPc}^{(2)})}. \tag{7.5}$$

by writing $t_{TiOPc}(d_{TiOPc}) \propto \exp(-d_{TiOPc}/\lambda_{TiOPc})$

$$\ln\left(\frac{I_{BEEM}(d_{TiOPc}^{(1)}, E)}{I_{BEEM}(d_{TiOPc}^{(2)}, E)}\right) = \ln\left(t_{TiOPc}(d_{TiOPc}^{(1)})\right) - \ln\left(t_{TiOPc}(d_{TiOPc}^{(2)})\right)$$

$$= \frac{d_{TiOPc}^{(1)}}{\lambda_{TiOPc}} + \frac{d_{TiOPc}^{(2)}}{\lambda_{TiOPc}} = \frac{1}{\lambda_{TiOPc}}\left(d_{TiOPc}^{(2)} - d_{TiOPc}^{(1)}\right), \qquad (7.6)$$

we finally get equation 7.6, from which we obtain an expression for the attenuation length, $\lambda_{TiOPc}(E)$, in dependence of the energy:

$$\lambda_{TiOPc} = \frac{d_{TiOPc}^{(2)} - d_{TiOPc}^{(1)}}{\ln\left(\frac{I_{BEEM}(d_{TiOPc}^{(1)}, E)}{I_{BEEM}(d_{TiOPc}^{(2)}, E)}\right)}. \qquad (7.7)$$

With formula 7.7 one can plot $\lambda_{TiOPc}(E)$ from the logarithmized measured values. We note that our evaluation of $\lambda_{TiOPc}(E)$ is independent of the use of the Bell-Kaiser model. In Figure 7.3 we see the outcome of such a calculation for $\lambda_{TiOPc}(E)$, where the BEEM currents of sample B and C were used. The attenuation length is increasing at the Schottky barrier height to about 4 Å and saturates at this value at about 1.25 eV.

7.2 Summary

In summary, we have investigated electron transmission properties of TiOPc. It was found that the ballistic current through Au/TiOPc/GaAs heterostructure can not be described precisely with the heterostructure extension of the Bell-Kaiser model at higher energies. This is because of two reasons: First, we did not include the influence of the GaAs L and X valleys into the calculations, and modelling the TiOPc with a simple rectangular potential barrier is not accurately enough. Additionally, an approach for the determination of the attenuation length of TiOPc as a function of energy has been successfully introduced.
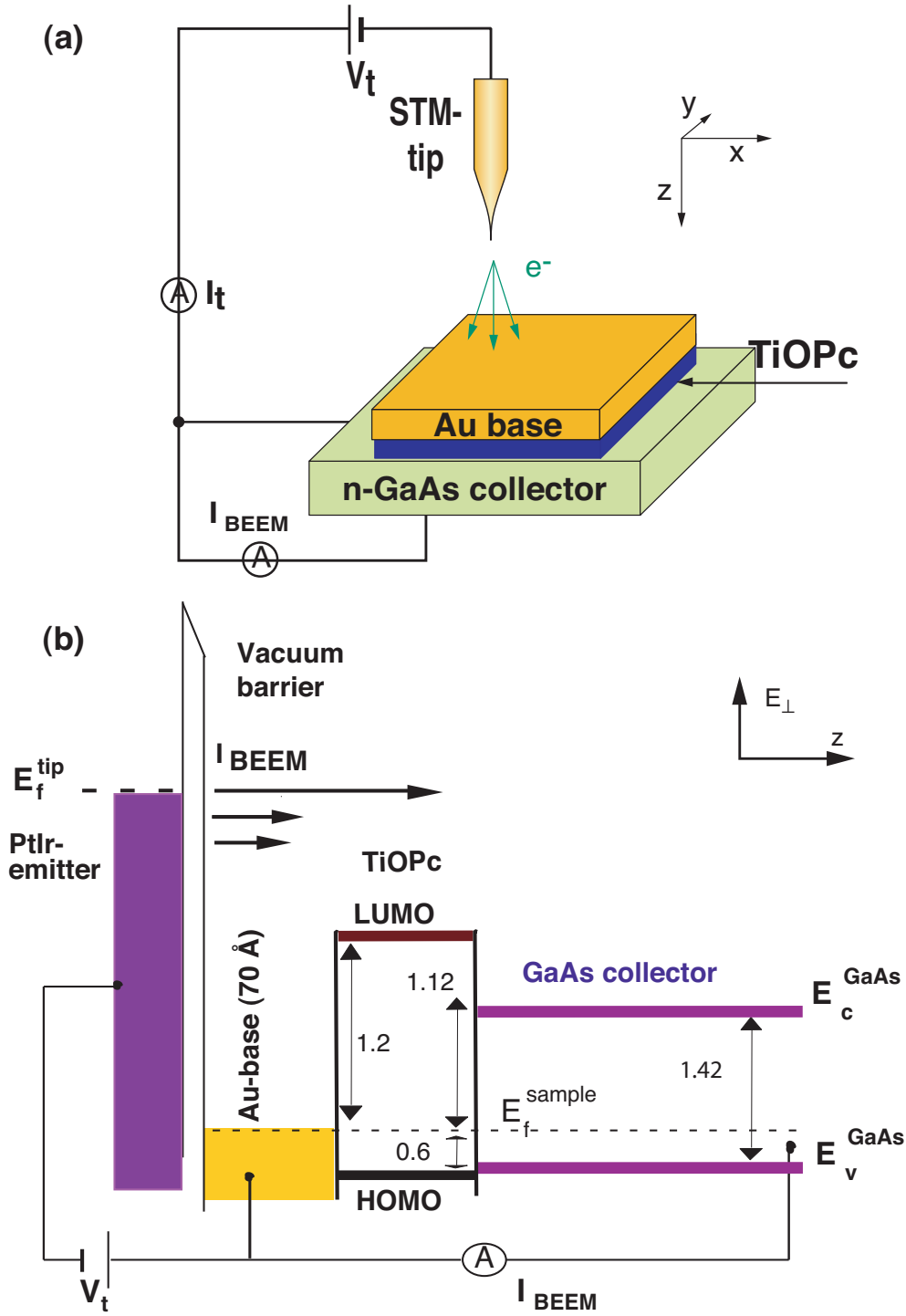
Figure 7.1: (a) Schematical view of the experimental setup. (b) Band profile of our experiment. E_f^{sample} is the Fermi energy of the sample, V_t is the tunneling voltage and I_{BEEM} is the ballistic current.
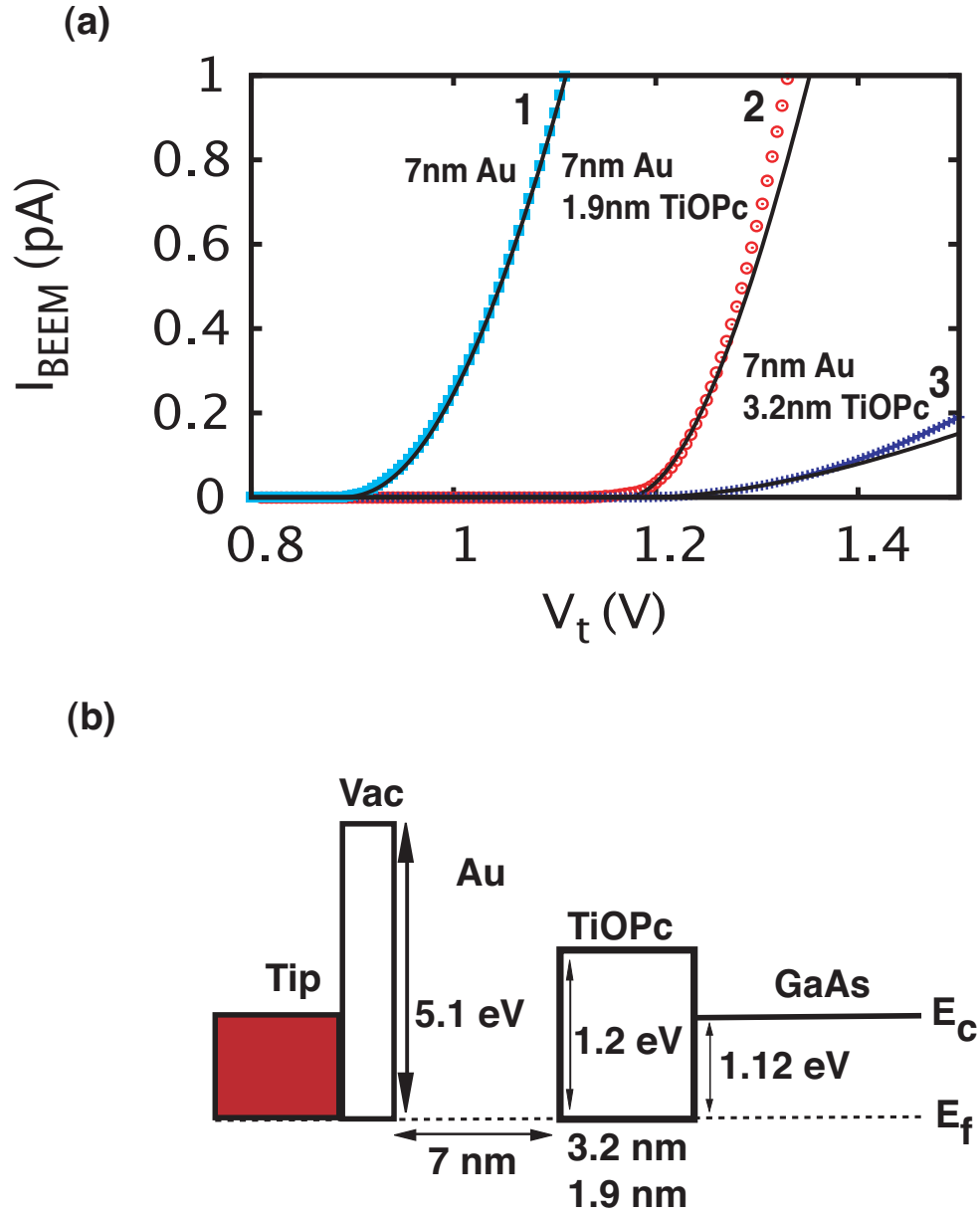
Figure 7.2: (a): Averaged BEEM spectra of Au/GaAs and Au/TiOPc/GaAs at 300 K. Curve (1): Averaged BEEM spectrum of 7 nm Au/GaAs. Curve (2): 7 nm Au/3.2 nm TiOPc/GaAs. Curve (3): 7 nm Au/1.9 nm TiOPc/GaAs. Solid lines are the calculated spectra. Curve (1) was calculated using the conventional Bell-Kaiser model, curve (2) and (3) are calculations for the situation depicted in (b), which were carried out applying the heterostructure extension of the Bell-Kaiser model.
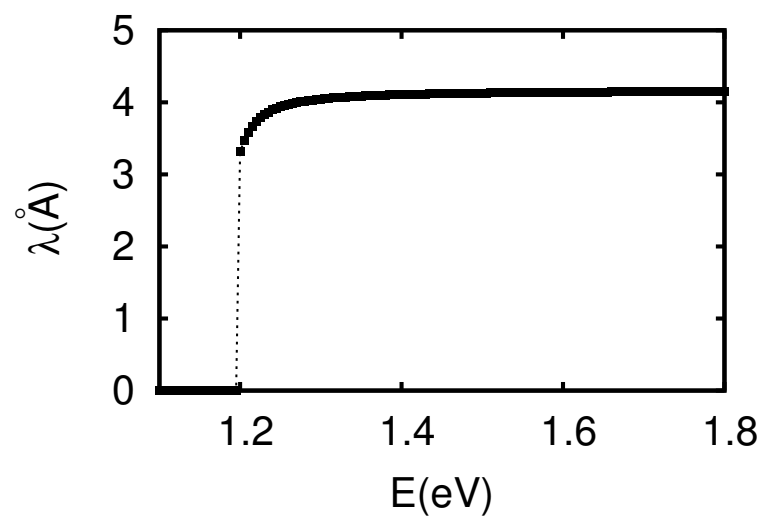
Figure 7.3: Ballistic electron attenuation length of TiOPc versus electron energy. The plot was generated from the BEEM current spectra of samples B and C, see text

Chapter 8

Temperature Dependent Schottky Barrier Height and Fermi Level Pinning on Au/HBC/GaAs Diodes

Au/ HBC (hexa-*peri* hexabenzocoronene, $C_{42}H_{18}$) /GaAs heterostructures were investigated by BEEM. At room temperature, the Schottky barrier height at the Au/HBC interface was measured to be 1.3 eV, while the Fermi level at the HBC-GaAs interface is pinned 1.2 eV below the GaAs conduction band. Decreasing the temperature down to $T = 10$ K, the Au/HBC Schottky barrier height increases up to 1.55 eV and the Fermi level pinning at the HBC-GaAs interface reaches a value of 1.4 eV, close to the valence band of GaAs. These high values make HBC a promising interfacial layer in order to increase the open circuit voltage of GaAs Schottky barrier solar cells, e.g.

8.1 Introduction

During the last years, much interest has been focused on thin organic films due to their potential applicability for electronic and optoelectronic devices such as organic light-emitting diodes (OLEDs) [94, 275, 276], optical detectors, waveguides, thin insulators, sensors, organic field effect transistors [277, 278], and photovoltaic devices [269, 279, 280]. Organic thin films are nowadays already widely used in various electronic devices, such as organic solar cells, OLEDs, xerography, plate making printings and laser printers. Therefore the knowledge and understanding of the metal-organic interface plays a significant role in the
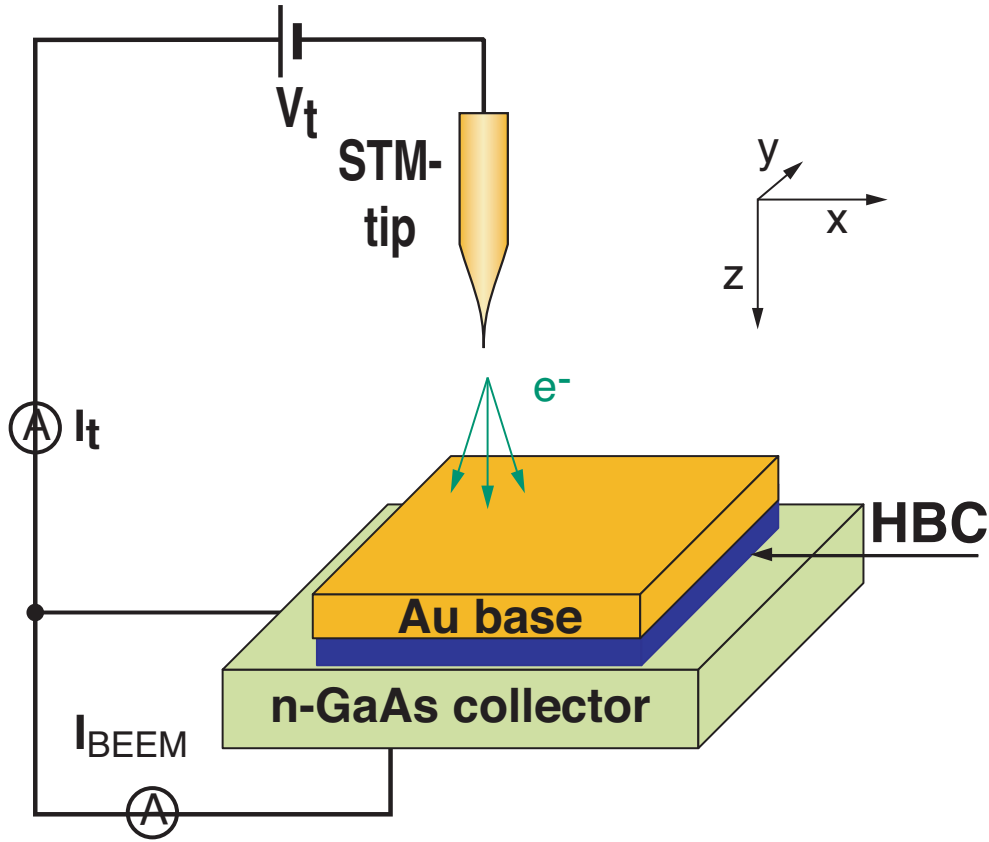
Figure 8.1: Schematical view of the experimental setup.

further development and improvement of organic and molecular electronics.

With the increasing interest in organic semiconductors, BEEM was also used to study metal-organic interfaces [36, 39, 41, 43], and especially large flat hydrocarbons like hexa-*peri* hexabenzocoronene ($C_{42}H_{18}$, HBC, structural formula shown in Fig. 8.2 (a)) are useful as relatively simple model compounds which have interesting electronic properties [253].

8.2   Experimental

For our experiment, we used low doped ($N_D \approx 1 \times 10^{16}$ cm^{-3}) GaAs substrates purchased at Wafer Technology LTD, UK. On these substrates, HBC-films having a nominal thickness of about 4 monolayers, which corresponds to about 12 Å, were grown using organic MBE [230]. For the base layer, we evaporated a 70 Å thick Au film onto the sample via a shadow mask prior to the BEEM measurements. The BEEM measurements were carried out in

Helium exchange gas in the variable temperature inset of a cryostat. The temperature in our experiment ranged from 10 K to 300 K.

8.3   Results and Discussion

To investigate the highest occupied molecular orbital (HOMO) / and the lowest unoccupied molecular orbital (LUMO) energy positions with respect to the GaAs conduction bands at the Au/HBC and HBC/GaAs interfaces, ballistic electron spectra were measured systematically at different temperatures. In order to improve the signal-to-noise ratio, over 100 individual spectra were acquired and averaged at different locations on the sample surface. The SBH is then defined by the onset of the collector current in the BEEM spectra. To extract the barrier height from the measured data in a reproducible way, a quadratic power law fit was employed (see Ref. [271]). We will show below that the barrier extracted from the BEEM spectra corresponds to the SBH at the Au/HBC interface. We will also show that the Fermi level pinning at the HBC/GaAs interface causes the position of the Γ-valley in the GaAs conduction band to be significantly lower than the SBH at the Au/HBC interface.

A typical averaged BEEM spectrum measured at room temperature can be seen in Figure 8.3 (left axis) together with its first derivative (right axis). Two main features are evident in the spectra: First, the organic layer increases the BEEM threshold voltage compared to reference Au/GaAs diodes, where a typical onset bias of 0.9 eV is found. Second, the Fermi level pinning at the HBC-GaAs interface is much closer to the valence band than on Au/GaAs diodes, leading to an unusually large difference between the Fermi energy and the Γ- valley of GaAs of 1.2 eV at the HBC/GaAs interface.

To obtain this result, we only have to identify the signatures of the L and X valleys of GaAs in the BEEM spectra and use them as reference points on the energy scale, as we already did it in our previous work on Au/TiOPc/GaAs samples [43]. According to the literature on conventional Au/GaAs diodes, [6] the signatures of the L and X valleys of GaAs are visible as additional features in the derivatives of the BEEM spectra, as regions with increased slope [6, 43]. In our data (see Figure 8.3 (right axis), one can also identify the signatures of the L and X valleys as two additional onsets in the first derivative of the BEEM spectra, but in contrast to Au/GaAs diodes, these features are observed at higher bias.

As the energetic differences between the Γ-, $L-$ and X valleys of GaAs are known, the position of the Γ- valley can now be determined. In our case, we get a value of 1.2 eV ($T = 300$ K) for the position of the GaAs Γ-valley above the Fermi energy at the HBC/GaAs interface, which is a very high value compared to the SBH of Au-GaAs diodes ($V_b \sim 0.9$ eV) without an organic interfacial layer.

We now want to discuss the alignment of the HOMO and the LUMO with respect to the Fermi energy and the GaAs conduction band. Values for the bandgap of HBC can be found in the literature [254, 255]. In Ref.[254] a transport gap of $E_g^{elec}(HBC) \sim 3.2$ eV, an optical transport gap of $E_g^{opt}(HBC) \sim 2.8$ eV, and an ionization energy of $I = 5.9$ eV is reported. In Ref. [255] a value of $E_g^{opt}(HBC) \sim 2.7$ eV for the optical gap, an exciton binding energy of 0.5 eV and a surface dipole of $\Delta \sim -0.8$ eV can be found.

Note that the situation in Refs. [254, 255] is quite different to ours. In Refs.[254, 255] HBC on Au is considered, but in our case we have polycrystalline Au evaporated on HBC and thus, there is a difference between organic/metal and metal/organic interfaces [281]. Metals on organic substrates are much more complex than the organic films on metal substrates because chemical reactions and metal diffusion can readily occur [282, 283].

However, if we take the literature value of ~ 3 eV for the transport gap, the value of -0.8 eV for the interface dipole layer, and 5.1 eV for the workfunction of polycrystalline Au, we obtain a conduction band diagram as shown in Figure 8.2 (b), which turns out to be consitstent with our experimental data. An interface dipole at the HBC-GaAs interface was neglected. By applying the Schottky-Mott rule for metal-semiconductor interfaces one gets $\phi_B^p = I - \phi_m - \Delta = 1.6$ eV for the hole injection barrier, and the electron injection barrier is calculated as $\phi_B^n = E_g - \phi_B^p = 1.4$ eV. This value is 0.1 eV higher then the measured SBH of 1.3 eV, we assume that is most likely due to breakdown of the Schottky Mott rule for metal-organic interfaces [284, 285].

To study the temperature dependence of the SBH and the Fermi level pinning at the HBC/GaAs interface, systematic BEEM measurements were carried out in the whole temperature range from $T = 300$ K down to $T = 10$ K.

The results for the SBH at the Au/HBC interface are plotted in Figure 8.4 (a), and the energy difference between the Fermi level and the GaAs Γ-valley at the HBC/GaAs interface can be seen in Figure 8.4 (b). For reference purposes, the corresponding SBH for a Au/TiOPc interface [43] is also plotted in Figure 8.4 (a). As one can see, the SBH at the Au/HBC interface increases approximately llinearly from 1.3 eV at $T = 300$ K to 1.56

eV at $T = 10$ K. The Fermi level pinning, which means the energy difference between the Fermi level and the GaAs Γ-valley, follows this trend and increases from 1.2 eV at $T = 300$ K to 1.4 eV at $T = 10$ K, which is already close to the valence band of GaAs.

While the increasing SBH with decreasing temperature is not surprising, the high barrier at the HBC-GaAs interface is indeed. Compared to Au-GaAs Schottky diodes ($V_b = 0.9$ eV), the barrier height at the HBC/GaAs interface is larger by 30% at room temperature. At $T = 10$ K, ($V_b = 1.0$ eV) the difference is even larger and and the inrease amounts to a value of 40%. Although the mechanisms responsible for this behavior are completely unclear to us at the moment, our finding has an interesting application: On Schottky contact solar cells, the open circuit voltage V_{oc} is mainly determined by the SBH, and it is known from Si-solar cells [286] that V_{oc} can be increased by additional interfacial layers. While in Si-solar cells, however, the increased V_{oc} is a consequence of the complex electrostatic situation in the metal-insulator-semiconductor system under illumination, HBC seems to change the Fermi level pinning directly. Thus, we expect that HBC interfacial layers increase the open circuit voltage V_{oc} of Schottky barrier solar cells significantly and in a more efficient way.

8.4   Summary

In summary, the Schottky barrier heights of Au/HBC/GaAs heterostructures were investigated by BEEM. Between $T = 300$ K and $T = 10$ K, the Schottky barrier height at the Au/HBC interface increases from 1.3 eV at $T = 300$ K to 1.56 eV at $T = 10$ K. Simultaneously, the Fermi level pinning at the HBC/GaAs interface becomes systematically deeper, starting with a position of 1.2 eV belov the GaAs conduction band at $T = 300$ K and ending at 1.4 eV at $T = 10$ K, which is close to the valence band of GaAs. The high barrier at the HBC-GaAs interface makes this material a promising interfacial layer for increasing the open circuit voltage of GaAs Schottky barrier solar cells.
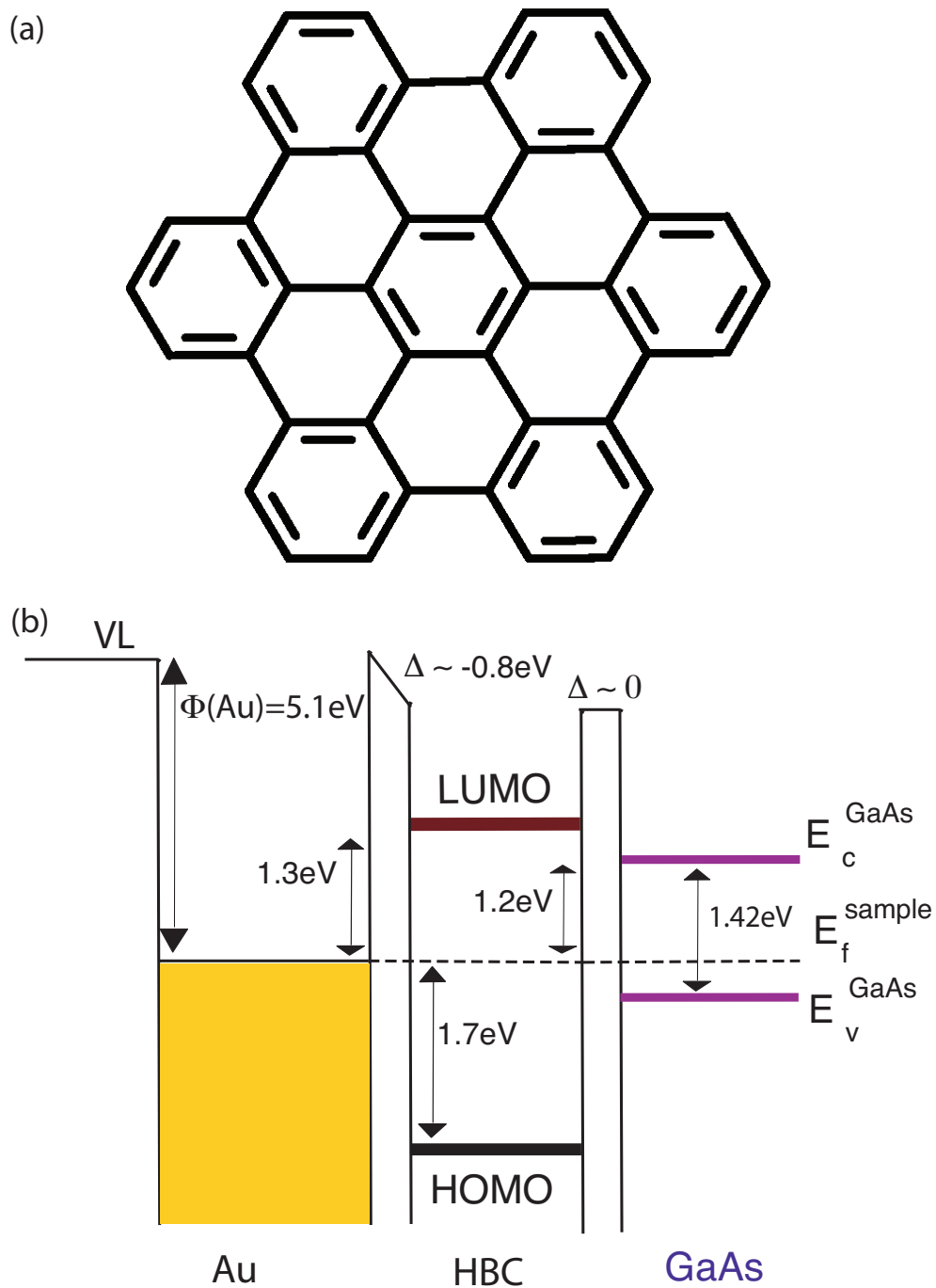
Figure 8.2: (a) Structural formula of hexa-*peri* hexabenzocoronene ($C_{42}H_{18}$, HBC). (b)Band diagram of our sample. E_f^{sample} is the Fermi energy, E_v^{GaAs}, and E_c^{GaAs} is the valence and conduction band of GaAs respectively.
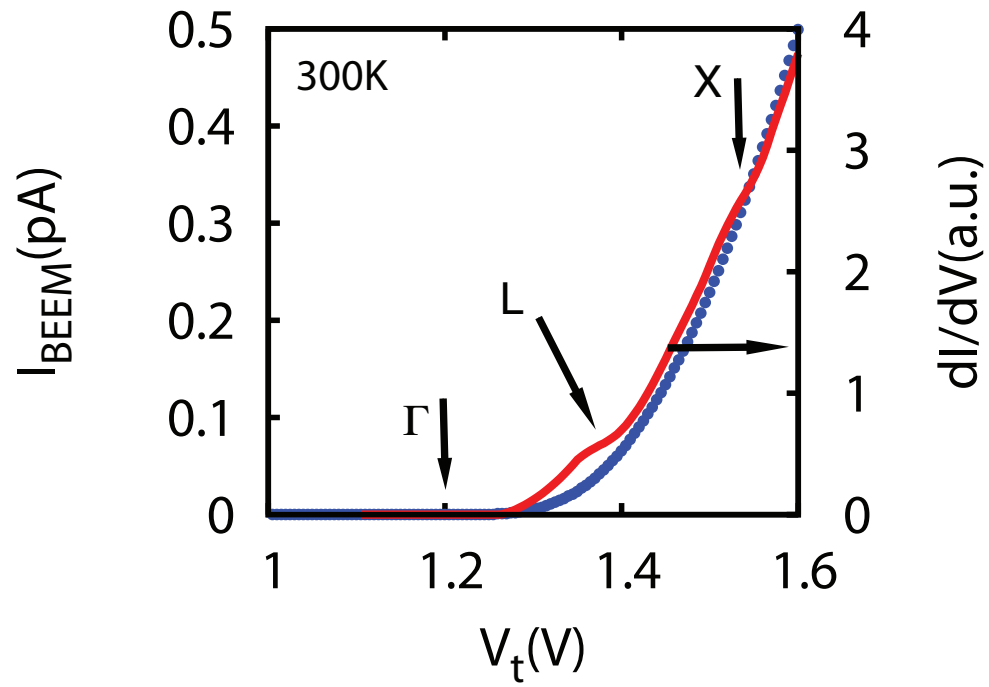
Figure 8.3: Averaged BEEM spectrum (left axis) and its first derivative (right axis). Both curves represent room temperature data.
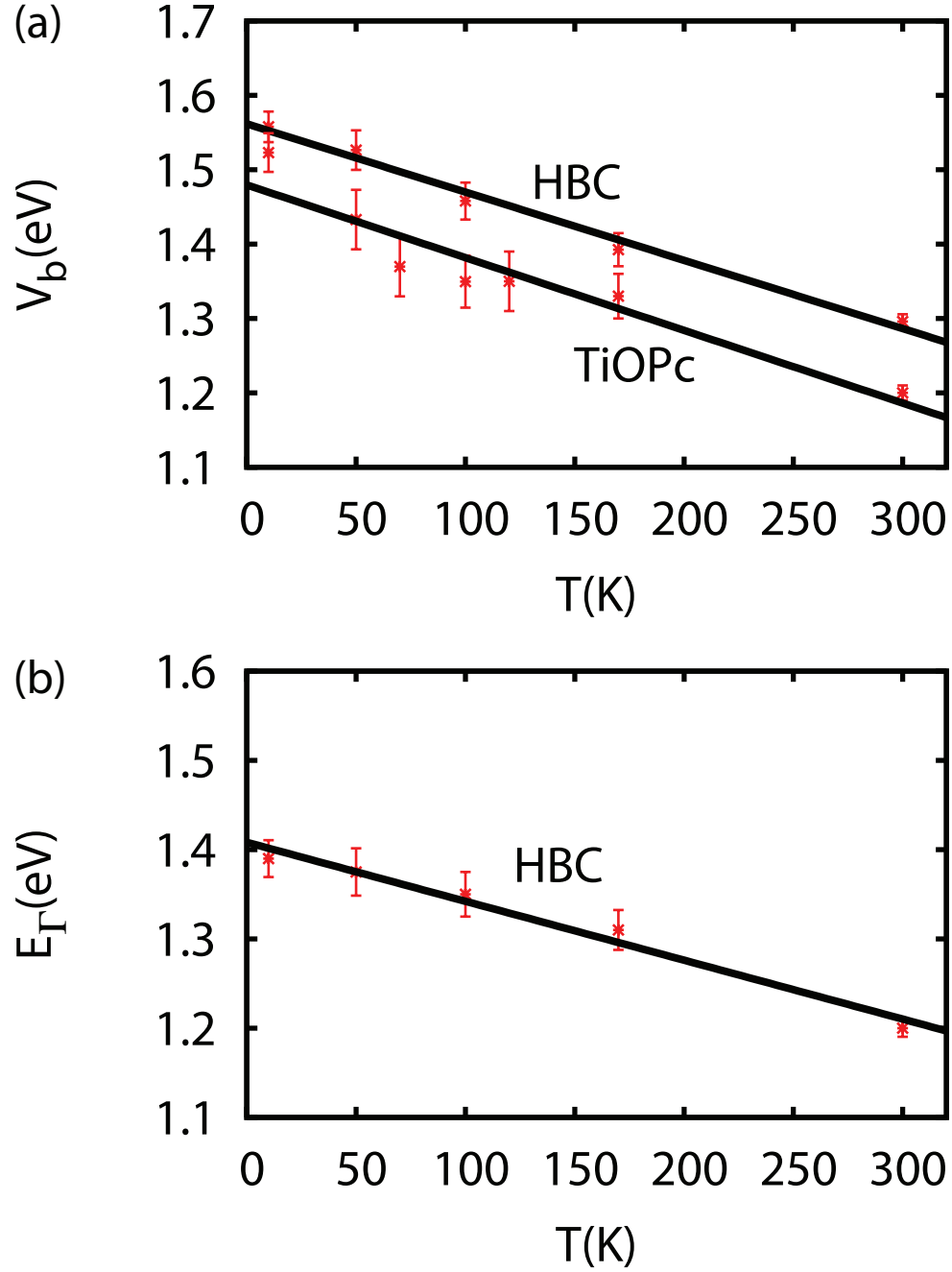
Figure 8.4: (a) SBH versus temperature for the Au/HBC and Au/TiOPc interface. The TiOPc data were taken from Ref. [43]). The solid lines are linear fits to the data. (b) Energy difference between the Fermi level and the GaAs (E_Γ) valley as a function of temperature.

Chapter 9

Summary and Outlook

9.1   Summary

Due to the BEEM images, it can be concluded that the samples are very homogeneous, in comparison to organic films manufactured by evaporation. All features visible in the BEEM images of our samples correlate exclusively with the granular structure and the topographic features of the Au-film and cannot be correlated to the organic film underneath. Analyzing the BEEM spectra we find that the TiOPc increases the BEEM threshold voltage compared to reference Au/GaAs diodes, which was also found in [39], where a BEEM study on a Au/Molecule/n-GaAs diode was done. The barrier height measured on the Au-TiOPc-GaAs is $V_b \approx 1.2\text{eV}$, which is in good agreement with the data found in references [49]. The results indicate that TiOPc functions as a p-type semiconductor, which is plausible since the measurements were carried out in air [230]. In addition, the derivative of the BEEM spectra shows multiple features in the energy regime above the LUMO level [230]. Possible origins of these features are currently under investigation.

In chapter 5, MBE grown Au-TiOPc-GaAs diodes were investigated by BEEM. Analyzing the BEEM spectra we find that the measured SBH is the barrier height at the Au-TiOPc interface. Temperature studies show an increase of the SBH from 1.2 eV at room temperature to 1.5eV at 10K.

In chapter 6, we have investigated the temperature and energy dependent electron transmission properties of TiOPc. It was found, that the transmission and the mfp both increase with energy, but exhibit a different behavior as a function of temperature. While the decreasing mfp with increasing temperature suggests, that the mfp is dominated by

phonon scattering processes, the TiOPc transmission increases with increasing temperature, which suggests that the transmission is dominated by impurity scattering processes. Assuming dominant ionized impurity scattering at the interfaces, and dominant phonon scattering in the bulk, however, our findings can be consistently explained.

In chapter 7, we have investigated electron transmission properties of TiOPc. It was found that the ballistic current through Au/TiOPc/GaAs heterostructure can not be described precisely with the heterostructure extension of the Bell-Kaiser model at higher energies. This is because of two reasons: First, we did not include the influence of the GaAs L and X valleys into the calculations, and modelling the TiOPc with a simple rectangular potential barrier is not accurately enough. Additionally, an approach for the determination of the attenuation length of TiOPc as a function of energy has been successfully introduced.

In chapter 8, the Schottky barrier heights of Au/ HBC(hexa-*peri* hexabenzocoronene, $C_{42}H_{18}$) /GaAs heterostructures were investigated by BEEM. Between $T = 300$ K and $T = 10$ K, the Schottky barrier height at the Au/HBC interface increases from 1.3 eV at $T = 300$ K to 1.56 eV at $T = 10$ K. Simultaneously, the Fermi level pinning at the HBC/GaAs interface becomes systematically deeper, starting with a position of $1.2eV$ above the GaAs conduction band at $T = 300$ K and ending at 1.4 eV at $T = 10$ K, which is close to the valence band of GaAs. The high barrier at the HBC-GaAs interface makes this material a promising interfacial layer for increasing the open circuit voltage of GaAs Schottky barrier solar cells.

9.2 Outlook

As organic MBE [230] growth nowadays allows the fabrication of many different types of hereterostructures. As few examples, we only mention Au/TiOPc/HBC/n-GaAs, Au/ TiOPc/3,4,9,10-perylenetetracarboxylic-3,4,9,10- dianhydride (PTCDA)/n-GaAs, Au/PTCDA/- HBC/n-GaAs among many others. As all these materials and heterostructures have applications as OLEDS or solar cells, electron transport through metal-organic, organic-organic, and organic-semiconductor interfaces is very important, especially if it can be studied on the nanoscale like in BEEM. The most relevant parameter for every heterostructure is the relative energetic alignment of the energy levels in the respective materials. Presently, the relative band alignment in organic hetererostructures is only known from measurements on macroscopic samples, however, no microscopic studies can be found in the present liter-

ature. Ballistic Electron Emission Microscopy is perfectly suited to determine sub-surface barrier heights and band offsets, as it was already demonstrated on the GaAs-AlGaAs system. Thus, measuring the relative positions of the LUMO levels on a PTCA-HBC heterostructure is a straightforward task, which can be extended to any material combination available. Investigating resonant tunneling structures on organic materials is a logical step forward. A proof of concept for resonant tunneling in organic resonant tunneling diodes and superlattices can be found in the literature but no local studies are reported until now. Here we have the possibility to study resonant tunneling processes and superlattice transport by BEEM, but also by other local probe techniques like conducting AFM measurements e.g.. As main advantage on organic semiconductors, however, scanning probe techniqies like BEEM or coducting AFM measurements can be used to study the efficiency of electron injection process for organic light emitting diodes (OLEDs). As the quantum efficiency for electroluminescence in organic semiconductors is close to unity, both BEEM and conducting AFM measurements can be carried out in emission mode simply by adding a photomultiplier and a spectrometer to the experiment. Also organic resonant tunneling structures are interesting to be tested with respect to their emission capabilities, since the involved processes leading to luminance are obviously not yet understood. Traps in heterostructures can also be studied by BEEM or scanning capacitance microscopy e.g.. BEEM allows a direct imaging of impurities as well as spectroscopic studies. Scanning capacitance microscopy allows imaging, too, and frequency dependent measurements can be utilized to study the dynamic behavior of traps in organic materials. Finally, BEEM/S experiments could be carried out on metal-organic-semiconductor heterostructures in an magnetic field perpendicular to the current direction. Such experiments could be performed to get information about the magnetic properties of organic semiconductors.

From the examples above, one can see that there are many open questions and the possible combinations for organic materials are almost unlimited. As BEEM experiments are relatively easy to perform, we are therefore confident that ballistic electron transport will continue to play an important role in organic device physics in the future.

Appendix A

Abbreviations & Symbols

A.1 Abbreviations

AFM atomic force microscopy

BEEM ballistic electron emission microscopy (also often used as a synonym to describe both ballistic electron emission microscopy and spectroscopy techniques)

BEES ballistic electron emission spectroscopy

BHEM ballistic hole emission microscopy

BHES ballistic hole emission spectroscopy

CBM conduction band minimum

EPR electron paramagnetic resonance

ESR electron spin resonance

FKE Institut für Festkörperelektronik der Technischen Universität Wien (Floragasse 7, A-1040 Wien)

HBC hexa-*peri* hexabenzocoronene

MBE molecular beam epitaxy

MISZ Mikrostrukturzentrum der Technischen Universität Wien (Floragasse 7, A-1040 Wien)

OFET organic field-effect transistor

OLED organic light emitting diode

PPP polyparaphenylene

PF polyfluorene

PPV polyparaphenylenevinylene

PT polythiophene

PTCDA perylene-3,4,9,10- tetracarboxylic- dianhydride

PTCDI 3,4,9,10-perylene-tetracarboxylic-diimide

SPM scanning probe microscopy, a term including a vast of local probe techniques, as for instance AFM, and STM.

SBH Schottky barrier height

SNOM scanning near field optical microscopy

STM scanning tunneling microscopy

STS scanning tunneling spectroscopy

TEM transmission electron microscopy

TiOPc titanylphthalocyanine

TPD 4,4'-bis(N-m-tolyl-N-phenylamino)biphenyl

UHV ultra high vaccum

A.2   Frequently Used Symbols

a_0 Bohr radius, $a_0 = \frac{\hbar^2}{m_0 e^2} = 0.529177$ Å

e elementary charge, $e = 1.60219 \times 10^{-19}$ C

m_0 free electron mass, $m_0 = 9.1095 \times 10^{-31}$ kg

m^* effective electron mass, $m^* = \hbar^2 (\frac{d^2 E}{dk^2})^{-1}$

k_B Boltzmann constant, $k_B = 1.38062 \times 10^{-23}$ J/K

E total energy

E_f Fermi energy

E_c conduction band edge

E_v valence band edge

E_i part of the kinetic energy associated with the i-th component of the wave vector momentum

E_i^0 initial value of E_i

E_{xy} kinetic energy component associated with k_{xy}

f Fermi distribution/Fermi function $f(E) = \frac{1}{e^{\frac{E-E_f}{k_B T}} + 1}$

I_c ballistic current (collector current)

I_t tunnel current

$\vec{k}$ wave vector, tied to the momentum $\vec{p}$ by $\vec{p} = \hbar \vec{k}$.

k_i component of the wave vector parallel to the i-th axis $(i = x, y, z)$

k_i^0 initial value of k_i

k_{xy} component of the wave vector parallel to the interface.

N_A acceptor concentration

N_D donor concentration

eV_b (Schottky) barrier height (in eV).

V_c collector voltage

V_t tunnel voltage

Appendix B

Publications in Reviewed Journals

- S. Özcan, T. Roch, G. Strasser, J. Smoliner, R. Franke and T. Fritz,
  "Ballistic Electron Emission Microscopy/Spectroscopy on Au/Titanylphthalocyanine/GaAs Heterostructures",
  J. Phys: Conf. Ser., 61, 1371, (2007).

- S. Özcan, J. Smoliner, M. Andrews, G. Strasser, T. Dienel, R. Franke and T. Fritz,
  "Ballistic Electron Transport Through Titanylphthalocyanine films",
  Appl. Phys. Lett., 90, 092107, selected for the "Virtual Journal of Nanoscale Science and Technology", March 12 (2007).

- S. Özcan, J. Smoliner, M. Andrews, G. Strasser, T. Dienel and T. Fritz,
  "Ballistic electron mean free path of titanylphthalocyanine films grown on GaAs",
  phys. stat. sol. (c), 5, No. 1, $386 - 389$, 2008.

- S. Özcan, J. Smoliner, M. Andrews, G. Strasser, T. Dienel, R. Franke and T. Fritz,
  "Ballistic Electron Attenuation Length in Titanylphthalocyanine films grown on GaAs",
  Semicond. Sci. Technol., *xxx*, *xxx*, 2008, accepted in print.

- S. Özcan, J. Smoliner, T. Dienel and T. Fritz,
  "Temperature Dependent Schottky Barrier Height and Fermi Level Pinning on Au/HBC/GaAs Diodes",
  Appl. Phys. Lett., *xxx*, *xxx*, 2008, submitted.

B.1 Conference Proceedings

- S. Özcan, T. Roch, G. Strasser, J. Smoliner, R. Franke and T. Fritz,
  "Ballistic Electron Emission Microscopy/Spectroscopy on Au/Titanylphthalocyanine/GaAs Heterostructures",
  Proceedings of the GMe-Workshop, Vienna 13. 10. 2006 ,K. Riedling (Hrg.); (2006), SBN: 978-3-901578-17-5; S. 71 - 75..

B.2 Other Publications

- H. Michor, M. El-Hagary, S. Özcan, A. Horyn, E. Bauer, M. Reissner, G. Hilscher, S. Khmelevskyi, P. Mohn and P. Rogl,
  "Weak itinerant ferromagnetism in YCo_9Si_4",
  Physica B 359, 1177 2005

- M. El-Hagary, H. Michor, S. Özcan, M. Giovanni, A. Matar, Z. Heiba, P. Kerschl M. Schönhart, E. Bauer, R. Grössinger, G. Hilscher, J. Freudenberger and H. Rosner,
  "Phase formation and ferrimagnetism of $GdCo_9Si_4$",
  J. Phys.: Condens. Matter 18, 4567 2006

- R. Grössinger, M. Schönhart, M. El-Hagary, H. Michor, S. Özcan, M. Giovanni, A. Matar, Z. Heiba, P. Kerschl, E. Bauer, G. Hilscher, J. Freudenberger and H. Rosner,
  "Phase formation and ferrimagnetism of $GdCo_{9-x}Si_{4+x}$",
  J. Phys.: Conf. Ser. 51, 139 2006

- Soner Özcan, T. Khmelevska, S. Khmelevska and P. Mohn
  "Site-preferences and local spin-polarization of transition metal solute atoms in B2 type Ni-Al alloys", *Intermetallics, xxx, xxx,* 2008, submitted.

Appendix C

Presentations within the Framework of this Thesis

C.1 Talks

- S. Özcan, J. Smoliner, M. Andrews, G. Strasser, T. Dienel and T. Fritz,
  "Hot Electron Transport Through Titanylphthalocyanine films",
  Talk: At the 15th International Conference on Nonequilibrium Carrier Dynamics in
  Semiconductors, Tokyo, Japan; July $23 - 27$, 2007.

- S. Özcan, T. Roch, G. Strasser, J. Smoliner, R. Franke, T. Fritz,
  "Ballistic Electron Emission Microscopy/Spectroscopy on Au/Titanylphthalocyanine/GaAs
  Heterostructure",
  Seminar-Talk: At the Inst. für angewandte Photophysik, TU-Dresden, Germany;
  27.4.2006.

- S. Özcan, J. Smoliner, T. Roch, G. Strasser, R. Franke, T. Fritz,
  "Ballistic Electron Emission Microscopy/Spectroscopy on Au/Titanylphthalocyanine/GaAs
  Heterostructures",
  Talk: At the Infrared Optical Nanostructures workshop, Wien; 12.05.2006.

C.2   Poster Presentations

- S. Özcan, J. Smoliner, M. Andrews, G. Strasser, T. Dienel and T. Fritz,
  "Ballistic Electron Transport Through Titanylphthalocyanine films",
  Poster: At the DPG-Tagungen, Regensburg, Germany; March 2007.

- S. Özcan, T. Roch, G. Strasser, J. Smoliner, R. Franke and T. Fritz,
  "Ballistic Electron Emission Microscopy/Spectroscopy on Au/Titanylphthalocyanine/GaAs
  Heterostructures",
  Poster: At the GMe-Workshop, Vienna, Austria; 13. 10. 2006

- S. Özcan, T. Roch, G. Strasser, J. Smoliner, R. Franke, T. Fritz,
  "Ballistic Electron Emission Microscopy/Spectroscopy on Au/Titanylphthalocyanine/GaAs
  Heterostructures",
  Poster: International Conference on Nanoscience and Technology (ICN+T), Basel
  Switzerland; 30.07.2006 - 04.08.2006.

Appendix D

Curriculum Vitae

EDUCATION

- March 2006 - April 2008
  PhD at the Technical University of Vienna
  Department of Solid State Electronics.
  Advisor: Prof. Dr. Jürgen Smoliner
  Title: "Ballistic Electron Emission Microscopy/Spectroscopy on Organic Semiconductors"

- Mai 2005 - March 2006 (not finished)
  PhD at the Technical University of Vienna
  Department of Business Mathematics.
  Advisor: Prof. Dr. Mafred Deistler
  Title: "Mathematical Modelling for Integrated Demand and Supply Chain Management"

- October 2001 - April 2005 (BSc+MSc)
  Technical University of Vienna
  Dipl. Ing. (corresponds to MSc) in Technical Physics
  Master Thesis
  Title: Research on Ferrimagnetism in $GdCo_{9-x}Si_{4+x}$
  Advisor: Prof. Dr. Herwig Michor and Prof. Dr. Gerfried Hilscher

- 1999 - 2001
  Externistenmatura at the Oberstufenrealgymnasium Hegelgasse 14**, Vienna**
  High School Diploma in two years.

- 1992 - 2001
  Several employers
  Bricklayer, Vienna.
  Waiter, Vienna.
  Waiter, Geelong, Victoria-Australia.
  Windsurfing instructor, Marmaris-Turkey.

- 1984 - 1992
  Primary- and middle-school, Vienna

- 1977
  Born in Carsamba-Samsun-Turkey

ACADEMIC AWARDS

- Advancement Scholarship 2004
  Technical University of Vienna, Faculty of Physics.

- Merit Scholarship 2005
  Technical University of Vienna, Faculty of Physics.

- Advancement Scholarship 2007
  Technical University of Vienna, Faculty of Electrical Engineering and Information Technology.

Bibliography

[1] G. Binning, G. Rohrer, C. Gerber, and E. Weibel, *Phys. Rev. Lett.* **49**, 57 (1982).

[2] G. Binning, G. Rohrer, C. Gerber, and E. Weibel, *Phys. Rev. Lett.* **50**, 120 (1983).

[3] L. D. Bell and W. J. Kaiser, *Phys. Rev. Lett.* **61**, 2368 (1988).

[4] W. J. Kaiser and L. D. Bell, *Phys. Rev. Lett.* **60**, 1408 (1988).

[5] X. Cheng, D. A. Collins, and T. C. McGill, *J. Vac. Sci. Technol. A* **15**, 2063 (1997).

[6] M. L. Ke, D. I. Westwood, C. C. Matthai, B. E. Richardson, and R. H. Williams, *Phys. Rev. B* **53**, 4845 (1996).

[7] J. J. O. Shea, E. G. Brazel, M. E. Rubin, S. Bhargava, M. A. Chin, and V. Narayanamurti, *Phys. Rev. B* **56**, 2026 (1997).

[8] A. Bauer, M. T. Cuberes, M. Prietsch, and G. Kaindl, *Phys. Rev. Lett.* **71**, 149 (1993).

[9] M. Kozhevnikov, V. Narayanamurti, A. Mascarenhas, Y. Zhang, J. M. Olson, and D. L. Smith, *Appl. Phys. Lett.* **75**, 1128 (1999).

[10] J. J. O. Shea, C. M. Reaves, S. P. DenBaars, M. A. Chin, and V. Narayanamurti, *Appl. Phys. Lett.* **69**, 3022 (1994).

[11] L. D. Bell, R. P. Smith, B. T. McDermott, E. R. Gertner, R. Pittman, R. L. Pierson, and G. J. Sullivan, *J. Vac. Sci. Technol. B* **16**, 2286 (1998).

[12] L. D. Bell, R. P. Smith, B. T. McDermott, E. R. Gertner, R. Pittman, R. L. Pierson, and G. J. Sullivan, *Appl. Phys. Lett.* **76**, 1725 (2000).

[13] E. G. Brazel, M. A. Chin, and V. Narayanamurti, *Appl. Phys. Lett.* **74**, 2367 (1999).

[14] M. Kozhevnikov, V. Narayanamurti, C. V. Reddy, H. P. Xin, C. W. Tu, A. Mascarenhas, and Y. Zhang, *Phys. Rev. B* **61**, 7861 (2000).

[15] L. D. Bell, S. J. Manion, M. H. Hecht, W. J. Kaiser, R. W. Fathauer, and A. M. Milliken, *Phys. Rev. B* **48**, 5712 (1993).

[16] K. Reuter, F. J. Garcia-Vidal, P. L. de Andres, F. Flores, and K. Heinz, *Phys. Rev. Lett.* **81**, 4963 (1999).

[17] B. Kaczer, H. Im, J. P. Pelz, and J. Chen, *Phys. Rev. B* **57**, 4027 (1998).

[18] M. T. Cuberes, A. Bauer, H. J. Wen, M. Prietsch, and G. Kaindl, *J. Vac. Sci. Technol. B* **12**, 2646 (1994).

[19] R. Ludeke, A. Bauer, and E. Cartier, *Appl. Phys. Lett.* **66**, 730 (1995).

[20] B. Kaczer and J. P. Pelz, *J. Vac. Sci. Technol. B* **14**, 2864 (1994).

[21] R. Ludeke, H. J. Wen, and A. Schenk, *Appl. Phys. Lett.* **73**, 1221 (1998).

[22] S. Bhargava, C. Zheng, J. Ko, M. A. Chin, L. A. Coldren, and V. Narayanamurti, *Appl. Phys. Lett.* **73**, 3271 (1998).

[23] S. Bhargava, H.-R. Blank, E. Hall, H. Kroemer, and V. Narayanamurti, *Appl. Phys. Lett.* **74**, 1135 (1999).

[24] D. K. Guthrie, P. N. First, T. K. G. E. N. Glytsis, and R. E. Leibenguth, *Appl. Phys. Lett.* **71**, 2292 (1997).

[25] T. Sajoto, J. J. O'Shea, S. Bhargava, D. Leonard, M. A. Chin, and V. Narayanamurti, *Phys. Rev. Lett.* **74**, 3427 (1995).

[26] R. Heer, J. Smoliner, G. Strasser, and E. Gornik, *Appl. Phys. Lett.* **73**, 1218 (1998).

[27] J. Smoliner, R. Heer, C. Eder, and G. Strasser, *Phys. Rev. B* **58**, 7516 (1998).

[28] J. Smoliner, C. Eder, G. Böhm, and G. Weimann, *Appl. Phys. Lett.* **69**, 52 (1996).

[29] C. Eder, J. Smoliner, G. Strasser, and E. Gornik, *Appl. Phys. Lett.* **68**, 2876 (1996).

[30] M. E. Rubin, G. Medeiros-Ribeiro, J. J. O'Shea, M. A. Chin, E. Y. Lee, P. M. Petroff, and V. Narayanamurti, *Phys. Rev. Lett.* **77**, 5268 (1996).

[31] M. E. Rubin, H. Blank, M. A. Chin, H. Kroemer, and V. Narayanamurti, *Appl. Phys. Lett.* **70**, 1590 (1997).

[32] C. V. Reddy, V. Narayanamurti, J. H. Ryou, U. Chowdhury, and R. D. Dupuis, *Appl. Phys. Lett.* **76**, 1437 (2000).

[33] H. Sirringhaus, E. Y. Lee, U. Kafader, and H. von Kanel, *J. Vac. Sci. Technol. B* **13**, 1848 (1995).

[34] E. Y. Lee, S. Bhargava, K. Pond, K. Luo, M. A. Chin, and V. Narayanamurti, *Appl. Phys. Lett.* **69**, 940 (1996).

[35] E. Y. Lee, S. Bhargava, M. A. Chin, and V. Narayanamurti, *J. Vac. Sci. Technol. A* **15**, 1351 (1997).

[36] C. Troadec, L. Kunardi, and N. Chandrasekhar, *Appl. Phys. Lett.* **86**, 072101 (2005).

[37] C. Troadec, D. Jie, L. Kunardi, S. J. O'Shea, and N. Chandrasekhar, *Nanotech.* **15**, 1818 (2004).

[38] L. Kunardi, C. Troadec, and N. Chandrasekhar, *J. Chem. Phys.* **122**, 204702 (2005).

[39] W. Li, K. L. Kavanagh, C. M. Matzke, A. A. Talin, F. Léonard, S-Faleev, and J. W. P. Hsu, *J. Phys. Chem. B* **109**, 6252 (2005).

[40] J. W. P. Hsu, D. V. Lang, K. W. West, Y.-L. Loo, M. D. Halls, and K. Raghavachari, *J. Phys. Chem. B* **109**, 5719 (2005).

[41] H. Haick, J. P. Pelz, T. Ligonzo, M. Ambrico, D. Cahen, W. Cai, C. Marginean, C. Tivarus, and R. T. Tung, *Phys. Stat. Sol.* **203**, 3438 (2006).

[42] A. Bannani, C. Bobisch, and R. Möller, *Science* **315**, 1824 (2007).

[43] S. Özcan, J. Smoliner, M. Andrews, G. Strasser, T. Dienel, and T. Fritz, *Appl. Phys. Lett.* **90**, 092107 (2007).

[44] S. Özcan, T. Roch, G. S. J. Smoliner, R. Franke, and T. Fritz, *J. Phys.: Conf. Ser.* **61**, 1371 (2007).

[45] S. Özcan, T. Roch, G. S. J. Smoliner, R. Franke, and T. Fritz, *Proceedings of the GMe-Workshop, Vienna* 13. 10. 2006 *,K. Riedling (Hrg.);SBN:* 978-3-901578-17-5*; S.* 71 - 75.. (2006).

[46] S. Özcan, J. Smoliner, M. Andrews, G. Strasser, T. Dienel, and T. Fritz, *phys. stat. sol. (c)* **5**, 386 (2008).

[47] S. Özcan, J. Smoliner, A. M. Andrews, G. Strasser, T. Dienel, R. Franke, and T. Fritz, *Semicond. Sci. Technol.* **xxx**, xxx (2008).

[48] S. Özcan, J. Smoliner, T. Dienel, and T. Fritz, *Appl. Phys. Lett.* **xxx**, xxx (2008).

[49] T. Nishi, K. Kanai, Y. Ouchi, M. R. Willis, and K. Seki, *Chem. Phys. Lett.* **414**, 479 (2005).

[50] J. J. Boland, *Surf. Sci.* **144**, 1 (1991).

[51] Y. Mo, J. Kleiner, M. B. Webb, and M. G. Lagally, *Phys. Rev. Lett.* **66**, 1998 (1991).

[52] D. A. Bonnel, *Scanning Probe Microscopy and Spectroscopy: Theory, Techniques and Applications 2nd edn*, Wiley, New York, 2000.

[53] C. J. Chen, *Introduction to Scanning Tunneling Microscopy*, Oxford University Press, Oxford, 1993.

[54] R. Wiesendanger, *Scanning Probe Microscopy and Spectroscopy: Methods and Applications*, Cambridge University Press, Cambridge, 1994.

[55] L. D. Bell, W. J. Kaiser, M. H. Hecht, and L. C. Davies, *Methods of Experimental Physics*, Academic, Dordrecht, 1993.

[56] E. L. Wolf, *Principles of Electron Tunneling Spectroscopy*, Oxford University Press, Oxford, 1985.

[57] F. Schwabl, *Quantenmechanik 2nd edn*, Springer, Berlin, 1990.

[58] R. Ludeke and A. Bauer, *Phys. Rev. Lett.* **71**, 1760 (1993).

[59] A. J. Stollenwerk, M. R. Krause, D. H. Idell, R. Moore, and V. P. LaBella, *Phys. Rev. B* **74**, 155328 (2006).

[60] D. L. Smith, E. Y. Lee, and V. Narayanamurti, *Phys. Rev. Lett.* **80**, 2433 (1998).

[61] I. Appelbaum and V. Narayanamurti, *Phys. Rev. B* **71**, 045320 (2005).

[62] N. Machida, S. Satoh, and K. Furuya, *Surf. Sci.* **600**, 4843 (2006).

[63] D. L. Smith and S. M. Kogan, *Phys. Rev. B* **54**, 10354 (1996).

[64] J. W. McNaab and H. G. Craighead, *J. Vac. Sci. Technol. B* **14**, 617 (1996).

[65] C. A. Ventrice, V. P. L. Bella, G. Ramaswamy, H. P. Yu, and L. J. Schowalter, *Appl. Surf. Sci.* **104/105**, 274 (1996).

[66] J. Smoliner, C. Eder, G. Strasser, and E. Gornik, *phys. stat. sol. (b)* **204**, 386 (1997).

[67] J. Smoliner and C. Eder, *Phys. Rev. B* **57**, 9856 (1998).

[68] J. Smoliner, R. Heer, and G. Strasser, *Phys. Rev. B* **60**, 5137 (1999).

[69] J. Smoliner, R. Heer, G. Ploner, and G. Strasser, *Physica E* **6**, 339 (2000).

[70] J. Smoliner, D. Rakoczy, and M. Kast, *Rep Prog. Phys.* **67**, 1863 (2004).

[71] R. HEER, , C. EDER, J. SMOLINER, and E. GORNIK, *Rev. Sci. Instrum.* **68**, 4488 (1997).

[72] R. HEER, , D. RAKOCZY, G. PLANER, G. STRASSER, E. GORNIK, and J. SMOLINER, *Appl. Phys. Lett.* **75**, 4007 (1999).

[73] R. HEER, J. SMOLINER, G. STRASSER, and E. GORNIK, *Phys. Rev. B* **59**, 4618 (1999).

[74] R. HEER, J. SMOLINER, and G. STRASSER, *Physica B* **272**, 187 (1999).

[75] R. HEER, J. SMOLINER, J. BORNEMEIER, and H. BRÜCKL, *Appl. Phys. Lett.* **85**, 4388 (2004).

[76] D. RAKOCZY, J. SMOLINER, R. HEER, and G. STRASSER, *Appl. Phys. Lett.* **88**, 3495 (2000).

[77] D. RAKOCZY, G. STRASSER, and J. SMOLINER, *Physica B* **314**, 81 (2002).

[78] D. RAKOCZY, G. STRASSER, C. STRAHBERGER, and J. SMOLINER, *Phys. Rev. B* **66**, 033309 (2002).

[79] D. RAKOCZY, G. STRASSER, and J. SMOLINER, *Appl. Phys. Lett.* **81**, 4964 (2002).

[80] D. RAKOCZY, G. STRASSER, and J. SMOLINER, *J. Vac. Sci. Technol. B* **20**, 1071 (2002).

[81] D. RAKOCZY, R. HEER, G. STRASSER, and J. SMOLINER, *Physica E* **16**, 139 (2003).

[82] D. RAKOCZY, G. STRASSER, and J. SMOLINER, *Phys. Rev. B* **68**, 073304 (2003).

[83] D. RAKOCZY, G. STRASSER, C. PACHER, and J. SMOLINER, *Semicond. Sci. Technol.* **19**, 8 (2004).

[84] D. RAKOCZY, G. STRASSER, and J. SMOLINER, *App. Phys. Lett.* **86**, 202112 (2005).

[85] C. EDER, J. SMOLINER, G. STRASSER, and E. GORNIK, *Appl. Phys. Lett.* **69**, 1725 (1996).

[86] C. Girardin, R. Coratger, R. Pechou, F. Ajustron, and J. Beauvillain, *J. Phys. France* **6**, 661 (1996).

[87] K. J. Russel, V. Narayanamurti, I. Appelbaum, M. P. Hanson, and A. C. Gossard, *Phys. Rev. B* **74**, 205330 (2006).

[88] R. Menegozzi, P.-G. Reinhard, and M. Schulz, *Appl. Phys. A* **66**, 897 (1998).

[89] G. M. Vanalme, R. L. V. Meirhaeghe, F. Cardon, and P. V. Daele, *Semicond. Sci. Technol.* **12**, 907 (1997).

[90] A. Saskai, *Phys. Rev. B* **30**, 7016 (1984).

[91] E. O. Kane, *Tunneling Phenomena in Solids eds E. Burnstein and S. Lundquist*, Plenum, New York, 1969.

[92] B. Rico and M. Y. Azbel, *Phys. Rev. B* **29**, 1970 (1984).

[93] A. Tsumura, H. Koezuba, and T. Ando, *Appl. Phys. Lett.* **49**, 1210 (1986).

[94] C. W. Tang and S. A. VanSlyke, *Appl. Phys. Lett.* **51**, 913 (1987).

[95] J. H. Burroughes, D. D. C. Bradley, A. R. Brown, R. N. Marks, K. MacKay, R. H. Friend, P. L. Burn, and A. B. Holmes, *Nature* **347**, 539 (1990).

[96] G. Horowitz, *Adv. Mater.* **10**, 365 (1998).

[97] Z. Bao, J. A. Rogers, and H. E. Katz, *J. Mater. Chem.* **9**, 1895 (1999).

[98] C. D. Dimitrakopoulos and P. R. L. Malenfant, *Adv. Mater.* **14**, 99 (2002).

[99] C. D. Dimitrakopoulos, *Thin -Film Transistors*, 2003.

[100] C. J. Brabec, N. S. Sariciftci, and J. C. Hummelen, *Adv. Funct. Mater.* **11**, 15 (2001).

[101] K. M. Koakley and M. D. McGehee, *Chem. Mater.* **16**, 4533 (2004).

[102] B. Crone, A. Dolabalapur, A. Gelperin, L. Torsi, H. E. Katz, A. J. Lovinger, and Z. Bao, *Appl. Phys. Lett.* **78**, 2229 (2001).

[103] T. Someya, H. E. Katz, A. Gelperin, A. J. Lovinger, and A. Dolabalapur, *Appl. Phys. Lett.* **81**, 3079 (2002).

[104] A. R. Brown, A. Promp, C. M. Hart, and D. M. Deleeuw, *Science* **270**, 972 (1995).

[105] B. Crone, A. Dolabalapur, Y. Y. Lin, R. W. Filas, Z. B. A. LaDuca, R. Sarpeshkar, and H. E. Katz, *Nature* **403**, 521 (2000).

[106] C. J. Drury, C. M. L. Mutsaers, C. M. Hart, and D. M. Leeuw, *Appl. Phys. Lett.* **73**, 108 (1998).

[107] S. R. Forrest, *Nature* **428**, 911 (2004).

[108] F. Gutmann and L. E. Lyons, *Organic Semiconductors*, Wiley, New York, 1967.

[109] W. R. Salaneck, S. Strafström, and J. L. Brédas, *Conjugated Polymer Surfaces and Interfaces: Electronic and Chemical Structure of Interfaces for Polymer Light Emitting Devices*, Cambridge University Press, Cambridge, 1996.

[110] D. P. Woodruff and T. A. Delchar, *Modern Techniques of Surface Science*, Cambridge University Press, Cambridge, 1986.

[111] J. Hoelzel, F. K. Schulte, and H. Wagner, *Solid State Surface Physics*, Springer, Berlin, 1979.

[112] L. J. Brillson, *Surf. Sci. Rep.* **2**, 123 (1982).

[113] W. Mönch, *Surf. Sci.* **299/300**, 928 (1994).

[114] K. Sugiyama, D. Yoshimura, E. Ito, T. M. andY. Hamatani, I. Kawamoto, Y. Ouchi, and K. Seki, *Mol. Cryst. Liq. Cryst.* **286**, 239 (1996).

[115] H. Ishii and K. Seki, *IEEE Trans. Electron Dev.* **44**, 1295 (1997).

[116] D. D. Eley and G. D. Parfitt, *Trans. Faraday Soc.* **51**, 1529 (1955).

[117] D. D. Eley and D. Spivey, *Trans. Faraday Soc.* **56**, 1432 (1960).

[118] R. A. Keller and H. E. Rast, *J. Chem. Phys.* **36**, 2640 (1962).

[119] R. A. KELLER, *J. Chem. Phys.* **38**, 1076 (1963).

[120] A. REMBAUM, J. MOACANIN, and H. A. POHL, *Progres in Dielectrics*, J. B. Birks ed., Heywood, London, 1965.

[121] H. MEIER, *Spectral Sensitization*, Focal Press, London/New York, 1968.

[122] H. MEIER, *Angew. Chem.* **77**, 633 (1963).

[123] G. H. HEILMEIER and S. E. HARRISON, *J. Appl. Phys.* **34**, 2732 (163).

[124] F. J. MORIN, *Phys. Rev.* **93**, 1195 (1954).

[125] S. H. GLARUM, *J. Phys. Chem. Solids* **24**, 1577 (1963).

[126] D. A. SEANOR, *Adv. Polymer Sci.* **4**, 317 (1965).

[127] J. SINGH, *Quantum Mechanics: Fundamentals and Applications to technology*, Wiley, New York, 1996.

[128] O. D. JURCHESCU, J. BAAS, and T. T. M. PALSTRA, *Appl. Phys. Lett.* **84**, 3061 (2004).

[129] R. W. I. DE BOER, M. E. GERSHENSON, A. F. MORPURGO, and V. PODROZOV, *Phys. Status Solidi A* **201**, 1302 (2004).

[130] M. POPE and C. E. SWENBERG, *Electronic Processes in Organic Crystals and Polymers, 2nd ed*, Oxford University Press, New York, 1999.

[131] I. M. RUTENBERG, O. A. SCHERMAN, R. H. G. ANDW. R. JIANG E. GARFUNKEL, and Z. J. BAO, *J. Am.Chem. Soc.* **126**, 4062 (2004).

[132] C. C. MATTHEUS, G. A. DE WIJS, R. A. DE GROT, and T. T. M. PALSTRA, *J. Am. Chem. Soc.* **125**, 6323 (2003).

[133] V. PODROZOV, V. M. PUDALOV, and M. E. GERSHENSON, *Appl. Phys. Lett.* **82**, 1739 (2003).

[134] C. GOLDMANN, S. HAAS, C. KRELLNER, K. P. PERNSTRICH, D. J. GRUNDLACH, and B. J. BATLOGG, *J. Appl. Phys.* **96**, 2080 (2004).

[135] R. Zeis, C. Besnard, T. Siegrist, C. Schlockermann, X. L. Chi, and C. Kloc, *Chem. Mater.* **18**, 244 (2006).

[136] V. C. Sundar, J. Zaumseil, V. Podrozov, E. Menard, L. R. Willett, T. Someya, M. E. Gershenson, and J. A. Rogers, *Science* **303**, 1644 (2004).

[137] V. Podrozov, E. Menard, A. Borissov, V. Kiryukhin, J. Rogers, and M. E. Gershenson, *Phys. Rev. Lett.* **93**, 086602 (2004).

[138] D. Fichou, B. Bachet, F. Demanze, I. Billy, G. Horowitz, and F. Garnier, F. *Adv. Mater.* **8**, 500 (1996).

[139] D. Fichou, *J. Mater. Chem.* **10**, 571 (2000).

[140] P. C. Chang, J. Lee, D. Huang, V. Subramanian, A. R. Murphy, and J. M. Frechet, *J. Chem. Mater.* **16**, 4783 (2004).

[141] F. Garnier, R. Hajlaoui, A. Yassar, and P. Srivastava, *Science* **265**, 1684 (1994).

[142] Y. Sakamoto, T. Suzuki, M. Kobayashi, Y. Gao, Y. Fukai, Y. Inoue, F. Sato, and S. Tokito, *J. Am. Chem. Soc.* **126**, 8138 (2004).

[143] M. H. Yoon, A. Facchetti, C. E. Stern, and T. J. Marks, *J. Am. Chem. Soc.* **128**, 5792 (2006).

[144] C. R. Newman, C. D. Frisbie, D. A. da Silva, J. L. Bredas, P. C. Ewbank, and K. R. Mann, *Chem. Mater.* **16**, 4436 (2004).

[145] B. A. Jones, M. J. Ahrens, M. H. Yoon, A. Facchetti, T. J. Marks, and M. R. Wasielewski, *Angew. Chem. Int. Ed.* **43**, 6363 (2004).

[146] D. Adam, P. Schuhmacher, J. Simmerer, L. Haussling, K. Siemensmeyer, K. H. Etzbach, H. Ringsdorf, and D. Haarer, *Nature* **371**, 141 (1994).

[147] A. V. de Craats, J. M. Warman, A. Fechtenkötters, J. D. Brandt, M. Harbison, and K. Müllen, *Adv. Mater.* **11**, 1469 (1999).

[148] M. Funahashi and J. Hanna, *Phys. Rev. Lett.* **78**, 2184 (1997).

[149] I. Shiyanovskaya, K. D. Singer, R. J. Twieg, L. Sukhomlinova, and V. Gettwert, *Phys. Rev. E* **65**, 041715 (2002).

[150] S. Ducharme and P. M. Borsenberger, *Xerographic Photoreceptors and Photorefractive Polymers, July 10-11, 1995, San Dieogo, CA;*, Society of Photo-optical Instrumentation Engineers, Bellingham, WA, 1995.

[151] Y. Shirota, *J. Mater. Chem.* **15**, 75 (2005).

[152] A. Camerman and J. Trotter, *Proc. R. Soc. London, A* **279**, 129 (1964).

[153] P. V. Pesavento, R. J. Chesterfield, C. R. Newman, and C. D. Frisbie, *J. Appl. Phys.* **96**, 7312 (2004).

[154] J. Ferraris, D. O. Cowan, V. Walatka, and J. H. Perlstein, *J. Am. Chem. Soc.* **95**, 948 (1973).

[155] T. Otsubo and K. Takimiva, *Bull. Chem. Soc. Jpn.* **77**, 43 (2004).

[156] C. Rovira, *Chem. Rev.* **104**, 5289 (2004).

[157] M. Mas-Torrent, M. Durkut, P. Hadley, X. Ribas, and C. Rovira, *J. Am. Chem. Soc.* **126**, 984 (2004).

[158] M. Mas-Torrent, P. Hadley, S. T. Bromley, N. Crivillers, J. Veciana, and C. Rovira, *Appl. Phys. Lett.* **86**, 012110 (2005).

[159] R. C. Haddon, A. S. Morris, R. C. Morris, T. T. M. Palstra, A. F. Hebard, and R. M. Fleming, *Appl. Phys. Lett.* **67**, 121 (1995).

[160] E. Frankevich, Y. Maruyama, H. Ogata, Y. Achiba, and K. Kikuchi, *Solid State Commun.* **88**, 177 (1993).

[161] T. Durkop, B. M. Kim, and M. S. Fuhrer, *J. Phys.: Condens. Matter* **16**, R553 (2004).

[162] H. Sirringhaus, P. J. Brown, R. H. Friend, M. M. N. K. Bechgaard, B. M. W. Langeveld-Voss, A. J. H. Spiering, R. A. J. Janssen, E. W. Meijer, P. Herwig, and D. M. de Leeuw, *Nature* **401**, 685 (1999).

[163] I. MCCULLOCH, M. HEENEY, C. BAILEY, K. GENEVICIUS, I. MACDONALD, M. SHKUNOV, D. SPARROWE, S. TIERNEY, R. WAGNER, M. W. ZHANG, M. L. CHABINYC, R. J. KLINE, M. D. MCGHEE, and M. F. TONEY, *Nat. Mater.* **5**, 328 (2006).

[164] H. SIRRINGHAUS, R. J. WILSON, R. H. FRIEND, M. INBASEKARAN, W. WU, E. P. WOO, M. GRELL, and D. D. C. BRADLEY, *Appl. Phys. Lett.* **77**, 406 (2000).

[165] R. H. FRIEND, R. W. GYMER, A. B. HOLMES, J. H. BURROUGHES, R. N. MARKS, C. TALIANI, D. D. C. BRADLEY, D. A. D. SANTOS, J. L. BREDAS, M. LOGDLUND, and W. R. SALANECK, *Nature* **397**, 121 (1999).

[166] M. T. BERNIUS, M. INBASEKARAN, J. O'BRIAN, and W. S. WU, *Adv. Mater.* **12**, 1737 (2000).

[167] A. BABEL and S. A. JENEKHE, *Adv. Mater.* **14**, 371 (2002).

[168] J. L. BREDAS, J. P. CALBERT, D. A. DA SILVA, and J. CORNIL, *J. Proc. Natl. Acad. Sci. U.S.A.* **99**, 5804 (2002).

[169] J. CORNIL, D. BELJONNE, J. P. CALBERT, and J. L. BREDAS, *Adv. Mater.* **13**, 1053 (2001).

[170] V. KAZUKAUSKAS, H. TZENG, and S. A. CHEN, *Appl. Phys. Lett.* **80**, 2017 (2002).

[171] E. C. P. SMITS, T. D. ANTHOPOULOS, S. SETAYESH, E. VAN VEENENDAAL, R. COEHOORN, P. W. M. BLOM, B. DE BOER, and D. M. DE LEEUW, *Phys. Rev. B* **73**, 205316 (2006).

[172] L. L. CHUA, J. ZAUMSEIL, J. F. CHANG, E. C. W. OU, P. K. H. HO, H. SIRRINGHAUS, and R. H. FRIEND, *Nature* **434**, 194 (2005).

[173] J. Y. LEE, S. ROTH, and Y. W. PARK, *Appl. Phys. Lett.* **88**, 252106 (2006).

[174] C. D. DIMITRAKOPOULOS, S. PURUSHOTHAMAM, J. KYMISSIS, A. CALLEGARI, and J. M. SHAW, *Science* **283**, 822 (1999).

[175] J. M. WARMAN, M. P. DE HAAS G. DICKER, F. C. GROZEMA, J. PIRIS, and M. G. DEBIJE, *Chem. Mater.* **16**, 4600 (2004).

[176] E. F. Valeev, V. Coropceanu, D. A. da Silva, S. Salman, and J. L. Bredas, *J. Am. Chem. Soc.* **128**, 9882 (2006).

[177] A. Dieckmann, H. Bassler, and P. M. Borsenberger, *J. Chem. Phys.* **99**, 8136 (1993).

[178] P. M. Borsenberger and J. J. Fitzgerald, *J. Phys. Chem.* **97**, 4815 (1993).

[179] D. H. Dunlap, P. E. Parris, and V. M. Kenkre, *Phys. Rev. Lett.* **77**, 542 (1996).

[180] S. V. Novikov, *J. Polym. Sci., Part B: Polym. Phys.* **41**, 2584 (2003).

[181] P. W. M. Blom, M. J. M. de Jong, and M. G. van Munster, *Phys. Rev. B* **55**, R656 (1997).

[182] H. Sirringhaus, *Adv. Mater.* **17**, 2411 (2005).

[183] N. Karl and C. Günther, *Cryst. Res. Technol.* **34**, 243 (1999).

[184] C. D. Dimitrakopoulos and D. J. Mascaro, *IBM J. Res. Develop.* **45**, 11 (2001).

[185] P. G. Lecomber and W. E. Spear, *Phys. Rev. Lett.* **25**, 509 (1970).

[186] F. W. Schmidlin, *Phys. Rev. B* **16**, 2362 (1977).

[187] J. Noolandi, *Phys. Rev. B* **16**, 4474 (1977).

[188] H. Scher and M. Lax, *Phys. Rev. B* **7**, 4491 (1973).

[189] G. Horowitz and M. E. Hajlaoui, *Adv. Mater.* **12**, 1046 (2000).

[190] R. J. Chesterfield, J. C. McKeen, C. R. Newman, P. C. Ewbank, D. A. da Silva, J. L. Bredas, L. L. Miller, K. R. Mann, and D. C. Frisbie, *J. Physc. Chem. B* **108**, 19281 (2004).

[191] V. R. Nikitenko, H. Heil, and H. von Seggern, *J. Appl. Phys.* **94**, 2480 (2003).

[192] P. Prins, L. P. Candeias, A. J. J. M. van Breemen, J. Sweelssen, P. T. Herwig, H. F. M. Schoo, and L. D. A. Siebbeles, *Adv. Mater.* **17**, 718 (2006).

[193] J. VERES, S. D. OGIER, S. W. LEEMING, D. C. CUPERTINO, and S. M. KHAFFAF, *Adv. Funct. Mater.* **13**, 199 (2003).

[194] P. W. M. BLOM, M. J. M. DE JONG, and J. J. M. VLEGGAAR, *Appl. Phys. Lett.* **68**, 3308 (1996).

[195] L. B. SCHEIN and A. R. MCGHIE, *Phys. Rev. B* **20**, 1631 (1979).

[196] C. GOH, R. J. KLINE, M. D. MCGEHEE, E. N. KADNIKOVA, and J. M. J. FRECHET, *Appl. Phys. Lett.* **86**, 122110 (2005).

[197] W. ZHU, S. J. SINGER, Z. ZHENG, and A. T. CONLISK, *Phys. Rev. E* **71**, 041501 (2005).

[198] H. BASSLER, *Phys. Status Solidi B* **175**, 15 (1993).

[199] A. J. MOZER, P. DENK, M. C. SCHARBER, H. NEUGEBAUER, and N. S. SARI-CIFTCI, *J. Phys. Chem. B* **108**, 5235 (2004).

[200] A. J. MOZER and N. S. SARICIFTCI, *Chem. Phys. Lett.* **389**, 438 (2004).

[201] A. J. MOZER, N. S. SARICIFTCI, A. PIVRIKAS, R. OSTERBACKA, G. JUSKA, L. BRASSAT, and H. BASSLER, *Phys. Rev. B* **71**, 035214 (2005).

[202] W. D. GILL, *J. Appl. Phys.* **43**, 5033 (1972).

[203] D. M. PAI, *J. Chem. Phys.* **52**, 2285 (1970).

[204] M. CHANDRASEKHAR, S. GUHA, and W. GRAUPNER, *Adv.Mater.* **13**, 613 (2001).

[205] A. M. VAN DE CRAATS and J. M. WARMAN, *Adv. Mater.* **13**, 130 (2001).

[206] A. ZEN, J. PFLAUM, S. HIRSCHMANN, W. ZHUANG, F. JAISER, U. ASAWAPIROM, J. P. RABE, U. SCHERF, and D. NEHER, *Adv. Func. Mater.* **14**, 757 (2004).

[207] V. LEMAUR, D. A. DA SILVA FILHO, V. COROPCEANU, M. LEHMANN, Y. GEERTS, J. PIRIS, M. G. DEBIJE, A. M. VAN DE CRAATS, K. SENTHILKUMAR, L. D. A. SIEBBELES, J. M. WARMAN, J. L. BREDAS, and J. CORNIL, *J. Am. Chem. Soc.* **126**, 3271 (2004).

[208] Z. Rang, A. Haraldsson, D. M. Kim, P. P. Ruden, M. I. Nathan, R. J. Chesterfield, and C. D. Frisbie, *App. Phys. Lett.* **79**, 2731 (2001).

[209] C. Y. Liu and A. J. Bard, *Nature* **418**, 162 (2002).

[210] J. L. Bredas, D. Beljonne, V. Coropceanu, J. P. Calbert, and J. Cornil, *J. Chem. Rev.* **104**, 4971 (2004).

[211] E. Silinsh and V. Cápek, *Organic Molecular Crystals: Interaction, Localization, and Transport Phenomena*, American Institute of Physics, New York, 1994.

[212] R. G. D. Valle, E. Venuti, L. Farina, A. Brillante, M. Masino, and A. Girlando, *J. Phys. Chem. B* **108**, 1822 (2004).

[213] M. L. Tiago, J. E. Northrup, and S. G. Louie, *Phys. Rev. B* **67**, 115212 (2003).

[214] A. Troisi and G. Orlandi, *J. Phys. Chem. B* **109**, 1849 (2005).

[215] A. Troisi, G. Orlandi, and J. E. Anthony, *Chem. Mater.* **17**, 5024 (2005).

[216] G. R. Hutchison, M. A. Ratner, and T. J. Marks, *J. Am. Chem. Soc.* **127**, 16866 (2005).

[217] O. Kwon, V. Coropceanu, N. E. Gruhn, J. C. Durivage, J. G. Laquindanum, H. E. Katz, J. Cornil, and J. L. Bredas, *J. Chem. Phys.* **120**, 8186 (2004).

[218] D. Knipp, R. A. Street, A. Volkel, and J. Ho, *J. Appl. Phys.* **93**, 347 (2003).

[219] T. Holstein, *Ann. Phys.* **8**, 325 (1959).

[220] T. Holstein, *Ann. Phys.* **8**, 343 (1959).

[221] R. W. Muhn and R. Silbey, *J. Chem. Phys.* **83**, 1843 (1985).

[222] R. W. Muhn and R. Silbey, *J. Chem. Phys.* **83**, 1854 (1985).

[223] Y. Zhao, D. W. Brown, and K. Lindenberg, *J. Chem. Phys.* **100**, 2335 (1994).

[224] K. Hannewald, V. M. Stojanovic, and P. A. Bobbert, *J. Phys.: Condens. Matter.* **16**, 2023 (2004).

[225] K. Hannewald, V. M. Stojanovic, J. M. T. S. P. A. Bobbert, G. Kresse, and J. Hafner, *Phys. Rev. B* **69**, 075211 (2004).

[226] V. M. Stojanovic, P. A. Bobbert, and M. A. Michels, *Phys. Rev. B* **69**, 144302 (2004).

[227] R. E. Peierls, *Quantum Theory of Solids*, Clarendon Press, Oxford, 1955.

[228] E. M. Conwell, *Phys. Rev. B* **22**, 1761 (1980).

[229] N. B. McKeown, *Phthalacyanine Materials: Synthesis, Structure and Function Theory, Techniques and Applications 2nd edn*, Cambrigde University Press, Cambrigde, 1998.

[230] K. Walzer, T. Toccoli, A. Pallaori, R. Verucchi, T. Fritz, K. Leo, A. Boschetti, and S. Iannotte, *Surf. Sci.* **573**, 346 (2004).

[231] C. C. Leznoff and A. B. P. Lever, *Phthalocyanines: Synthesis, Properties and Applications*, volume 4, VCH, Weinheim, 1996.

[232] P. M. Borsenberger and D. S. Weiss, *Organic Photoreceptors for Imaging Systems*, Marcel Dekker, New York, 1993.

[233] K.-Y. Law, *Chem. Rev.* **93**, 449 (1993).

[234] T. Enokida, R. Hirohashi, and T. Nakamura, *J. Imaging. Sci.* **34**, 234 (1990).

[235] S. A. Jenekhe and S. Yi, *Adv. Mater.* **12**, 1274 (2000).

[236] M. Martin, J.-J. André, and J. Simon, *J. Appl. Phys.* **54**, 2792 (1983).

[237] T. Shimada, K. Hamaguchi, A. Koma, and F. S. Ohuchi, *Appl. Phys. Lett.* **72**, 1869 (1998).

[238] C. A. Jennings, R. Aroca, G. J. Kovacs, and C. Hsaio, *J. Raman Spectr.* **27**, 867 (1996).

[239] S. Grammatica and J. Mort, *J. Appl. Phys.* **85**, 445 (1981).

[240] R. O. Loutfy, C. K. Hsiao, A. M. Hor, and G. Di-Paola-Baranyi, *J. Imaging Sci.* **29**, 148 (1985).

[241] A. AUGER, P. M. BURNHAM, I. CHAMBRIER, M. J. COOK, and D. L. HUGHES, *J. Mater. Chem.* **15**, 168 (2005).

[242] R. O. LOUTFY, A. M. HOR, G. DI-PAOLA-BARANYI, and C. K. HSIAO, *J. Imaging Sci.* **29**, 116 (1986).

[243] S. KERA, Y. YABUUCHI, H. YAMANE, H. SETOYAMA, K. K. OKUDAIRA, A. KAHN, and N. UENO, *Phys. Rev. B* **70**, 085304 (2004).

[244] S. C. B. MANNSFELD and T. FRITZ, *Phys. Rev. B* **69**, 075416 (2004).

[245] S. C. B. MANNSFELD and T. FRITZ, *Phys. Rev. B* **71**, 235405 (2005).

[246] Y. MAJIMA, K. YAMAGATA, and M. IWAMOTO, *J. Appl. Phys.* **86**, 3229 (1999).

[247] X.-H. KONG, M. WANG, S.-B. LEI, Y.-L. YANG, and C. WANG, *J. Mater. Chem.* **16**, 4265 (2006).

[248] M. BRINKMANN, J. C. WITTMANN, M. BARTHEL, M. HANACK, and C. CHAUMONT, *Chem. Mater.* **14**, 904 (2002).

[249] H. TADA, H. TOUDA, M. TAKADA, and K. MATSUSHIGE, *Appl. Phys. Lett.* **76**, 873 (2000).

[250] T. NISHI, K. KANAI, Y. OUCHI, M. R. WILLIS, and K. SEKI, *IPAP Conf. Ser.* **6**, 35 (2005).

[251] T. NISHI, K. KANAI, Y. OUCHI, M. R. WILLIS, and K. SEKI, *Chem. Phys.* **325**, 121 (2006).

[252] M. HONDA, K. KANAI, K. KOMATSU, Y. OUCHI, H. ISHII, and K. SEKI, *J. Appl. Phys.* **102**, 103704 (2007).

[253] F. DIETZ, N. TYUTYULKOV, G. MADJAROVA, and K. MÜLLEN, *J. Phys. Chem. B* **104**, 1746 (2000).

[254] H. PROEHL, M. TOERKER, F. SELLAM, T. FRITZ, and K. LEO, *Phys. Rev. B* **63**, 205409 (2001).

[255] R. Forker, T. Dienel, T. Fritz, and K. Müllen, *Phys. Rev. B* **74**, 165410 (2006).

[256] F. Sellam, T. Schmitz-Hübsch, M. Toerker, S. Mannsfeld, H. Proehl, T. Fritz, K. Leo, C. Simpson, and K. Müllen, *Surf. Sci.* **478**, 113 (2001).

[257] U. Zimmermann and N. Karl, *Surf. Sci.* **268**, 296 (1992).

[258] P. Samori, X. Yin, N. Tchebotareva, Z. Wang, T. Pakula, F. Jäckel, M. D. Watson, A. Venturini, K. M. üllen, and J. P. Rabe, *J. Am. Chem. Soc.* **126**, 3567 (2004).

[259] P. Samori, A. Fechtenkötter, E. Reuther, M. D. Watson, N. Severin, K. M. üllen, and J. P. Rabe, *Adv. Mater.* **18**, 1317 (2006).

[260] S. Ito, P. T. Herwig, T. Böhme, J. P. Rabe, W. Rettig, and K. Müllen, *J. Am. Chem. Soc.* **122**, 7698 (2000).

[261] N. Tchebotareva, X. Yin, M. D. Watson, P. Samori, J. P. Rabe, and K. M. üllen and, *J. Am. Chem. Soc.* **125**, 9734 (2003).

[262] F. Jäckel, X. Yin, P. Samori, N. Tchebotareva, M. D. Watson, A. Venturini, K. Müllen, and J. P. Rabe, *Synt. Metal.* **147**, 5 (2004).

[263] S. C. B. Mannsfeld, K. Leo, and T. Fritz, *Phys. Rev. Lett.* **94**, 056104 (2005).

[264] T. S.-H. F. Sellam, R. Staub, M. Toerker, T. Fritz, C. Kübel, and K. M. K. Leo, *Surf. Sci.* **445**, 358 (2000).

[265] M. Toerker, T. Fritz, and H. Proehl, *Phys. Rev. B* **65**, 245422 (2002).

[266] S. A. Jenckhe and J. A. Osaheni, *Science* **265**, 765 (1994).

[267] G. Yu, J. Gao, J. C. Hummelen, and A. J. Heeger, *Science* **270**, 1789 (1995).

[268] A. Dodabalapur, Z. Bao, A. Makhija, G. Laquindanum, V. R. Raju, Y. Feng, E. Katz, and J. Rogers, *Appl. Phys. Lett.* **73**, 142 (1998).

[269] C. W. Tang, *Appl. Phys. Lett.* **48**, 183 (1986).

[270] T. Tsuzuki, Y. Kuwabara, W. Noma, Y. Shirota, and M. R. Willis, *Jpn. J. Appl. Phys.* **35**, 4 (1996).

[271] M. Prietsch, *Phys. Rep.* **253**, 163 (1995).

[272] V. Narayanamurti and M. Kozhevnikov, *Phys. Rep.* **349**, 447 (2001).

[273] A. Savitzky and M. J. E. Golay, *Analy. Chem.* **36**, 1627 (1964).

[274] J. S. Blakemore, *J. Appl. Phys.* **53**, 123 (1982).

[275] C. W. Tang, S. A. VanSlyke, and C. H. Chen, *J. Appl. Phys. Lett.* **65**, 3610 (1989).

[276] J. Kido, M. Kimura, and K. Nagaim, *Science* **67**, 1332 (1995).

[277] M. Hiramato, H. Fujiwara, and M. Yokoyama, *Appl. Phys. Lett.* **51**, 913 (1987).

[278] M. Hiramato, H. Fujiwara, and M. Yokoyama, *J. Appl. Phys. Lett.* **72**, 3781 (1992).

[279] C.-Y. Liu, L. V, and A. J. Bard, *Chem. Mater.* **9**, 943 (1997).

[280] C.-Y. Liu and A. J. Bard, *Chem. Mater.* **10**, 840 (1998).

[281] H. Ishii, K. Sugiyama, E. Ito, and K. Seki, *Adv. Mat.* **11**, 605 (1999).

[282] K. Konstadinidis, F. Papadimitrakopoulos, M. Galvin, and R. L. Opila, *J. Appl. Phys.* **77**, 5642 (1995).

[283] P. Dannetum, M. Boman, S. Stafström, W. R. S. R. Lazzaroni, C. Fredriksson, J. L. Brédas, R. Zamboni, and C. Taliani, *J. Chem. Phys.* **99**, 664 (1993).

[284] I. G. Hill, A. Rajagopal, A. Kahn, and Y. Hu, *Appl. Phys. Lett.* **73**, 662 (1998).

[285] J. Ivanco, F. P. Netzer, and M. G.Ramsey, *J. Appl. Phys.* **101**, 103712 (2007).

[286] N. K. Swami, S. Srivastava, and H. M. Ghule, *J. Phys. D : Appl. Phys.* **12**, 765 (1979).